SLAC–PUB–6458
April 1994
(A)

DYNAMIC APERTURE AND TRANSVERSE PROTON DIFFUSION IN HERA*

F. ZIMMERMANN
Stanford Linear Accelerator Center
Stanford University, Stanford, CA 94309

ABSTRACT

The dynamic aperture caused by persistent-current nonlinear field errors is an important concern in the design of superconducting hadron storage rings. The HERA proton ring is the second superconducting accelerator in operation. In this lecture note, its measured dynamic aperture is compared with that inferred from comprehensive tracking studies. To understand the difference between prediction and measurement, a semi-analytical method is developed for evaluating transverse diffusion rates due to various processes, such as modulational diffusion or sweeping diffusion. This analysis makes use of parameters for high-order resonances in the transverse phase space, which are obtained by normal-form algorithms using differential-algebra software. The semi-analytical results are consistent with the measurements, and suggest that the actual dynamic aperture is caused by an interplay of tune modulation and nonlinear magnetic fields.

Presented at the Accelerator Physics Lectures at the Superconducting Super Collider, Dallas, TX, October 29, 1992

*Work supported by Department of Energy contract DE-AC03-76SF00515.

1. Introduction

1.1. Motivation

The HERA proton ring at DESY in Hamburg is the second large superconducting storage ring in operation. It was expected, and it has been partly verified in the first years of its operation, that the beam lifetime and performance of this storage ring will be limited by single particle nonlinear beam dynamics.

The persistent-current nonlinear field errors, the time-dependence of which proved to be harmful in the first superconducting accelerator, the Fermilab Tevatron, are potentially more dangerous for HERA due to the larger ratio of the maximum dipole field to the field at injection B_{max}/B_{inj} which is about 20, compared to 6 for the Tevatron. At the injection energy of 40 GeV the relative size of the nonlinear field errors is significantly increased. In addition the size of the injected beam is also larger. Therefore the impact of the persistent-current induced field errors on the dynamic aperture is a question of considerable concern.

Consequently, strong effort has been devoted to detailed magnet measurements,[1] a dedicated local correction scheme,[2] comprehensive simulation studies,[3, 4] a reference magnet system allowing permanent control of the time dependence of the dipole and sextupole field errors, and to the invention of special magnet 'massage' cycles to achieve reproducibility. Following this recipe it has proved possible to inject a proton beam into HERA with a reasonable lifetime of about ten hours.[5] Nevertheless there is evidence for a dynamic aperture limitation inside the physical aperture.

1.2. Outline

The structure of this note is as follows. In Section 2 techniques of tracking data analysis are described with special emphasis on the Lyapunov-exponent method. In the remainder of Section 2 the dynamic aperture deduced from the simulation studies is compared with the one actually measured in HERA. It is shown that inclusion of a realistic tune modulation in the simulation leads to better agreement with the observations. Section 3 is devoted to an overview of various effects that tune modulation can have on a single resonance island. Some sources of tune modulation in a storage ring are discussed, and estimates of the corresponding modulation frequencies and amplitudes are presented in Section 4. Parameters of several high-order resonances in HERA are calculated in Section 5 by means of differential-algebra techniques and Lie-algebraic methods. Section 6 describes a semi-analytical approach based on these parameters to determine the transverse diffusion rates caused by modulational diffusion and sweeping diffusion. The results are summarized and some conclusions are drawn in Section 7. More details and additional information may be found in Refs. 6, 7.

2. Analysis of Tracking Data and Expected Dynamic Aperture

The dynamic aperture is defined as the border in phase space inside which particle motion is stable for a sufficiently large number of turns around the storage ring. For superconducting

hadron colliders the aperture can be strongly limited at injection energy due to the field errors caused by persistent currents in the magnets. In HERA the minimum time needed to inject 210 bunches is about 20 minutes, corresponding to $6 \cdot 10^7$ turns. Tracking studies with the present computer systems fall short of this number of revolutions by almost a factor 100. There are two possible approaches to overcome this problem:

- The tracking data for a smaller number of turns are analysed in such a way as to detect potentially unstable trajectories, which may result in a particle loss after a much longer time period. A promising approach of this category is based on a calculation of Lyapunov exponents and the determination of the border between regular and chaotic motion, which can be viewed as a good estimate for the actual dynamic acceptance. Here $10^3 - 10^4$ turns are usually sufficient to yield fairly accurate results.

- The employed model of the accelerator is simplified. For instance the complete storage ring can be replaced by a Taylor map representation.[8] Such a Taylor map can easily be extracted from a standard tracking code with the methods of differential algebra.[9] In order to avoid artificial emittance growth in the simulation,[10] the Taylor map must be modified by some symplectification scheme, for instance by performing a kick factorization.[11] Following this approach a gain in computational speed by a factor 10–20 is possible.[12] It is evident that the Taylor map tracking can also be analysed with respect to chaotic motion, thereby further reducing the required computing time.

We now discuss the Lyapunov-exponent method in more detail.

2.1. Lyapunov Exponent

The Lyapunov exponent characterizes the rate of divergence of initially close trajectories and provides a sensitive measure of local instabilities in phase space. For regular motion the distance d in phase space between two tracks grows linearly with the number of turns N. When averaged over long periods of time,

$$d(N) \propto N.$$

Chaotic motion is characterized by an exponential growth of this distance:

$$d(N) \propto \mathrm{e}^{\lambda N},$$

where λ is called the Lyapunov exponent (see for instance Ref. 13). Its formal definition is

$$\lambda \equiv \lim_{N\to\infty} \lim_{d(0)\to 0} \frac{1}{N} \ln \frac{d(N)}{d(0)}, \tag{1}$$

and it is independent of the measure of d, i.e., the value of λ does not depend on the choice of metric for the phase space.[14] It should be noted that the Lyapunov exponent λ is zero for a regular trajectory.

A general particle trajectory is described by the six canonical coordinates x, p_x, z, p_z, σ, and η.[15] Here x and z are the horizontal and vertical displacements from the design orbit, σ

is the longitudinal distance from the bunch center, and η the relative energy deviation. The canonically conjugate momenta to x and z are denoted by p_x and p_z, respectively. In linear approximation the six-dimensional phase space coordinates after N turns are related to the initial values through the N-turn Jacobian matrix J_N:

$$J_N \equiv \frac{\partial(x, z, \sigma, p_x, p_z, \eta)_N}{\partial(x, z, \sigma, p_x, p_z, \eta)_0}. \tag{2}$$

The limit of vanishing initial distance $d(0) \to 0$ in Eq. (1) can be performed exactly,[14] leading to an alternative expression in which the Lyapunov exponent is given in terms of the largest eigenvalue $EV_{N,\max}$ of the Jacobian matrix J_N:

$$\lambda \equiv \lim_{N\to\infty} \lambda_N \equiv \lim_{N\to\infty} \frac{1}{N} \ln |EV_{N,\max}|. \tag{3}$$

The modulus of the largest eigenvalue $EV_{N,\max}$ shows the same behavior as a function of N as the distance $d(N)$. That means, for a regular trajectory a linear increase with the number of turns is observed, and for chaotic motion the eigenvalue increases exponentially.

At this point it is appropriate to review some basic concepts of accelerator physics.[16, 17] The equations of motion can be solved exactly for a model of the storage ring consisting only of dipoles, quadrupoles, and drift spaces, hereafter referred to as a 'linear storage ring'. Without coupling between the three planes of motion, a particle performs a betatron oscillation of the form

$$y = \sqrt{\epsilon_y \beta_y(s)} \cos(\phi_y(s) + \phi_{y\,0}), \tag{4}$$

where y denotes either the horizontal or the vertical displacement with respect to the reference orbit, and the coordinate s is the path length along that orbit. The linear storage ring is completely characterized by the *beta function* $\beta_y(s)$, which is a periodic function

$$\beta_y(s) = \beta_y(s + C),$$

C being the circumference of the ring. This function not only describes the s-periodic part of the oscillation amplitude in Eq. (4), but it also determines the derivative of the phase function $\phi_y(s)$:

$$\frac{d\phi_y(s)}{ds} = \frac{1}{\beta_y(s)}. \tag{5}$$

Hence the number of betatron oscillations per turn, called Q-value or *tune*, is given by

$$Q_y = \frac{1}{2\pi} \oint \frac{1}{\beta_y(s)}\, ds. \tag{6}$$

One of the two constants of integration, ϵ_y and $\phi_{y\,0}$, in Eq. (4), namely the initial phase $\phi_{y\,0}$, is of no particular importance. The second, ϵ_y, describes the s-independent part of the oscillation amplitude. At a fixed value of s the particle trajectory is restricted to an ellipse in the y-p_y-plane, whose area F is related to ϵ_y by

$$F = \pi \epsilon_y. \tag{7}$$

The quantity ϵ_y is called *single-particle emittance* and is quoted in units of mm mrad. It equals twice the action variable I_y:

$$\epsilon_y = 2I_y \equiv 2 \cdot \frac{1}{2\pi} \oint p_y dy \tag{8}$$

In a linear storage ring the single-particle emittance ϵ_y defined by Eq. (4) or (7) is a constant of motion. The real storage ring is not linear, and the actual particle trajectories deviate from the solution to Eq. (4). Nevertheless, because this deviation is small over short periods of time, it is still fruitful to use the linear solution as a parametrization in the tracking analysis. In the presence of nonlinearities, ϵ_y calculated according to Eq. (4) does not stay constant, but can increase (or decrease) slowly as a function of time. Because the divergence from the linear solution depends strongly on the starting value of ϵ_y itself, the particles inside a bunch will suffer different changes of ϵ_y. In general, the increase of the average value of ϵ_y over the beam distribution differs strongly from the increase experienced by a particle, say, at one or at two standard deviations.

The emittance ϵ_y of a single trajectory, used throughout this thesis, is defined by Eq. (4) and should be understood simply as a measure of the squared horizontal or vertical oscillation amplitude normalized so as to be independent of the position around the ring. Very often we will quote the sum $\epsilon \equiv \epsilon_x + \epsilon_z$, called the total transverse emittance.

Occasionally we also refer to the two-sigma beam emittance, which is the emittance of a particle trajectory enclosing 86% of the beam in phase space. The two-sigma beam emittance will be denoted by the symbol $\bar{\epsilon}$ and is to be distinguished from the single-particle emittance ϵ defined before, which refers to an arbitrary trajectory.

In the case of a linear storage ring the difference of the phase ϕ_y between two nearby trajectories as a function of the number of turns is a constant, because the local phase advance is given by $1/\beta_y(s)$ for all particles. In a nonlinear system the phase advance depends on the amplitude, and the phase distance $|\phi_{y,1} - \phi_{y,2}|$ grows at least linearly in time.

The use of the Lyapunov method in the postprocessing analysis of tracking data rests on the following observations and hypotheses:

1. The divergence between two particles, as observed in cartesian coordinates, is mainly information on the phase distance and not on the amplitude evolution. It is therefore advantageous to consider only the phase separation $(\frac{1}{2}\sum_{y=x,z}(\phi_{y,1} - \phi_{y,2})^2)^{\frac{1}{2}}$, respective to its three-dimensional generalization, instead of the strongly oscillating cartesian distance between two trajectories.

2. The eigenvalue behavior and the phase divergence are almost identical (Figs. 1a and b, and 2a and b). This implies that two-particle-tracking already gives very accurate results and that a sufficiently small initial distance had been chosen, the limitation in this quantity being given by rounding errors.

3. Considerable improvement can be achieved by investigating the phase distance in a suitably 'normalized' coordinate frame, in which all phase space deformations up to a specific order have been removed. For regular motion the distance between two particles in the

Figure 1: Regular trajectory in a HERA-like FODO cell for 5,000 turns: a) maximum eigenvalue, b) phase distance between two nearby particles, c) phase distance between two nearby particles in normal-form coordinates.[55]

normalized coordinates evolves almost free of any disturbing oscillations (Figs. 1b and c), whereas for strongly chaotic trajectories the transformation to new coordinates has virtually no effect (Figs. 2b and c). The increased sensitivity for detecting barely chaotic particles by this method is documented in Fig. 3.

4. Particles with positive Lyapunov exponents experience an emittance growth on a longer time scale. Hence an exponential phase separation indicates a long-term amplitude increase and possible final particle loss. This is the main reason for the use of Lyapunov exponents in tracking studies and has been confirmed for all cases under consideration. An example is shown in Fig. 4.

Figure 2: Chaotic trajectory in a HERA-like FODO cell for 5,000 turns: a) maximum eigenvalue, b) phase distance between two nearby particles, c) phase distance between two nearby particles in normal-form coordinates.[55]

Figure 3: Barely chaotic trajectory in a HERA-like FODO cell: a) phase distance between two nearby particles for 30,000 turns, b) phase distance between two nearby particles for 5,000 turns, c) phase distance between two nearby particles in normal-form coordinates for 5,000 turns (the change of the slope indicates chaotic motion).[55]

Figure 4: Lyapunov exponent for a regular and a chaotic trajectory in HERA and the corresponding emittance evolution: a) and b) $\ln \lambda_N$ as a function of $\ln N$ for $10,000$ turns at starting amplitudes of 11.9 mm and 13.5 mm ($\beta = 76$ m), respectively, with $\Delta p/p = 10^{-3}$; c) and d) transverse emittance $\epsilon_x + \epsilon_z$ over $120,000$ revolutions for the same two trajectories. Each dot represents the maximum value during 200 turns.

2.2. Effect of the Persistent-Current Field Errors

Comprehensive tracking calculations have been performed to study the effect of magnetic field errors on the dynamic aperture of HERA at the injection energy of 40 GeV. The measured individual multipole components up to 20-pole of all superconducting dipoles and quadrupoles were taken into account by adding five thin, higher-order lenses to each FODO half cell. The details and methods used in the tracking-data analysis are described elsewhere[18, 19, 4] (see also Section 2.1). The simulations provide an estimate of the dynamic aperture, defined by the onset of chaotic particle motion.

The predicted dynamic aperture of the HERA proton ring is shown in Fig. 5 as a function of the amplitude of momentum oscillation $\Delta p/p$. The dynamic aperture r is given in units of mm and depends on the beta function β at the point of observation. In this case β is chosen to be 76 m, the maximum value in the arcs. A quantity that is closely related to the aperture, but is independent of the point of observation, is the dynamic acceptance $A_{x,z}$, which is defined as the single-particle emittance of the outermost stable trajectory and is quoted in units of mm mrad. The relation between aperture r and acceptance A is

$$A \equiv A_x + A_z = r^2/\beta \qquad \text{or} \qquad r \equiv \sqrt{A \cdot 76\text{m}} \quad , \tag{9}$$

where $\beta = 76$ m is the beta function value at the point, to which r refers.

The working point of $Q_x = 31.27$ and $Q_z = 32.30$ chosen for the investigation is close to the actual value used in the HERA operation of 1992. In 1992 the circumferential rf voltage of the 52 MHz system was about 70 kV, corresponding to a synchrotron frequency of 22 Hz. This value is also used in the simulation. For a proper bucket matching between PETRA and HERA a smaller rf voltage and synchrotron frequency are required. The design synchrotron frequency is 14 Hz.

The dynamic acceptance expected from the threshold of chaos in the simulation studies is $A \approx 4$ mm mrad for on-momentum particles, equivalent to an aperture of 17.5 mm. The onset of chaos is considerably reduced to about $A = 1.9$ mm mrad or $r = 12$ mm for an initial momentum deviation of $\Delta p/p = 5 \cdot 10^{-4}$, which is about the actual momentum spread of the injected bunch.

Two effects may cause a reduction of the dynamic aperture for off-momentum particles. Firstly, the nonlinear fields are larger on a dispersion orbit than for particles with $\Delta p/p = 0$. However, for a relative momentum deviation of $\Delta p/p = 5 \cdot 10^{-4}$ and an average dispersion function of about 1.5 m in the arc the orbit shift is less than 1 mm. This is much too small to explain the reduction of aperture noticed in Fig. 5. Secondly, large synchrotron oscillations induce a betatron tune modulation via the chromaticity of the storage ring. In the model-calculations the corrected chromaticity is $\xi_x = -1.3$, and $\xi_z = 0.6$. Hence the resulting tune modulation amplitude for a typical off-momentum trajectory is in the order of the momentum spread $5 \cdot 10^{-4}$. The observed reduction of the dynamic aperture for off-momentum particles can mainly be ascribed to the additional tune modulation.

In agreement with this interpretation is the observation that for a circumferential rf voltage of 2 MV (and a different working point $Q_x = 31.15$ and $Q_z = 32.18$) the dynamic aperture is reduced by less than 10% in the simulation, for a particle with $\Delta p/p = 5 \cdot 10^{-4}$.[18] An

Figure 5: Dynamic aperture in the arcs of the HERA proton ring expected from simulation studies for the working point ($Q_x = 31.27$, $Q_z = 32.30$) and a circumferential rf voltage of 70 kV. Shown are amplitude values r in mm, defined by the equation $r = \sqrt{\beta(\epsilon_x + \epsilon_z)}$ with $\beta = 76$ m, as a function of the amplitude of momentum oscillations $\Delta p/p$. Also indicated is a range of values for the real dynamic aperture measured in 1992. The uncertainty depicted does not refer to the error of the measurement, which is much smaller, but to the variation observed over periods of days or weeks.

rf voltage of 2 MV corresponds to a synchrotron frequency of about 120 Hz. As will be shown later a relatively small tune modulation frequency such as the synchrotron frequency of 22 Hz used in 1992 is potentially much more harmful. This can be explained by high-order resonances, which are studied in Section 5.

Also shown in Fig. 5 is the design beam size, corresponding to two standard deviations σ, and a rough measurement of the actual dynamic aperture in the HERA proton ring. Proton beams that are injected with large transverse oscillations have a lifetime of less than 1 hour, which suggests that the dynamic aperture is smaller than the physical aperture. This is confirmed by beam profile measurements with the residual gas monitors.[21] These indicate that the dynamic aperture is about 1.2 mm mrad, while the linear acceptance as measured by orthogonal orbit

Table 1: Influence of tune modulation on the dynamic acceptance in HERA at $\Delta p/p = 0$ and $\Delta p/p = 10^{-3}$. The results are obtained by simulations of the six-dimensional motion with uncompensated linear coupling. The modulation frequency f_q in Hz is related to the modulation tune Q_m by $f_q \equiv Q_m f_{rev}$, where f_{rev} denotes the revolution frequency ($f_{rev} = 47.3$ kHz for HERA).

q	f_q in Hz	acceptance in mm mrad	
		$\Delta p/p = 0$	$\Delta p/p = 10^{-3}$
0	0	4.2	1.9
0.001	10	1.5	—
0.005	10	1.5	—
0.01	10	1.2	0.9
0.005	50	1.9	—
0.01	50	1.9	0.9
0.005	600	3.1	—
0.01	600	3.1	—

bumps is between 2.3 and 3.0 mm mrad. The observed bunch lengths are always smaller than 3 m, which provides an estimate of the dynamic momentum acceptance.

2.3. Tracking Studies including Tune Modulation

According to the previous section, the measured dynamic aperture is a factor of 1.5–2 smaller than the value expected from simulations which take into account only the nonlinear field errors. A better agreement is obtained if a modest tune modulation is included in the model.

It is of no great importance in which way the tune modulation is added. The reduction in acceptance is the same whether one modulates the strength of all quadrupoles or simply adds an additional rotation with a modulated angle at the end of each turn, provided that the overall modulation amplitude is the same.

The impact of tune modulation on the dynamic acceptance can be illustrated by the results of two tracking studies. Table 1 shows the reduction in the dynamic acceptance caused by a tune modulation of different frequency and amplitude. The data refer to a simulation performed for uncompensated linear coupling ($\kappa \approx 0.017$, where κ denotes the minimum difference between the two betatron tunes in the case of coupling[22]) and with full synchro-betatron motion. It can be seen that the sensitivity to the modulation frequency is much stronger than the sensitivity to the modulation amplitude and that a ripple of frequency 10–50 Hz can drastically reduce the aperture over a wide range of modulation amplitudes.

The effect of a 50-Hz ripple with an amplitude of 10^{-4} was simulated for pure betatron motion with different emittance ratios in the linearly decoupled accelerator ($\kappa \approx 0.003$). The results of this study are summarized in the two acceptance-diagrams of Fig. 6, which represent regular, chaotic, and unstable trajectories for the non-modulated case and in the presence of tune modulation, respectively. It can be seen that the tune modulation reduces the aperture by about a factor of 2.

Figure 6: Vertical versus horizontal dynamic acceptance in the case of pure betatron motion with compensated linear coupling: a) no tune modulation, b) 50 Hz tune ripple with amplitude 10^{-4}. Trajectories in the hatched region of diagram b) are chaotic only in the presence of tune modulation.

In Section 4 the actual modulation amplitudes are estimated to be as large as 10^{-4}. The strong effect of tune modulation on the dynamic aperture observed in the tracking studies, therefore, calls for an analytical study of the chaos-generating process, to which the subsequent sections will be devoted.

3. Tune Modulation

3.1. Single Resonance

Under normal operating conditions, the transverse phase space for a large proton storage ring is covered by a web of resonance islands. Close to one of these resonances, say $nQ \approx p$ for one degree of freedom, the transverse motion is approximately described by the nonlinear Hamiltonian

$$H(I, \phi, \theta) = IQ_0 + g(I) + h(I)\cos(n\phi - p\theta), \tag{10}$$

where $g(I)$ and $h(I)$ denote in general nonlinear functions of the action I, which are called detuning and driving term, respectively. Of importance for HERA is the case of several isolated weak resonances, for which $g(I) \gg h(I)$. From Eq. (10), the amplitude-dependent tune is [†]

$$Q(I) = Q_0 + \frac{dg}{dI}(I) \approx \phi'.$$

The resonance condition is fulfilled at a certain action value I_r defined by $nQ(I_r) = p$. If Eq. (10) is expanded around the resonant value I_r, a further approximation is possible:

$$K(\Delta, \tilde{\phi}) = \frac{1}{2}\left(\frac{d^2g}{dI^2}(I_r)\right)\Delta^2 + h(I_r)\cos n\tilde{\phi}, \tag{11}$$

where the new momentum and phase variables are defined by

$$\Delta \equiv I - I_r, \tilde{\phi} \equiv \phi - \frac{p}{n}\theta.$$

Equation (11) is recognized as the Hamiltonian of a nonlinear pendulum. The total width of the pendulum separatrix is given by

$$\Delta I_{\mathrm{tot}} = 2\Delta_{\max} = 4\sqrt{\left|\frac{h(I_r)}{\frac{d^2g}{dI^2}(I_r)}\right|}. \tag{12}$$

For small oscillations around $\tilde{\phi}_r = \pi/n$, Eq. (11) can be expanded up to quadratic terms, $\cos n\tilde{\phi} \approx -1 + \frac{1}{2}n^2(\tilde{\phi} - \tilde{\phi}_r)^2$. This yields the frequency at which particles inside a resonance island oscillate around the elliptic fixed point,

$$Q_I = n\sqrt{\left|h(I_r)\frac{d^2g}{dI^2}(I_r)\right|}. \tag{13}$$

The frequency Q_I is called the 'island tune'.[23]

[†] A prime denotes the derivative with respect to theta.

3.2. Single Resonance with Modulation

In the presence of tune modulation the Hamiltonian assumes the form

$$H(I,\phi,\theta) = IQ_0 + g(I) + h(I)\cos\left(n\phi + \frac{nq}{Q_m}\sin(Q_m\theta+\alpha) - p\theta\right), \tag{14}$$

where q is the modulation amplitude, Q_m the modulation frequency, and α an arbitrary phase. Equation (14) differs from the Hamiltonian Eq. (10) only by the additional term $\frac{nq}{Q_m}\sin(Q_m\theta+\alpha)$ in the argument of the cosine. The contribution of the tune modulation to the total Hamiltonian becomes more explicit by means of a canonical transformation from (I,ϕ) to $(\bar{I},\bar{\phi})$ with the generating function

$$F_2(\bar{I},\phi) = \bar{I}\phi + \frac{q}{Q_m}\sin(Q_m\theta+\alpha)\bar{I}.$$

The transformation is

$$\bar{\phi} = \frac{\partial F_2}{\partial \bar{I}} = \phi + \frac{q}{Q_m}\sin(Q_m\theta+\alpha)$$

$$I = \frac{\partial F_2}{\partial \phi} = \bar{I}$$

and the new Hamiltonian is then (compare also to Ref. 23)

$$\bar{H} = H + \frac{\partial F_2}{\partial \theta} = Q_0\bar{I} + g(\bar{I}) + h(\bar{I})\cos(n\bar{\phi} - p\theta) + q\cos(Q_m\theta+\alpha)\bar{I}. \tag{15}$$

The last term describes the tune modulation. For this Hamiltonian we have

$$\bar{\phi}' = \frac{\partial\bar{\phi}}{\partial\theta} = \frac{\partial\bar{H}}{\partial\bar{I}} \approx Q_0 + \frac{\partial g}{\partial\bar{I}}(\bar{I}) + q\cos(Q_m\theta+\alpha). \tag{16}$$

Transforming again to the nonlinear pendulum variables

$$\bar{\Delta} = \bar{I} - \bar{I}_r, \bar{\bar{\phi}} = \bar{\phi} - \frac{p}{n}\theta$$

one obtains

$$\bar{K}(\bar{\Delta},\bar{\bar{\phi}},\theta) = \frac{1}{2}\frac{d^2g}{d\bar{I}^2}(\bar{I}_r)\bar{\Delta}^2 + h(\bar{I}_r)\cos n\bar{\bar{\phi}} + q\cos(Q_m\theta+\alpha)\bar{\Delta}, \tag{17}$$

which is the same as Eq. (11) plus an additional term that is linear in $\bar{\Delta}$.

3.3. Island Width of Sidebands

Equation (14) can be expanded into Bessel functions using the Jacobi-Anger identity:[23, 24, 6]

$$\cos\left(n\phi + \frac{nq}{Q_m}\sin(Q_m\theta+\alpha) - p\theta\right) = \sum_{j=-\infty}^{\infty} J_j\left(\frac{nq}{Q_m}\right)\cos(n\phi + jQ_m\theta - p\theta + j\alpha).$$

Inserting this expansion into Eq. (14) we get the generalized resonance condition in the presence of tune modulation,

$$nQ(I_r^j) + jQ_m - p = 0. \tag{18}$$

For each fundamental resonance $nQ-p=0$ a set of sideband resonances with $j \neq 0$ is generated. From

$$Q(I_r^j) = Q_0 + \frac{dg}{dI}(I_r^j) = \frac{p}{n} - \frac{j}{n}Q_m$$

and

$$\frac{dg}{dI}(I_r^j) \approx \frac{dg}{dI}(I_r) + \frac{d^2g}{dI^2}(I_r) \cdot j\delta I,$$

the distance δI between two sideband resonances is

$$\delta I \approx \frac{Q_m}{n\frac{d^2g}{dI^2}(I_r)}. \tag{19}$$

The width of the sideband separatrices is obtained by replacing $h(I_r)$ by $h(I_r)J_j(\frac{nq}{Q_m})$ in Eq. (12), the formula for the non-modulated case:

$$\Delta I_{\text{tot}}^j = 4\sqrt{\left|\frac{h(I_r)J_j(\frac{nq}{Q_m})}{\frac{d^2g}{dI^2}(I_r)}\right|}. \tag{20}$$

As a rule of thumb the Bessel function in Eq. (20) can have a significant value only if its argument is larger than the order, i.e., if

$$\frac{nq}{Q_m} > j. \tag{21}$$

Then the Bessel functions may be approximated by their rms values for large arguments:[25]

$$J_j(x) \approx \frac{1}{\sqrt{\pi x}}. \tag{22}$$

From Eq. (20) we then get (with Q_I as defined in Eq. (13))

$$\Delta I_{\text{tot}}^j \approx 4\frac{Q_I}{n}\left(\frac{Q_m}{qn\pi}\right)^{\frac{1}{4}}\frac{1}{\frac{d^2g}{dI^2}(I_r)}. \tag{23}$$

Following Ref. 26 we expect global chaos if the distance between two sidebands δI (Eq. (19)) is smaller than the width of the resonances ΔI_{tot}^j, i. e., if

$$\frac{Q_m}{n\frac{d^2g}{dI^2}(I_r)} < 4\frac{Q_I}{n}\left(\frac{Q_m}{qn\pi}\right)^{\frac{1}{4}}\frac{1}{\frac{d^2g}{dI^2}(I_r)}.$$

Therefore the condition for chaos becomes[23]

$$\frac{Q_m^{\frac{3}{4}}(nq)^{\frac{1}{4}}}{Q_I} \leq \frac{4}{\pi^{\frac{1}{4}}}. \tag{24}$$

Note that Eq. (21) has been assumed in deriving Eq. (24). Figures 7a and b illustrate the validity of Eqs. (21) and (22). For the two modulation frequencies $Q_m = 0.04$ and $Q_m = 0.1$ the location of the sideband resonances is depicted as a function of the modulation amplitude q. The chosen resonance parameters $n = 4$, $\frac{d^2g}{dI^2}(I_r) = 1$, and $Q_I = 4\sqrt{h(I_r)} = 0.049$ refer to the phase diagram shown in Fig. 9.

In Fig. 7, the island sizes $\Delta I^j_{\rm tot}$ are computed by the exact expression Eq. (20). Action values in the hatched area lie inside of some resonance island, whereas action values in the white regions are outside of any island. Hence, if there is no white space between two sidebands, these overlap. The centers of the sidebands are separated by $\delta I = Q_m/4$. They are closer, and resonance overlap is, therefore, more probable for the smaller modulation frequency Q_m (see Fig. 7a). The curves in Figs. 7a and b represent Eq. (21), which appears to be a good approximation of the number of sizable sidebands. As expected, this number grows about linearly with the modulation amplitude q.

The overlap criterion, Eq. (24), predicts a threshold of resonance overlap at modulation amplitudes $q \approx 1.8$ or $q \approx 0.12$ for the modulation frequencies of Figs. 7a and b, respectively. For larger modulation amplitudes no sideband overlap is expected, since the island size shrinks as a function of q, which is described by Eqs. (20) and (22). Figure 7a shows that the sideband resonances overlap at least up to the modulation amplitude $q = 1$, in agreement with Eq. (24). In Fig. 7b, the resonances become separated beyond about $q \approx 0.1 - 0.15$. This value is consistent with the prediction of Eq. (24), indicated by a straight vertical line, and thus corroborates Eq. (22).

If the inequalities in Eqs. (21) and (24) are fulfilled, we are in the chaotic region. Here an estimate of the 'diffusion' speed can be obtained in the following manner.[27, 28] Starting from the unperturbed Hamiltonian,

$$H(I, \phi, \theta) = IQ_0 + g(I) + h(I)\cos(n\phi - p\theta),$$

and the corresponding equation of motion for the action,

$$\frac{dI}{d\theta} = -\frac{\partial H}{\partial \phi} = nh(I)\sin(n\phi - p\theta), \tag{25}$$

we derive the increase in action (or emittance $\epsilon \equiv 2I$) during a single crossing of the fundamental resonance. Integration of Eq. (25) yields

$$\int_{I_1}^{I_2} \frac{dI}{h(I)} = \int_{\theta_1}^{\theta_2} n\sin(n\phi - p\theta)d\theta. \tag{26}$$

The integral on the right hand side can be calculated as demonstrated in Ref. 29. The main contribution comes from the neighborhood of the 'stationary phase' ϕ_0,[‡] where

$$\frac{\partial}{\partial\theta}(n\phi - p\theta)\bigg|_{\phi=\phi_0,\,\theta=\theta_0} = 0.$$

[‡]The 'method of stationary phase' is described for example in Ref. 30.

Figure 7: Location of the sideband islands with respect to the fundamental resonance as a function of the modulation amplitude q. The island sizes $\Delta I^j_{\rm tot}$ are derived from Eq. (20) for the resonance parameters $n = 4$, $d^2g/dI^2(I_r) = 1$, and $Q_I = 4\sqrt{h(I_r)} = 0.049$. (The corresponding phase diagram is shown in Fig. 9.) Action values in the hatched area are inside of some resonance island. Two sideband resonances overlap if they are not separated by a white region. The two diagrams refer to different modulation frequencies: a) $Q_m = 0.04$, b) $Q_m = 0.1$. According to Eq. (24), resonance overlap is expected only for the modulation amplitudes $q < 1.8$ or $q < 0.12$ in cases a and b, respectively. In b, this limit is depicted by the straight vertical line. The solid curves represent Eq. (21), which approximates the number of sizable sidebands.

A second order Taylor expansion around the phase ϕ_0,

$$\phi \approx \phi_0 + \frac{1}{2}\frac{\partial \phi}{\partial \theta^2}\bigg|_{\theta_0} (\theta - \theta_0)^2 \equiv \phi_0 + \frac{1}{2}\phi_0''(\theta - \theta_0)^2,$$

leads to

$$\int_{\theta_1}^{\theta_2} \sin(n\phi - p\theta)d\theta \approx \sin n\psi_0 \int_{\theta_1}^{\theta_2} \cos\left\{\frac{n\phi_0''}{2}(\theta - \theta_0)^2\right\} d\theta + \cos n\psi_0 \int_{\theta_1}^{\theta_2} \sin\left\{\frac{n\phi_0''}{2}(\theta - \theta_0)^2\right\} d\theta\,, \tag{27}$$

where, for brevity, a new phase variable $\psi_0 \equiv \phi_0 - \theta_0 p/n$ has been introduced. The remaining integrals are Fresnel integrals and can be solved. Assuming that the intervals $|\theta_1 - \theta_0|$ and $|\theta_2 - \theta_0|$ are sufficiently large,[29] the maximum value (as a function of ψ_0) of the integral in Eq. (27) is given by

$$\sqrt{\frac{2\pi}{n|\phi_0''|}}, \tag{28}$$

and its average absolute value is

$$\sqrt{\frac{8}{\pi n|\phi_0''|}}. \tag{29}$$

The average value will be used in our further discussion. Returning to Eq. (26) we find

$$\Delta I_{\text{single}} \equiv |I_2 - I_1| \approx nh(I_r) \cdot \sqrt{\frac{8}{\pi n|\phi_0''|}}, \tag{30}$$

under the assumption that $h(I) \approx h(I_r) =$ constant. We now remember that the motion is assumed to be chaotic. Thus the phase correlation is lost between subsequent resonance crossings, and the action increase can be described by a random walk process. Then the mean square uncertainty in the action after N resonance crossings grows as

$$\overline{(\Delta I)^2} = N(\Delta I_{\text{single}})^2. \tag{31}$$

Taking into account the tune modulation, the modulus of the second derivative of the phase is replaced by its average value

$$|\phi_0''| \approx \frac{2}{\pi} q Q_m. \tag{32}$$

Since the number of resonance crossings after a time Δt is

$$N = 2Q_m f_{rev} \Delta t, \tag{33}$$

(two crossings per modulation period), we obtain

$$\frac{\overline{(\Delta\epsilon)^2}}{\Delta t} = 32\frac{f_{rev} n h^2(I_r)}{q}, \tag{34}$$

where $\epsilon \equiv 2I$ denotes the single-particle emittance. The diffusion coefficient $D \equiv \frac{1}{2}\overline{(\Delta\epsilon)^2}/(\Delta t)$ is inversely proportional to the modulation amplitude q and independent of the modulation frequency Q_m.

3.4. Diffusion Rate for a Two-Dimensional Map

To examine the validity of Eq. (34) a numerical simulation is performed for a two-dimensional map consisting of a rotation

$$\begin{pmatrix} x \\ p \end{pmatrix}_f = \begin{pmatrix} \cos 2\pi Q & \sin 2\pi Q \\ -\sin 2\pi Q & \cos 2\pi Q \end{pmatrix} \begin{pmatrix} x \\ p \end{pmatrix}_i, \tag{35}$$

where Q depends on the amplitude in the form

$$Q = Q_0 + \frac{\alpha}{4}(x_i^2 + p_i^2)^2, \tag{36}$$

and an octupolar kick

$$p_f = p_i - x_i^3. \tag{37}$$

The corresponding Hamiltonian is

$$H = \left(Q_0 - \frac{1}{4}\right) I + \frac{\alpha}{3} I^3 + \frac{1}{16\pi} I^2 \cos 4\phi + \frac{3}{16\pi} I^2 + \frac{4}{16\pi} I^2 \cos 2\phi, \tag{38}$$

with the usual definitions of I and ϕ:

$$x = \sqrt{2I}\cos\phi \qquad \text{and} \qquad p = -\sqrt{2I}\sin\phi. \tag{39}$$

If the tune is close to the resonance $4Q \approx 1$ and if, furthermore, $\alpha \gg 1$, the last two terms in the Hamiltonian may be disregarded, and the driving term of the fourth integer resonance

$$h(I) = \frac{1}{16\pi} I^2 \tag{40}$$

is much smaller than the detuning function

$$g(I) = \frac{\alpha}{3} I^3. \tag{41}$$

The case $h(I) \ll g(I)$ is typical for a storage ring, where one stays away from strong low-order resonances. Note that the absolute value of the detuning and driving terms can be changed by a scale transformation. Let us choose $Q_0 = 0.23$ and $\alpha = 1000$. The condition $\partial H/\partial I = 0$ then leads to the resonant action value

$$I_r \approx \sqrt{\frac{1}{\alpha}\left(\frac{1}{4} - Q_0\right)} \approx 4.5 \cdot 10^{-3}, \tag{42}$$

and the elliptic fixed points are located at

$$x_r = p_r = \sqrt{I_r} \approx 6.7 \cdot 10^{-2}. \tag{43}$$

Figure 8: Emittance spread for 200 chaotic trajectories of the two-dimensional maps, Eqs. (35)–(37), as functions of the number of turns.

The island tune from Eq. (13) is

$$Q_I = 4\sqrt{\frac{2\alpha I_r^3}{16\pi}} \approx 7.6 \cdot 10^{-3}. \tag{44}$$

An additional tune modulation with amplitude $q \approx 0.1$ and frequency $Q_m \approx 6.25 \cdot 10^{-3}$, not too far from the island tune, destroys the resonance island chain and gives rise to global chaos in agreement with Eq. (24). An ensemble of 200 particles is placed inside the chaotic region with a tiny initial spread in position of 10^{-7}. The evolution of the rms-emittance-spread of this ensemble is shown in Fig. 8 as a function of the turn number for two different modulation amplitudes. After a transient period of about 2,000 turns, in which the initially very close particles lose their phase correlation, the evolution is well described by Eq. (34). In particular, it is verified that the diffusion rate is inversely proportional to the modulation amplitude q.

3.5. Adiabatic Trapping

If the modulation frequency Q_m is held constant, Eq. (24) determines a maximum value of the modulation amplitude q, below which the motion is chaotic. Here and in the next section, a complementary mimimum value of the modulation amplitude q is derived and justified.

For a constant tune the position of the resonance islands is uniquely determined. If a tune modulation is added, however, the resonance islands change their locations in phase space with the periodicity of the modulation cycle. Provided that the frequency of the tune modulation is sufficiently small, particles initially close to the centers of the islands move with the islands, returning to the vicinity of their initial positions once every modulation period. In this case the tune modulation is called adiabatic.[31]

The adiabatic boundary can be derived from the intuitive condition[27, 28]

$$\left\{ \begin{array}{c} \text{action change rate} \\ \text{of island center due to} \\ \text{the slow tune variation} \end{array} \right\} < \left\{ \begin{array}{c} \text{action change rate} \\ \text{caused by the motion} \\ \text{around the resonance} \end{array} \right\}. \tag{45}$$

The maximum change rate of the action value for the island center is obtained from the action-dependence of the tune in the following way:

$$\phi_r' \approx Q_0 + \frac{dg}{dI}(I_r), \tag{46}$$

$$\phi_r'' \approx \frac{d^2g}{dI^2}(I_r)\frac{dI_r}{d\theta}, \quad \text{and} \tag{47}$$

$$\left.\frac{dI_r}{d\theta}\right|_{\max} = \frac{|\phi_r''|_{\max}}{\left|\frac{d^2g}{dI^2}(I_r)\right|} = \frac{qQ_m}{\left|\frac{d^2g}{dI^2}(I_r)\right|}. \tag{48}$$

According to Eq. (15) the action change during the motion around the resonance center is

$$\frac{dI}{d\theta} = h(I_r)n\sin(n\bar{\phi} - p\theta) \approx h(I_r)\cdot n \tag{49}$$

(here it has been assumed that $\sin(n\bar{\phi} - p\theta) \approx 1$ for a trajectory half-way between stable and unstable fixed points). By means of Eqs. (45), (48), and (49) the adiabaticity condition is

$$qQ_m < \frac{d^2g}{dI^2}(I_r)\cdot h(I_r)\cdot n,$$

or, using the island tune of Eq. (13),

$$\left|\frac{qQ_m}{Q_I^2}\right| < \frac{1}{n}. \tag{50}$$

It should be mentioned that Eq. (50) agrees with the condition that the fixed point of the 0th sideband becomes unstable in the limit of small modulation frequency.[23]

3.6. Small Angle Approximation

For small oscillations around the stable fixed points the $\cos n\phi$-term in Eq. (17) can be expanded, and the Hamiltonian is approximated [§] as follows:[23]

$$K(\Delta,\phi) = \frac{1}{2}\frac{d^2g}{dI^2}(I_r)\Delta^2 + h(I_r)\frac{1}{2}(n\phi)^2 + q\cos(Q_m\theta + \alpha)\bar{\Delta}. \tag{51}$$

[§]For convenience, the definition of the phase ϕ is changed by π/n, and the superscripts of Eq. (17) are dropped.

In this approximation the nonlinear pendulum of Eq. (11) has been replaced by a harmonic oscillator. From Eq. (51) we have the equations of motion

$$\dot{\Delta} = -hn^2\phi \qquad \text{and} \qquad \dot{\phi} = \frac{d^2g}{dI^2}\Delta + q\cos(Q_m\theta + \alpha).$$

$$\text{So} \qquad \ddot{\Delta} + Q_I^2\Delta = -\frac{qQ_I^2}{\frac{d^2g}{dI^2}}\cos(Q_m\theta + \alpha). \tag{52}$$

This is the equation of a driven harmonic oscillator. An analogous equation is satisfied by ϕ:

$$\ddot{\phi} + Q_I^2\phi = -qQ_m\sin(Q_m\theta + \alpha). \tag{53}$$

A special solution is

$$\phi = -\frac{Q_m^2}{Q_I^2 - Q_m^2}\frac{q}{Q_m}\sin(Q_m\theta + \alpha), \tag{54}$$

and

$$\Delta = -\frac{Q_I^2}{Q_I^2 - Q_m^2}\frac{q}{\frac{d^2g}{dI^2}}\cos(Q_m\theta + \alpha). \tag{55}$$

The prerequisite for this approximation has been given in Ref. 23 as

$$\left|\frac{qQ_m}{Q_I^2 - Q_m^2}\right| < \frac{1}{n}. \tag{56}$$

This can be obtained from Eq. (54), if one requires

$$n\phi \ll 1,$$

on which the quadratic expansion of the cosine in Eq. (17) was based.

Equation (56) has different physical interpretations in the high and low frequency limits. For small modulation frequencies Q_m, Eq. (56) becomes identical to Eq. (50), which represents the adiabatic boundary. In the limit of large modulation frequencies, Eq. (56) approaches Eq. (21) for $j = 1$, which specifies the border where the first sideband resonance starts to be important.

3.7. Two Degrees of Freedom

The theory of tune modulation outlined above suits also the more general situation of resonances for two degrees of freedom, if the appropriate replacements are made in the previous formulae. The Hamiltonian

$$H(I_x, I_z, \phi_x, \phi_z, \theta) = I_xQ_{x0} + I_zQ_{z0} + g(I_x, I_z) + h(I_x, I_z)\cos(k\phi_x + l\phi_z - p\theta) \tag{57}$$

describes the effect of a single resonance $kQ_x + lQ_z - p \approx 0$. By means of the generating function

$$F(\bar{I}_x, \bar{I}_z, \phi_x, \phi_z, \theta) = (k\phi_x + l\phi_z - p\theta)\bar{I}_x + \phi_z\bar{I}_z \tag{58}$$

new canonical variables $\bar{\phi}_x$, $\bar{\phi}_z$, $\bar{I}_x$, and $\bar{I}_z$ are introduced according to

$$\bar{\phi_x} = \frac{\partial F}{\partial \bar{I}_x} = k\phi_x + l\phi_z - p\theta \quad , \quad \bar{\phi_z} = \frac{\partial F}{\partial \bar{I}_z} = \phi_z \tag{59}$$

$$I_x = \frac{\partial F}{\partial \phi_x} = k\bar{I}_x \quad , \quad I_z = \frac{\partial F}{\partial \phi_z} = l\bar{I}_x + \bar{I}_z, \tag{60}$$

and the transformed Hamiltonian $\bar{H}$ is

$$\bar{H}(\bar{I}_x, \bar{I}_z, \bar{\phi_x}) = (kQ_{x0} + lQ_{z0} - p)\bar{I}_x + \bar{I}_z Q_{z0} + \bar{g}(\bar{I}_x, \bar{I}_z) + \bar{h}(\bar{I}_x, \bar{I}_z)\cos(\bar{\phi_x}). \tag{61}$$

The barred functions $\bar{g}$ and $\bar{h}$ are related to the old ones by

$$\bar{g}(\bar{I}_x, \bar{I}_z) \equiv g(k\bar{I}_x, l\bar{I}_x + \bar{I}_z) = g(I_x, I_z) \tag{62}$$

$$\bar{h}(\bar{I}_x, \bar{I}_z) \equiv h(k\bar{I}_x, l\bar{I}_x + \bar{I}_z) = h(I_x, I_z). \tag{63}$$

The new Hamiltonian virtually describes a system of one degree of freedom because the action $\bar{I}_z$ is an invariant of the motion. The $\bar{I}_z$-$\bar{\phi}_z$-plane will, therefore, be disregarded in our further discussion. In the remaining $\bar{I}_x$-$\bar{\phi}_x$-plane the motion close to the resonance is approximated by a nonlinear pendulum similar to Eq. (11),

$$\bar{K}(\bar{\Delta}, \bar{\tilde{\phi}}) = \frac{1}{2}\frac{d^2\bar{g}}{d\bar{I}_x^2}(\bar{I}_{x,r}, \bar{I}_{z,r})\bar{\Delta}_x^2 + \bar{h}(\bar{I}_{x,r}, \bar{I}_{z,r})\cos\bar{\phi}_x, \tag{64}$$

where we have defined the new momentum $\bar{\Delta}_x$ to be the deviation from the resonant value,

$$\bar{\Delta}_x = \bar{I}_x - \bar{I}_{x,r}. \tag{65}$$

This pendulum equation is almost the same as that derived by a different approach in Ref. 32. According to Eq. (13) the island tune of a resonance for two degrees of freedom is given by

$$\begin{aligned} Q_{I,2d} &= \sqrt{\frac{\partial^2\bar{g}(\bar{I}_x, \bar{I}_z)}{\partial\bar{I}_x^2}\bar{h}(\bar{I}_x, \bar{I}_z)} \\ &= \sqrt{\left[k^2\frac{\partial^2 g(I_{x,r}, I_{z,r})}{\partial I_x^2} + 2kl\frac{\partial^2 g(I_{x,r}, I_{z,r})}{\partial I_x I_z} + l^2\frac{\partial^2 g(I_{x,r}, I_{z,r})}{\partial I_z^2}\right] h(I_{x,r}, I_{z,r})}, \end{aligned} \tag{66}$$

where use has been made of Eqs. (62) and (63) to convert the expression to the original variables.

As usual the total width of the resonance island is deduced from the pendulum Hamiltonian (see also Eq. (12)):

$$\Delta\bar{I}_{x,\,\mathrm{tot}} = 2\bar{\Delta}_{x,max} = 4\sqrt{\left|\frac{\bar{h}(\bar{I}_{x,r}, \bar{I}_{z,r})}{\frac{\partial^2\bar{g}}{\partial\bar{I}_{x,r}^2}(\bar{I}_{x,r}, \bar{I}_{z,r})}\right|}. \tag{67}$$

The translation into the original action space with the help of the transformation in Eq. (60) gives

$$\Delta I_{\rm tot} = \sqrt{\Delta I_x^2 + \Delta I_z^2} = \sqrt{l^2 + k^2}\, \Delta \bar{I}_{x,\,\rm tot}. \tag{68}$$

Hence the total island width for two degrees of freedom is

$$\Delta I_{\rm tot} = \frac{4 Q_{I,2d} \sqrt{l^2 + k^2}}{|l^2 \frac{\partial^2 g}{\partial I_z^2} + 2kl \frac{\partial^2 g}{\partial I_x \partial I_z} + k^2 \frac{\partial^2 g}{\partial I_x^2}|}. \tag{69}$$

Tune modulation is introduced in analogy to Eq. (15). An additional term linear in $I_{x,z}$ is added to the single-resonance Hamiltonian of Eq. (57), yielding

$$\begin{aligned} H(I_x, I_z, \phi_x, \phi_z, \theta) &= I_x Q_{x0} + I_z Q_{z0} + g(I_x, I_z) + h(I_x, I_z) \cos(k\phi_x + l\phi_z - p\theta) + \\ &\quad + q(I_x + I_z) \cos(Q_m \theta + \alpha), \end{aligned} \tag{70}$$

where we have assumed, for simplicity, that both tunes are modulated with the same frequency Q_m and amplitude q. Performing the same canonical transformation as above the pendulum approximation leads to (compare to Eq. (17))

$$\bar{K}(\bar{\Delta}, \bar{\tilde{\phi}}, \theta) = \frac{1}{2} \frac{d^2 \bar{g}}{d \bar{I}_x^2} (\bar{I}_{x,r}, \bar{I}_{z,r}) \bar{\Delta}_x^2 + h(\bar{I}_{x,r}, \bar{I}_{z,r}) \cos \bar{\phi}_x + q \bar{\Delta}_x (k + l) \cos(Q_m \theta + \alpha). \tag{71}$$

Under our assumption that both tunes are modulated with the same frequency Q_m and amplitude q, Eqs. (21),(24),(56), and (50) are still valid if one uses the general island tune of Eq. (66) and if one replaces n by $k + l$. The latter substitution indicates that difference resonances are less affected by the tune modulation than are sum resonances.

The mean emittance growth in the chaotic region close to a single resonance has been calculated for one degree of freedom in section 3.7, Eq. (34). It can easily be generalized to two degrees of freedom, and is then

$$\frac{\overline{(\Delta(\epsilon_x + \epsilon_z))^2}}{\Delta t} = 32 \frac{f_{rev} (k + l) h^2 (I_{x,r}, I_{z,r})}{q}. \tag{72}$$

Again we find that only the substitution $n \to k + l$ is required to generalize the result for one degree of freedom.

3.8. Width of the Stochastic Layer

The effect of tune modulation as a function of resonance order, island tune, modulation amplitude, and modulation frequency can be estimated in an alternative way. The basic procedure, developed in Ref. 26, is to construct a discrete mapping for the motion near the separatrix. The threshold of chaos for this map yields the width of the stochastic layer, which is

a quantitative measure of the chaotic part of the phase space close to a resonance. Our starting point is a Hamiltonian of the form of Eq. (71):

$$H(\Delta,\phi,\theta)=\frac{1}{2}\frac{d^2g}{dI^2}\Delta^2-h\cos\phi+q(k+l)\Delta\cos(Q_m\theta+\alpha). \tag{73}$$

The unperturbed Hamiltonian

$$H_0(\Delta,\phi)=\frac{1}{2}\frac{d^2g}{dI^2}\Delta^2-h\cos\phi \tag{74}$$

has stable fixed points at $(\phi=2k\pi,\Delta=0)$ and unstable fixed points at $(\phi=(2k+1)\pi,\Delta=0)$. The motion on the separatrix is given by[33]

$$\phi_{sx}=4\arctan e^{Q_I\theta}-\pi, \tag{75}$$

where we have used the island tune defined in Eq. (13). The change in H_0 during a half period of the oscillation can be approximated by integrating $dH_0/d\theta\equiv[H_0,q\cdot(k+l)\cdot\Delta\cos(Q_m\theta+\alpha)]$ along the separatrix trajectory, which is denoted by the subscript 'sx':

$$\begin{aligned}\Delta H_0 &\approx h\frac{(k+l)q}{2}\int_{-\infty}^{\infty}d\theta[\sin(\phi_{sx}-Q_m\theta-\alpha)+\sin(\phi_{sx}+Q_m\theta+\alpha)] &(76)\\ &= h\frac{(k+l)q}{2Q_m}\kappa\int_{-\infty}^{\infty}ds[\sin(\phi_{sx}-\kappa s-\alpha)+\sin(\phi_{sx}+\kappa s+\alpha)] &(77)\\ &= -h\frac{(k+l)q}{2Q_m}\kappa\sin\alpha\int_{-\infty}^{\infty}ds[\cos(\phi_{sx}-\kappa s)-\cos(\phi_{sx}+\kappa s)]. &(78)\end{aligned}$$

Here we have changed the integration variable from θ to $s=\theta\cdot Q_I$ and have introduced the dimensionless quantity

$$\kappa\equiv\frac{Q_m}{Q_I}. \tag{79}$$

The integrals on the right hand side are known as Melnikov-Arnold integrals $\mathcal{A}_2(\kappa)$, $\mathcal{A}_2(-\kappa)$[26, 33, 34, 35] and can be evaluated (see Ref. 6). We are then led to the following solution:

$$\Delta H_0=-h\kappa\frac{(k+l)q}{2Q_m}\cdot(\mathcal{A}_2(\kappa)-\mathcal{A}_2(-\kappa))\cdot\sin\alpha. \tag{80}$$

Denoting the relative energy deviation from the separatrix by w,

$$w\equiv\frac{H_0-h}{h},$$

and Eq. (80) can also be written as

$$\bar{w}=w-\kappa\frac{(k+l)q}{2Q_m}\cdot(\mathcal{A}_2(\kappa)-\mathcal{A}_2(-\kappa))\cdot\sin\alpha. \tag{81}$$

A canonical variable conjugate to w is the phase α. In order to construct a map the change in α also has to be calculated. The oscillation frequency in the vicinity of the separatrix is given by[26]

$$Q(w) \approx \frac{\pi Q_I}{\ln(\frac{32}{|w|})}. \tag{82}$$

Hence the change of α during a half period of the oscillation is

$$\bar{\alpha} \approx \alpha + \pi \frac{Q_m}{Q(\bar{w})} \approx \alpha + \frac{Q_m}{Q_I} \ln \frac{32}{|\bar{w}|}. \tag{83}$$

Note that the argument of the logarithm is the transformed variable $\bar{w}$ and not the initial w, which means that Eqs. (81) and (83) are applied successively. The Jacobian determinant of either part is one, and therefore the total map is symplectic. The trace of the Jacobian matrix for this map is calculated as

$$\mathrm{Tr} J(\alpha, w) = 2 + f \frac{\kappa}{|\bar{w}|} \cos \alpha, \tag{84}$$

with the abbreviation

$$f \equiv \frac{(k+l)q}{2Q_I} (\mathcal{A}_2(\kappa) - \mathcal{A}_2(-\kappa)). \tag{85}$$

A fixed point is stable if the absolute value of the trace is smaller than 2; otherwise it is unstable. In our case the fixed points are given by (with m_r and n_r being natural numbers)

$$\begin{aligned} |w_r| &= 32 \cdot e^{-\frac{2\pi m_r}{\kappa}} \\ \alpha_r &= n_r \pi. \end{aligned} \tag{86}$$

If f is a positive quantity, the fixed points $\alpha = n_r \pi$ with n_r even are always unstable. However for an uneven n_r instability occurs only if

$$|w| < \frac{\kappa f}{4}. \tag{87}$$

In order to proceed further we have to insert the solution of the Melnikov-Arnold integral $\mathcal{A}_2$,[26, 33, 6]

$$\mathcal{A}_2(\kappa) = 4\pi\kappa \frac{e^{\frac{\pi\kappa}{2}}}{\sinh(\pi\kappa)}, \tag{88}$$

into Eq. (85). According to Eq. (87) the width of the stochastic layer is then written as

$$w_{sl} = \pi \kappa^3 \frac{(k+l)q}{Q_m} \frac{\sinh(\frac{\pi\kappa}{2})}{\sinh(\pi\kappa)}. \tag{89}$$

The value of w_{sl} is proportional to the fraction of area of the resonance island which becomes chaotic due to the external tune modulation. For a large ratio $Q_m/Q_I \equiv \kappa \gg 1$, the width of the chaotic layer decreases exponentially as a function of the modulation frequency.

Instead of founding our argumentation on the stability of the fixed points we can derive the width of the stochastic layer in an alternative way. If f defined by Eq. (85) is sufficiently small, it is possible to linearize the mapping in w (but not in α) around a resonant value w_r. Equations (81) and (83) are then transformed into

$$\begin{aligned} \bar{I} &= I + K \sin\alpha \qquad (90) \\ \bar{\alpha} &= \alpha + \bar{I}, \qquad (91) \end{aligned}$$

where we have introduced the new variable

$$I \equiv -\kappa \left(\frac{w - w_r}{w_r} \right) \qquad (92)$$

and the parameter

$$K \equiv \frac{\kappa f}{w_r}. \qquad (93)$$

Equations (90) and (91) constitute the 'standard mapping', which is of fundamental importance in the theory of nonlinear resonances. The onset of global chaos for this mapping occurs at a critical value $K \approx 1$.[26] Hence the width of the stochastic layer is approximately

$$|w_{sl}| \approx \kappa f, \qquad (94)$$

which differs from Eq. (87) only by a factor of 4. In the following we will take the geometric mean of Eqs. (89) and (94). Noting that

$$w_I \equiv \frac{\Delta I_{sl}}{\Delta I_{\mathrm{tot}}} \approx \frac{1}{2} w_{sl}, \qquad (95)$$

in the following we will drop all subscripts and use the symbol w (understood to be w_I) for the expression on the right hand side of Eq. (89).

It should be mentioned that Eq. (89) may be completely valid only in the limit of large modulation frequencies, since we have ignored an oscillating term (as a function of modulation frequency) caused by the discrete locations of fixed points in Eq. (86).[26]

3.9. Phase Diagrams

In the parameter space of tune modulation, areas with distinct dynamical behavior can be graphically represented, which leads to 'phase diagrams' as proposed in Ref. 23. The borderlines given by the inequalities in Eqs. (24) and (56),

$$\begin{aligned} \frac{Q_m^{\frac{3}{4}} (nq)^{\frac{1}{4}}}{Q_I} &= \frac{4}{\pi^{\frac{1}{4}}} \\ \left| \frac{q Q_m}{Q_I^2 - Q_m^2} \right| &= \frac{1}{n}. \end{aligned} \qquad (96)$$

describe approximate boundaries between regions with qualitatively different behavior in the (q, Q_m)-plane. The unperturbed system is defined by only two parameters, the island tune Q_I and the order n of the resonance [¶]. A typical phase diagram is shown in Fig. 9 (solid curves), for the values $Q_I = 0.049$ and $n = 4$ of the octupole kick map studied in Section 3.10. The four different regions in the phase diagram can be interpreted as follows:

1. At small modulation amplitudes and small modulation frequencies, the tune change is adiabatic, and the particles are stable.

2. For small modulation amplitudes and large modulation frequencies the sideband islands cover only a very small fraction of phase space. Thus the majority of particles are not affected by the tune modulation. This region is characterized by 'rapid phase oscillations'.

3. If the modulation amplitude is increased, the sideband islands gain importance. For large modulation frequency these islands are separated from each other, and the motion is still regular.

4. For large modulation amplitudes the sidebands start to overlap below some critical modulation frequency, giving rise to global chaos. It is this region of the phase diagram (in the upper left corner) where emittance growth processes and proton losses occur.

The particle loss is due to a 'diffusion' process in the chaotic region, which is described by Eq. (34):

$$\frac{\overline{(\Delta\epsilon)^2}}{\Delta t} = 32 \frac{f_{rev} n h^2(I_r)}{q}. \tag{97}$$

The local diffusion rate is independent of the modulation frequency.

We now propose a complementary phase diagram, which is derived from Eq. (89):

$$w \equiv \pi n q \frac{Q_m^2}{Q_I^3} \frac{\sinh(\frac{\pi Q_m}{2Q_I})}{\sinh(\frac{\pi Q_m}{Q_I})} \stackrel{!}{=} w_0. \tag{98}$$

The contour line $w = w_0$, for a properly chosen constant w_0, can be used to define a border between chaotic and regular regions. Contour lines for $w_0 = 0.05, 0.1, 0.2$, and 0.3 are shown as dotted curves in Fig. 9. While the chaotic regions predicted by Eqs. (96) and (98) agree approximately, there are still a few important differences:

a) Equation (96) describes a resonance-like behavior at $Q_m \approx Q_I$, whereas according to Eq. (98), the modulation amplitude has to exceed a certain threshold to be harmful. The prediction of Eq. (96) that an arbitrarily small modulation amplitude may cause global chaos seems to be unrealistic.

[¶] As mentioned, in the more general two-dimensional case n has to be replaced by $k + l$.

Figure 9: Phase diagram for the island tune $Q_I = 0.049$ and the resonance order $n = 4$ according to Eq. (96) (solid curves) and contour lines using Eq. (98) with $w = 0.05, 0.1, 0.2, 0.3$ (dotted lines). The small closed and open circles refer to strongly chaotic and almost undisturbed cases, respectively, as found in simulation studies with an octupole kick map (Section 3.10). The phase space diagrams corresponding to the circles (from left to right) are depicted in Figs. 10b–j and 13a–f.

b) The maximum response to tune modulation is either at $Q_m = Q_I$ from Eq. (96), or at $Q_m \approx 1.35 \cdot Q_I$ (maximum value of width w in Eq. (98)).

c) The boundary of the chaotic region is defined by only one equation if one applies the stochastic layer argumentation of Eq. (98).

The effect of tune modulation on a simple octupole kick map is examined in the next section in order to study these questions more deeply.

3.10. Octupole Kick Map

The two-dimensional map that we want to study consists of a rotation

$$\begin{pmatrix} x \\ p \end{pmatrix}_f = \begin{pmatrix} \cos 2\pi Q & \sin 2\pi Q \\ -\sin 2\pi Q & \cos 2\pi Q \end{pmatrix} \begin{pmatrix} x \\ p \end{pmatrix}_i \tag{99}$$

and an octupolar kick

$$p_f = p_i - x_i^3. \tag{100}$$

The equivalent Hamiltonian is

$$H(x,p,\theta) = \frac{1}{2}Q(x^2+p^2) + \frac{1}{4}x^4\delta(\theta). \tag{101}$$

Action and angle variables I and ϕ are introduced by the usual relations

$$x = \sqrt{2I}\cos\phi \qquad \text{and} \qquad p = -\sqrt{2I}\sin\phi. \tag{102}$$

Near the fourth integer resonance $4Q \approx 1$ the total Hamiltonian is approximated by

$$H(I,\tilde{\phi}) \approx \left(Q - \frac{1}{4}\right) I + \frac{3}{16\pi}I^2 + \frac{1}{16\pi}I^2\cos(4\tilde{\phi}). \tag{103}$$

We readily identify the characteristic quantities

$$g(I) = \frac{3}{16\pi}I^2 \tag{104}$$

$$h(I) = \frac{1}{16\pi}I^2 \tag{105}$$

$$n = 4. \tag{106}$$

Choosing $Q = 0.23$, the resonant action value is $I_r = 4\pi(\frac{1}{4} - Q) \approx 0.25$, and the island tune is approximately

$$Q_I = n\sqrt{\frac{d^2g}{dI^2}(I_r)h(I_r)} \approx 0.049. \tag{107}$$

The phase diagram of this situation is shown in Fig. 9. We investigate two special cases. First, we examine the behavior for the comparatively small modulation amplitude $q = 0.002$. Figure 10 presents phase space diagrams for ten different modulation frequencies. Each diagram shows six different trajectories plotted once every modulation period (stroboscopic plot). The corresponding positions in the phase diagram are indicated by the lower row of circles in Fig. 9. It is evident from the diagrams that the small angle boundary of Eq. (96) considerably underestimates the size of the chaotic region: The second part of Eq. (96) predicts chaos only in the very small range $0.045 < Q_m < 0.053$. However, chaotic trajectories occupy large phase-space areas for roughly $\frac{1}{4}Q_I < Q_m < 4Q_I$. These limits would be described by Eq. (98) with $w_0 \approx 0.01$ as can be seen from Fig. 11 depicting the stochastic width of Eq. (98) as a function of the modulation frequency. The stochastic width w is maximal at $Q_m \approx 0.066$ and thus is in a region which should be regular according to Eq. (96).

Another point of interest is the border derived from the resonance overlap criterion of Eq. (24). We choose the modulation amplitude $q = 0.05$, which is larger than the value $q^* \approx 0.033$ at the intersection of the two phase boundary lines in Eq. (96). Figure 12 shows the width of the stochastic layer as a function of the modulation frequency for this value of q.

Figure 10: Phase space diagrams of six trajectories for the octupole kick maps of Eqs. (99) and (100) with a tune modulation amplitude $q = 0.002$; each diagram corresponds to a different modulation frequency Q_m: a) no modulation b) $Q_m = 0.005$, c) $Q_m = 0.01 \approx \frac{1}{5}Q_I$, d) $Q_m = 0.02$, e) $Q_m = 0.04$, f) $Q_m = 0.05 \approx Q_I$, g) $Q_m = 0.06$, h) $Q_m = 0.1$, i) $Q_m = 0.2 \approx 4Q_I$, and j) $Q_m = 0.5$.

Figure 11: Width w of the stochastic layer, Eq. (98), for the simple octupole kick maps of Eqs. (99) and (100), with a modulation amplitude $q = 0.002$, as a function of the modulation frequency Q_m. The open and closed circles refer to the almost undisturbed and to the strongly chaotic phase space diagrams in Figs. 10b–j, respectively.

In Fig. 12 the chaotic width w becomes too large at modulation frequencies close to the island tune for the predicted value to be accurate. Since the stochastic layer extends to both sides of the separatrix, only half of it lies inside the resonance island. A reasonable upper limit for the parameter w is therefore 2, which would describe a situation in which the complete resonance island is chaotic. Hence the range of validity of Eq. (89) is restricted in a self-consistent way to values of w smaller than 2. Far from the separatrix it is no longer possible to approximate the motion by integrating along the separatrix, which was the basic assumption.

Figure 13 shows phase space diagrams for six different modulation frequencies and a constant modulation amplitude $q = 0.05$. Due to the larger value of q, chaotic particles are lost almost immediately, which leads to a somewhat distinct appearance of the phase space diagrams as compared to Fig. 10. The change from chaotic to regular motion occurs at about $Q_m \approx 0.25$. In view of Fig. 12, this threshold could be described by Eq. (98) with $w_0 \approx 0.1$, whereas the first part of Eq. (96) predicts the border of global chaos already at $Q_m \approx 0.133$. The six cases examined in Fig. 13 are represented by the upper row of circles in the phase diagram, Fig. 9. It may be concluded that Eq. (98) represents the border of the chaotic region at least as accurately as Eq. (96).

The reader may have noticed, from Figs. 10–13, that in many cases the fraction of the resonance island destroyed by the tune modulation agrees with Eq. (98) only within a factor

Figure 12: Width w of the stochastic layer, Eq. (98), for the simple octupole kick maps, Eqs. (99) and (100), with a tune modulation amplitude $q = 0.05$, as a function of the modulation frequency Q_m. The open and closed circles refer to the almost undisturbed and to the strongly chaotic phase space diagrams in Figs. 13b–f, respectively.

5–10, where the deviations are both towards too high and too low values. Therefore, it is desirable to estimate the magnitude of the deviation to be expected for a typical resonance in HERA and thus of the error in the results of Section 2.

It has been pointed out[36] that Eqs. (96) and (98), describing alternative borders in a phase diagram, can be expressed in terms of two quantities, a 'scaled' modulation amplitude $\tilde{q} \equiv nq/Q_m$ and a 'scaled' modulation frequency $\tilde{Q}_m \equiv \kappa \equiv Q_m/Q_I$. Simulations provide strong evidence that the degree of chaos is indeed characterized by the two universal parameters $\tilde{q}$ and $\tilde{Q}_m$ and does not depend on the actual values of n and Q_I. Assuming parameters representative for HERA (see Section 2), here labeled by the superscript H,

$$\begin{aligned} n^H &= 10, \\ Q_I^H &\approx 2 \cdot 10^{-4}, \\ Q_m^H &\approx 10^{-3}, \\ q^H &\approx 10^{-4}, \end{aligned}$$

the scaled parameters are $\tilde{q}^H \approx 1$ and $\tilde{Q}_m^H \approx 5$. The phase space diagram of Fig. 13d corresponds to nearly these values, namely to $\tilde{q} \approx 1$ and $\tilde{Q}_m \approx 4$. For this case, Fig. 12 predicts a chaotic

Figure 13: Phase space diagrams of six trajectories for the octupole kick maps, Eqs. (99) and (100), with a tune modulation amplitude $q = 0.05$; each diagram corresponds to a different modulation frequency Q_m: a) $Q_m = 0.05 \approx Q_I$, b) $Q_m = 0.1$, c) $Q_m = 0.125$, d) $Q_m = 0.2$, e) $Q_m = 0.25 \approx 5Q_I$, and f) $Q_m = 0.5$.

region whose size is about 40% of the undisturbed island. From comparison of the phase space diagrams in Figs. 13d and f, about 60–70% of the island is actually destroyed in Fig. 13d. The island tune Q_I for most of the resonances in HERA is smaller than the assumed value $Q_I^H \approx 2 \cdot 10^{-4}$. Fortunately, for a larger ratio Q_m^H/Q_I^H the error of Eq. (98) decreases. This is illustrated by Fig. 13e, for which the stochastic width is about 15%, in good agreement with Fig. 12. It may, therefore, be expected that, in the results for HERA presented in Section 2, the error of w is not larger than a factor of 2.

4. Modulation Amplitudes

4.1. Origin of Power Supply Ripple

A major source of tune modulation in a storage ring is magnetic field modulations caused by voltage ripple of the magnet power supplies. The voltage ripple is partly due to the design of the rectifiers and partly due to technical imperfections.

The superconducting correction coils in HERA are fed by switched mode power supplies (chopper). These are built as converters on the basis of a pulse width modulation and are driven at a frequency of 14 kHz.[37] Due to the very high frequency, their effect on the beam dynamics is negligible, provided that the fractional part of the betatron tune is not too close to the driving frequency of the power supplies, which corresponds to $Q_m \approx 0.296$.

For magnets or magnet chains which are operated at a current higher than $360A$, rectifiers with thyristor bridges are used. The main superconducting circuit is fed by a 24-pulse 4-bridge silicon controlled rectifier (SCR). The expected fundamental ripple frequency is 12 kHz for a perfect balance of the bridge circuit. Due to imbalances between individual bridges and thyristors, and due to capacitances to ground all harmonics of the fundamental frequency, 50 Hz are found in the voltage spectra of the SCRs.

4.2. Simple Model of the Main Circuit

In the HERA ring all superconducting dipoles and quadrupoles are powered in series. Consequently, a current ripple in the main circuit changes the focusing strength of the quadrupoles as well as the deflecting dipole field. A change in the dipole field leads to a shift in energy and beam orbit. In the arcs the corresponding shift of the tune is compensated by the simultaneous change of the quadrupole strengths. Independent power supplies feed the normal-conducting quadrupoles in the straight sections. Therefore the compensation of the dipole and the quadrupole field variations is not perfect, and a net tune modulation results.

To illuminate the relation between power supply ripple and tune modulation, a simplified model of a current ripple $\frac{\Delta I}{I}\cos(\omega_{ripple}t)$ with constant amplitude and phase along the superconducting magnet chain is considered. Three effects contribute to the effective tune modulation, namely

1. the absolute change of the momentum,
2. the orbit change at the position of the sextupoles,
3. the change of the focusing strength of the quadrupoles.

For a low-frequency ripple, $\omega_{ripple} \ll \omega_{sync}$, the energy of the particles follows the change in the external field. The revolution frequency stays constant because the radio frequency in the cavities is not changed. Hence the change in the velocity is compensated by a change in the path length, and we have

$$\frac{\Delta C}{C} = \frac{\Delta v}{v} = \frac{1}{\gamma^2}\frac{\Delta p}{p},$$

where γ is the relativistic $\gamma \equiv (1 - \frac{v^2}{c^2})^{-\frac{1}{2}}$. The relative change in the orbit length is

$$\frac{\Delta C}{C} = \frac{1}{\gamma_{tr}^2} \left(\frac{\Delta p}{p} - \frac{\Delta B}{B} \right).$$

In this section the ripple of the guide field $\frac{\Delta B}{B}$ is assumed to be equal to the current ripple $\frac{\Delta I}{I}$. The transition energy γ_{tr} is the nominal energy at which the change in path length exactly compensates for the change in velocity for off-momentum particles. For HERA its value is $\gamma_{tr} \approx 27.7$. The last two equations lead to

$$\frac{\Delta p}{p} = \frac{\gamma^2}{\gamma^2 - \gamma_{tr}^2} \frac{\Delta B}{B}. \tag{108}$$

If there were no sextupole coils in the ring, the absolute change in momentum would give rise to a tune modulation amplitude q_I via the natural total chromaticity $\xi_{nat.}^{tot}$:

$$q_I = \xi_{nat.}^{tot} \frac{\Delta p}{p} = \xi_{nat.}^{tot} \frac{\gamma^2}{\gamma^2 - \gamma_{tr}^2} \frac{\Delta B}{B}, \tag{109}$$

the chromaticity ξ being defined as the change in tune ΔQ per relative momentum deviation,

$$\xi \equiv \frac{\Delta Q}{\Delta p / p}. \tag{110}$$

The 'natural' chromaticity $\xi_{nat.}$ is caused by the variation with momentum of the quadrupole focusing strength. It can be expressed as an integral of the quadrupole strength K in units of m^{-2} times the beta function β around the ring,

$$\xi_{nat.}^{tot} \equiv -\frac{1}{4\pi} \oint K \beta \, ds.$$

Sextupole correction coils and sextupole field errors in the superconducting magnets provide a second contribution to the overall chromaticity, which is of opposite sign. The effective sextupole strength around the ring is adjusted such that the total chromaticity

$$\xi^{tot} = \xi_{nat.}^{tot} + \frac{1}{4\pi} \oint m D \beta \, ds \tag{111}$$

is close to zero, m being the sextupole strength in units of m^{-3} and D the dispersion function. Hence the horizontal orbit shift in the sextupoles, given by

$$x = D \left(\frac{\Delta p}{p} - \frac{\Delta B}{B} \right) = D \frac{\gamma_{tr}^2}{\gamma^2 - \gamma_{tr}^2} \frac{\Delta B}{B},$$

causes a modulation amplitude q_{II}, which can be written as

$$q_{II} = -\xi_{nat.}^{tot} \frac{\gamma_{tr}^2}{\gamma^2 - \gamma_{tr}^2} \frac{\Delta B}{B}. \tag{112}$$

It is convenient to decompose the total natural chromaticity into two parts,

$$\xi_{nat.}^{tot} = \xi_{nat.}^{straight} + \xi_{nat.}^{arc}, \tag{113}$$

by means of which the effect of the warm quadrupoles in the straight sections is separated from that of the superconducting quadrupoles in the arcs. The modulation of the focusing strength of the superconducting quadrupoles leads to a modulation amplitude q_{III},

$$q_{III} = \frac{1}{4\pi} \int_{arc} K\beta \, ds \, \frac{\Delta B}{B} = -\xi_{nat.}^{arc} \frac{\Delta B}{B}. \tag{114}$$

Adding Eqs. (109), (112), and (114) the total modulation amplitude q becomes

$$q = |q_I + q_{II} + q_{III}| = |\xi_{nat.}^{straight}| \frac{\Delta B}{B} \qquad \text{for} \qquad \omega_{ripple} \ll \omega_{sync}. \tag{115}$$

For frequencies larger than the synchrotron frequency, $\omega_{ripple} \gg \omega_{sync}$, the momentum is approximately constant $\Delta p \approx 0$. Hence, in this case, there is no contribution to the modulation amplitude of the form q_I from Eq. (109). The horizontal orbit change is simply

$$x = -D \frac{\Delta B}{B},$$

and q_{II} in Eq. (112) has to be replaced by

$$q_{IV} = \xi_{nat.}^{tot} \frac{\Delta B}{B}, \tag{116}$$

while q_{III} from Eq. (114) also applies to a high-frequency ripple. The total tune modulation amplitude

$$q = |q_{III} + q_{IV}| = |\xi_{nat.}^{straight}| \frac{\Delta B}{B} \qquad \text{for} \qquad \omega_{ripple} \gg \omega_{sync} \tag{117}$$

is the same as for a low-frequency ripple (Eq. (115)).

In the HERA proton ring the natural chromaticities at injection energy are about

$$\xi_{nat.}^{tot} = \xi_{nat.}^{arc} + \xi_{nat.}^{straight} \approx -40, \quad \xi_{nat.}^{arc} \approx -30, \quad \text{and} \quad \xi_{nat.}^{straight} \approx -10. \tag{118}$$

In our simple model, the relation between current ripple and tune modulation amplitude is

$$q \approx |\xi_{nat.}^{straight}| \cdot \frac{\Delta B}{B} \approx 10 \cdot \frac{\Delta B}{B}. \tag{119}$$

The amplitude of the 150-Hz field ripple measured in the reference dipole magnets is $\Delta B/B \approx 1.4 \cdot 10^{-6}$ and corresponds to a tune modulation amplitude $q \sim 1.4 \cdot 10^{-5}$, according to Eq. (119). In reality the amplitude of the current ripple is not constant around the ring, and the overall modulation amplitude q is a factor of 3–4 larger (see next section).

It is difficult to relate the observed field ripple to the voltage ripple at the power supply. For example, using $L_{tot} \approx 24$H the estimate $\Delta U = \omega L_{tot} I \frac{\Delta B}{B}$ results in $\Delta U \approx 8V$. In contrast, the power supply specifications allow a maximum ripple amplitude of only 2 Volts.[38] Direct measurements at the power supply show that the actual ripple amplitude is even smaller, on the order of 150 mV.[39] Thus an RL-circuit is not an adequate model to describe the superconducting magnet chain.

Figure 14: Tune modulation amplitude at injection energy as a function of the ripple frequency for a voltage ripple of 1 V at the power supply.[40]

4.3. Transmission Line Characteristics

In order to properly estimate the actual effect of the magnetic field ripple, the transmission line characteristics of the superconducting magnet string have to be considered. For every ripple frequency a wave pattern builds up along the magnet chain. The corresponding current ripple amplitude at each position in the ring can be computed from the measured 4-pole parameters of dipole and quadrupole magnets. As far as the contribution to the overall tune modulation is concerned the ripple effects in different quadrupole and sextupole magnets partially add and partially cancel each other.

In Fig. 14 the tune modulation amplitude expected for a harmonic power supply voltage ripple of amplitude 1 V is shown as a function of the ripple frequency.[40] The amplitude of the 50-Hz ripple was measured to be about 50 mV, which, according to Fig. 14, translates into a tune modulation amplitude of $q \sim 3 \cdot 10^{-5}$. The 150-Hz voltage ripple of 150 mV gives rise to a tune modulation of amplitude $q \sim 5 \cdot 10^{-5}$. The large enhancement of the effect of a power supply ripple between 0 and 300 Hz, illustrated by Fig. 14, is related to standing wave resonances of the magnet string, which occur at frequencies as low as 15.6 Hz. According to model calculations[41] the eigenmodes of the transmission line may be excited during the ramp. Such an excitation has not yet been measured.

4.4. Shielding by the Beam Pipe

The inside of the cold HERA beam pipe is coated with a copper layer of thickness $d = 10\,\mu$m at a radius $r = 27.5$ mm. This layer provides most of the shielding, which can be calculated by solving

Maxwell's equations with the appropriate boundary conditions.[42, 43] The frequency-dependent skin depth is given by

$$\delta(f) = \frac{1}{\sqrt{\pi f \mu_0 \sigma}} \,. \tag{120}$$

The 'shielding factor' $\tilde{Q} \equiv B_{\rm inside}/B_{\rm outside}$ is defined to be the ratio of the magnetic field inside the beam pipe to the field a great distance from it, which is assumed to be homogeneous. Introducing the two abbreviations

$$\begin{aligned} k(f) &\equiv \frac{1+i}{\delta(f)} \\ K(f) &\equiv k(f)\cdot(r-d)\,, \end{aligned}$$

the shielding factor can be written in complex form as[42, 43]

$$\tilde{Q}(f) = \left[\cosh(k(f)\cdot d) + 0.5\left[K(f) + \frac{1}{K(f)}\right]\cdot\sinh(k(f)\cdot d)\right]^{-1} \,. \tag{121}$$

In Fig. 15a the absolute value of $\tilde{Q}(f)$ is plotted in the frequency range 0–15 kHz assuming a conductivity $\sigma_{\rm copper} \approx 4\cdot 10^9 \frac{1}{\Omega{\rm m}}$ at liquid helium temperature.[44] At 150 Hz, the attenuation factor is only 0.8.

The warm sections of the beam pipe are not coated by copper, but consist of 2-mm-thick stainless steel with a conductivity of $\sigma \approx 3\cdot 10^6 \frac{1}{\Omega{\rm m}}$.[44] At the position of the interaction-region quadrupoles (QR10,QR14) the average beam pipe radius is $r = 29.5$ mm. Figure 15b shows that in the frequency range of interest, between 0 and 600 Hz, the warm beam pipe provides virtually no shielding.

4.5. Ground Motion Effects

A tune modulation of low frequency can be caused by ground waves and mechanical vibrations of the magnets. The amplitude of the beam oscillations due to these effects and the impact on collision alignment in HERA have been the object of vigorous investigations.[45] One may suspect that a part of the low-frequency beam oscillations results in a harmonic tune modulation due to an orbit change at the position of the sextupoles. For instance, assuming a root-mean-square orbit displacement in the arc of $x_{\rm rms} = 0.05$ mm caused by mechanical quadrupole vibrations, a rough estimate of the resulting modulation amplitude is

$$q_{vibration} \approx |\xi_{nat.}| \frac{Q - \{Q\}}{Q} \frac{x_{\rm rms}}{D\sqrt{N_{quad}}}, \tag{122}$$

where D is the average dispersion function (about 1.5 m), N_{quad} the number of quadrupoles, $\xi_{nat.} \approx -40$ the natural chromaticity, and $Q - \{Q\}$ the fractional part of the betatron tune Q.

The factor $(Q - \{Q\})/Q$ accounts for the oscillatory character of the closed orbit distortions. Over every full betatron wavelength the accumulated tune shift is zero, because

Figure 15: Shielding factor $|\tilde{Q}|$ as a function of frequency in Hz for the HERA beam pipe: a) cold beam pipe with $d = 10\mu m$ copper plating, b) warm beam pipe consisting of $d = 2mm$ stainless steel.

orbit displacements of opposite sign in a sextupole compensate for each other. Thus in a first approximation only the fractional part of the tune, which corresponds to an incomplete closed orbit oscillation, gives rise to a tune shift. For a typical working point of $Q \approx 31.3$ the suppression factor is about $0.3/31 \approx 10^{-2}$. The square root of the number of quadrupoles ($N_{quad} \approx 200$) enters in Eq. (122) if there is no correlation between the individual magnets. A typical number is $q = 10^{-6}$, which is a factor of 100 smaller than the modulation amplitudes due to power supply ripple. The dominant frequencies are in the range 2–20 Hz.[45]

4.6. Synchrotron Oscillations and Nonzero Chromaticity

The effect of synchrotron motion and nonzero chromaticity may to first order be approximated by the accompanying tune modulation in the transverse phase space. A typical modulation amplitude is $q \approx 2 \cdot 10^{-4}$ (assuming a relative energy deviation $\delta \approx 2 \cdot 10^{-4}$ and a chromaticity $\xi \equiv \Delta Q / \frac{\Delta p}{p} \approx 1$). The synchrotron frequency of about about 20 Hz corresponds to $Q_m \approx 4 \cdot 10^{-4}$.

5. Analysis of High-Order Resonances

By a suitable combination of normal-form and factorization processes the parameters of all resonances $kQ_x + lQ_z = p$ up to eleventh order can be evaluated inside the dynamic aperture of HERA. The basic procedure consists of two steps.[46] First, a four-dimensional truncated Taylor map of eleventh order is extracted from a tracking code by the methods of differential algebra.[9] Second, differential-algebra based normal-form transformations and Lie-algebraic factorizations are performed,[46, 47] which bring the map into a particularly simple form. An overview of differential algebra and of normal-form methods is given in Ref. 6.

An eighth order normal-form transformation for a model of the HERA proton ring still shows considerable deviations from tracking, which indicate that the order 8 is too low. For instance the tune dependence on amplitude is not well reproduced for emittances of about 4 mm mrad (see Fig. 16). However, small resonance denominators prevent a ninth order normal-form transformation from converging in the whole amplitude range of interest. A possible way out is to normalize the map M up to eighth order and subsequently to rewrite the remainder as a Dragt-Finn factorization,[48] or, in other words, to apply first order perturbation theory in the eighth order normal-form coordinate frame. The original map M is then cast into the following form:

$$M = A^{-1} e^{:-2\pi QI + t_3(I) + \ldots + t_8(I):} e^{:f_9(I,\phi):} \ldots e^{:f_{11}(I,\phi):} A + \mathcal{O}(12), \tag{123}$$

where the t_n and f_n are polynomials of degree n in $x_k = \sqrt{2I_k}\cos\phi_k$, and $p_k = -\sqrt{2I_k}\sin\phi_k$. '$A$' denotes the eighth order normal-form transformation. The detuning is deduced from the approximate Hamiltonian

$$H_{approx} = A^{-1}\left[QI - \frac{1}{2\pi}\{t_3(I) + \ldots + t_8(I) + < f_9(I,\phi) + \ldots + f_{11}(I,\phi) >_\phi\}\right]. \tag{124}$$

Tune curves obtained by this method and those from an eighth and an eleventh order normal-form analysis are compared with the tracking data in Fig. 16. Here and in the following,

Figure 16: a) Horizontal tune Q_x as a function of the starting amplitude x_{start} ($\beta_x = 28.5$ m, $z_{start} = 0$), b) vertical tune Q_z as a function of the starting amplitude z_{start} ($\beta_z = 3.8$ m, $x_{start} = 0$). In both diagrams, the maximum amplitude corresponds to an emittance of about 4 mm mrad.

the amplitude values refer to the interaction point, where the horizontal and vertical beta function of the injection optics are $\beta_x \approx 28.5$ m and $\beta_z \approx 3.8$ m, respectively. The horizontal axis in Fig. 16 gives the starting amplitude at this point, the total scale corresponding to an emittance of 4 mm mrad. The initial angles x' and z' are chosen to be zero.

In Fig. 16 the divergence of the eleventh order normal-form analysis and the shortcoming of an eighth order normalization are clearly evident. The combination of a normal-form transformation and a subsequent Dragt-Finn factorization leads to a substantial improvement and reproduces the amplitude-dependent tunes up to the threshold of chaotic motion.

In order to verify the convergence of A^{-1}, the transformation can be directly applied to the tracking data. This is illustrated in Fig. 17 for a trajectory with an initial emittance $\epsilon_x \approx 0$ mm mrad and $\epsilon_z \approx 4$ mm mrad. Shown are the usual phase space projections and those in eighth- and ninth-order normal-form coordinate frames. In the coordinates transformed up to eighth order, the motion in both planes is almost perfectly decoupled and more circular. The finite width of the circle in the horizontal normal-form plane (Fig. 17c) is caused by nonlinear terms of order higher than 8 and can only be removed by increasing the order of the transformation. A ninth order normal-form transformation, however, diverges strongly in the vertical plane (Fig. 17f), when the transformed coordinates become extremely large.

To identify the relevant high-order resonances the amplitude-dependent tunes are depicted in a tune diagram together with the resonance lines. This is done for three different

Figure 17: Tracking data for HERA at an initial emittance $\epsilon_x = 0$ mm mrad and $\epsilon_z \approx 4$ mm mrad; a and b) original horizontal and vertical plane, c and d) horizontal and vertical plane normalized to eighth order, e and f) horizontal and vertical plane normalized to ninth order. Note the different scale in diagram f.

Table 2: Characteristics of high-order resonances in HERA as a function of starting amplitudes x and z for the working point ($Q_x = 31.27$, $Q_z = 32.30$). At the point of observation $x = 11$ mm or $z = 4$ mm corresponds to an emittance of about 4 mm mrad.

x	z	Resonance	$\partial^2 g/\partial I_x^2$	$\partial^2 g/\partial I_x \partial I_z$	$\partial^2 g/\partial I_z^2$	h	Q_I
0.000	2.720	$-3Q_x + 6Q_z = 100$	$0.5 \cdot 10^{-2}$	$-0.4 \cdot 10^{-2}$	$0.26 \cdot 10^{-3}$	$0.2 \cdot 10^{-10}$	$2 \cdot 10^{-6}$
0.000	2.780	$6Q_x - 2Q_z = 123$	$0.5 \cdot 10^{-2}$	$-0.4 \cdot 10^{-2}$	$0.29 \cdot 10^{-3}$	$0.13 \cdot 10^{-14}$	$1.9 \cdot 10^{-8}$
0.000	2.800	$9Q_x + 2Q_z = 346$	$0.5 \cdot 10^{-2}$	$-0.4 \cdot 10^{-2}$	$0.30 \cdot 10^{-3}$	$0.14 \cdot 10^{-23}$	$6.1 \cdot 10^{-13}$
0.000	2.840	$3Q_x + 4Q_z = 223$	$0.55 \cdot 10^{-2}$	$-0.4 \cdot 10^{-2}$	$0.32 \cdot 10^{-3}$	$0.13 \cdot 10^{-9}$	$2.3 \cdot 10^{-6}$
0.000	3.960	$8Q_x + 3Q_z = 347$	$0.8 \cdot 10^{-2}$	$-0.57 \cdot 10^{-2}$	$0.18 \cdot 10^{-1}$	$0.33 \cdot 10^{-20}$	$2.9 \cdot 10^{-11}$
4.290	0.000	$7Q_x - 3Q_z = 122$	$0.33 \cdot 10^{-2}$	$-0.27 \cdot 10^{-2}$	$-0.71 \cdot 10^{-4}$	$0.9 \cdot 10^{-12}$	$5 \cdot 10^{-7}$
6.105	0.000	$-4Q_x + 7Q_z = 101$	$0.31 \cdot 10^{-2}$	$-0.22 \cdot 10^{-2}$	$-0.17 \cdot 10^{-3}$	$0.3 \cdot 10^{-16}$	$2 \cdot 10^{-9}$
7.150	0.000	$11Q_x = 344$	$0.30 \cdot 10^{-2}$	$-0.20 \cdot 10^{-2}$	$-0.19 \cdot 10^{-3}$	$0.11 \cdot 10^{-7}$	$6.3 \cdot 10^{-5}$
5.720	2.080	$7Q_x - 3Q_z = 122$	$0.39 \cdot 10^{-2}$	$-0.24 \cdot 10^{-2}$	$-0.27 \cdot 10^{-3}$	$0.16 \cdot 10^{-6}$	$2.2 \cdot 10^{-4}$
6.490	2.360	$-4Q_x + 7Q_z = 101$	$0.39 \cdot 10^{-2}$	$-0.21 \cdot 10^{-2}$	$-0.36 \cdot 10^{-3}$	$0.31 \cdot 10^{-6}$	$2.24 \cdot 10^{-4}$
8.415	3.060	$11Q_x = 344$	$0.38 \cdot 10^{-2}$	$-0.13 \cdot 10^{-2}$	$-0.62 \cdot 10^{-3}$	$0.77 \cdot 10^{-7}$	$1.9 \cdot 10^{-4}$

working points in Fig. 18. Shown is the change of the tunes when the initial emittance is varied between zero and $\epsilon_x = \epsilon_z = 4$ mm mrad. Also represented in the figure are all resonance lines through order 11. For the three working points, it is possible to identify 11, 6, and 11 resonances of order 7 to 11, which are crossed by the tune, if the starting emittance is changed continuously from 0 to 4 mm mrad along the three lines $\epsilon_x = 0$, $\epsilon_z = 0$, and $\epsilon_x = \epsilon_z$.

The detuning and driving terms $\partial^2 g/\partial I^2$ and h can also be determined by the normal-form analysis. They are evaluated for all resonances crossed in Fig. 18. In Table 2 the results are listed for one of the working points. A compilation of the resonance-parameters for all three working points is given in Refs. 6 and 7.

According to Table 2 an island tune of $2 \cdot 10^{-4}$ and a resonance order $n = 10$ may be considered typical for large amplitudes. The corresponding phase diagram is depicted in Fig. 19. It is evident that tune modulation frequencies above 50 Hz ($Q_m > 10^{-3}$) should be harmless from a sideband-overlap point of view.

Figure 20 shows the island width $\Delta\epsilon_{\rm tot} \equiv 2\Delta I_{\rm tot}$, computed from Eq. (69), as a function of the emittance $\epsilon \equiv \epsilon_x + \epsilon_z$, for the resonances of order 7–11 listed in Table 2 and in Ref. 6. The resonance width is approximately parametrized by

$$\Delta\epsilon_{\rm tot} \approx 2 \cdot 10^{-4} \cdot \epsilon^4 \cdot \ (\text{mm mrad})^{-3}. \tag{125}$$

In Fig. 21 the absolute width of the stochastic layer $w \cdot \Delta I_{\rm tot}$ in mm mrad (Eqs. (69) and (98)) is represented as a function of the modulation frequency for a typical high-order resonance in HERA (tenth resonance in Table 2). The modulation amplitude $q = 10^{-4}$ assumed can for instance be caused by power supply ripple.

Figure 22 is the same as Fig. 21 apart from the larger value of the modulation amplitude $q = 10^{-3}$, which could be due to synchrotron oscillations and a nonzero chromaticity. The design synchrotron frequency of 14 Hz is close to the maximum width of the dotted curve (see Eq. (98)). For this fairly large value of q it becomes important that the relative width w, computed from Eq. (98), has an upper limit of about 2. As mentioned in Section 3.10, this limit is related to the

Figure 18: Diagram of the amplitude-dependent particle tunes for the HERA proton ring and of all resonance lines up to order 11. The tunes are obtained by the combined eighth order normal-form analysis and eleventh order Dragt-Finn factorization. The numbered dots are tunes for special values of the starting emittances: 1) $\epsilon_x = 0$, $\epsilon_z = 0$; 2) $\epsilon_x = 0$, $\epsilon_z = 4$ mm mrad; 3) $\epsilon_x = 4$ mm mrad, $\epsilon_z = 0$; 4) $\epsilon_x = 4$ mm mrad, $\epsilon_z = 4$ mm mrad. The connecting lines correspond to a continuous variation of the initial emittances between these values. The squares, circles and triangles refer to the working points ($Q_x = 31.27$, $Q_z = 32.30$), ($Q_x = 31.27$, $Q_z = 32.295$), and ($Q_x = 31.27$, $Q_z = 32.29$), respectively.

Figure 19: Phase diagram for the island tune $Q_I = 2 \cdot 10^{-4}$ and the resonance order $n = 10$ according to Eq. (96) (solid curves) and contour lines from Eq. (98) for $w = 0.05, 0.1, 0.2$, and 0.3 (dotted curves). This diagram represents a typical high-order resonance at injection energy in HERA.

Figure 20: Island width $\Delta\epsilon_{\rm tot} \equiv 2\Delta I_{\rm tot}$, Eq. (69), as a function of the resonant single-particle emittance $\epsilon \equiv \epsilon_x + \epsilon_z$ in units of mm mrad, for the resonances of order 7–11 listed in Table 2 and in Ref. 6. The closed squares, circles, and triangles refer to the three different working points of Figure 18. The dotted curve represents Eq. (125).

Figure 21: Absolute width of the stochastic layer $w \cdot \Delta I_{\mathrm{tot}}$ in units of mm mrad according to Eqs. (69) and (98) as a function of the modulation frequency Q_m for a typical eleventh order resonance in HERA. This resonance (tenth entry of Table 2) is crossed at an emittance value of $\epsilon = \epsilon_x + \epsilon_z \approx 2.95$ mm mrad and has an island tune $Q_I \approx 2.24 \cdot 10^{-4}$. The modulation amplitude $q = 10^{-4}$ is characteristic of the effect of power supply ripple (see Section 4).

Figure 22: Absolute width of the stochastic layer $w \cdot \Delta I_{\mathrm{tot}}$ in units of mm mrad for the same resonance as in Fig. 21, assuming the larger modulation amplitude $q = 10^{-3}$. A modulation amplitude like this could be caused by synchrotron oscillations and nonzero chromaticity. The dotted curve depicts Eq. (98). The solid curve is obtained by regarding 2 as an upper limit for w, which corresponds to the complete destruction of the resonance island (see also Section 3.10).

complete destruction of the resonance islands. If, for each modulation frequency, the minimum of Eq. (98) and 2 is chosen as the value of w, we get the solid curve in Fig. 22.

6. Diffusion Rates

6.1. Semi-Analytical Approach

In this section we describe a semi-analytical scheme, which allows the evaluation of macroscopic (i.e., measurable) diffusion rates and appears as a promising alternative to, if not substitute for, conventional tracking studies. The basic ingredients of this scheme are

- a set of parameters of isolated, high-order resonances,
- local diffusion rates in the chaotic layer close to a single resonance, and

- a method to combine the local diffusion rates at each resonance into a macroscopic 'global' diffusion rate, which may be compared with experimental measurements.

In Section 5 parameters of high-order resonances were computed for the same detailed model of HERA that is employed in the tracking studies.[6] These parameters may be used to calculate local diffusion rates.

Previously several mechanisms have been proposed to explain the transverse particle transport ('diffusion') observed in circular accelerators and numerically verified for simple Hamiltonian systems, which approximately describe the motion in the vicinity of a resonance. Among these mechanisms are Arnold diffusion,[26, 33] modulational diffusion,[49, 33] resonance streaming,[50, 51] and the strong diffusion across the chaotic layer, which is formed around the separatrix of each resonance.[27, 28]

The local diffusion processes as well as the diffusion due to gas scattering may be described by a Fokker-Planck equation in the action variable.[26, 33, 49, 6] If the motion is Hamiltonian (and also in the case of gas scattering) the Fokker-Planck equation reduces to a diffusion equation with action-dependent coefficients.[33, 6]

We will assume that a diffusion equation also characterizes the macroscopic behavior over regions much larger than the width of the chaotic layer. Such a description was applied successfully to parametrize the beam profile evolution in the Fermilab Tevatron[52] and is routinely employed to analyze the transverse drift rates measured with the HERA collimator system.[54] Most proton storage rings are operated close to the coupling resonance $Q_x - Q_z = p$ (p integer), and in this case it appears sufficient to consider a diffusion equation in the total transverse action $I \equiv I_x + I_z$ of the form

$$\frac{\partial f}{\partial t} = \frac{\partial}{\partial I}\left(D(I)\frac{\partial f}{\partial I}\right). \tag{126}$$

According to Fokker-Planck theory, the diffusion coefficient $D(I)$ in Eq. (126) is related to the squared action change per time interval by the simple formula[6]

$$D(I) = \frac{1}{2}\left\langle \frac{\overline{(\Delta I)^2}}{\Delta t} \right\rangle, \tag{127}$$

and the mean action growth rate $< \overline{\Delta I} > /\Delta t$ satisfies

$$\left\langle \frac{\overline{\Delta I}}{\Delta t} \right\rangle = \frac{d}{dI} D(I). \tag{128}$$

Here, the bar indicates the mean over a particle ensemble, and square brackets denote an average over macroscopic regions of phase space.

A convenient way of approximating the 'global' diffusion coefficient $D(I)$ in Eq. (126) is to average the diffusion inside the chaotic layer over the region between two adjacent resonance islands. This averaging takes into account the fluctuating changes and drifts of the machine parameters which are unavoidable in real accelerators. These parameters' drifts also give rise to the 'sweeping diffusion', which will be discussed in Section 6.4. Alternative ways of

deriving a global diffusion rate from the local diffusion coefficients are conceivable, but the strong amplitude-dependence of the macroscopic diffusion rates is almost completely due to the amplitude-dependence of the local rate and barely depends on the exact manner of calculating the global rate from the local diffusion coefficients.

To provide a self-contained treatment, we start by recalling some values of dynamic aperture, physical aperture, and beam sizes in HERA (compare to Section 2). Here, the values are quoted in terms of action rather than single-particle emittance.

During its commissioning in 1991/92 the dynamic acceptance of the HERA proton ring was measured to be about $I_{dyn.\ acc.} \approx 0.5 - 0.8$ mm mrad, where the uncertainty refers to fluctuations over periods of days or weeks and not to the accuracy of the measurement. Hence the dynamic aperture is not very large when compared with the beam size (two standard deviations) $I_{beam} \approx 0.25$ mm mrad.

In 1992, the physical acceptance, as determined by orthogonal orbit bumps was about twice as large as the dynamic acceptance, $I_{phys.\ acc.} \approx 1.2 - 1.5$ mm mrad. The dynamic acceptance predicted by tracking is even larger, $I \approx 2$ mm mrad, when only the effect of multipole errors is considered. The latter value was determined by the Lyapunov exponent method[33, 55] and refers to the onset of chaotic particle motion in phase space which is supposed to yield a conservative estimate of the dynamic aperture. However, when, in addition to the nonlinear field errors, a realistic tune modulation (of amplitude $q \approx 5 \cdot 10^{-5}$ at a frequency of 50 Hz) is also included in the model, chaotic trajectories are found close to the actual dynamic aperture. It is, therefore, interesting to evaluate diffusion rates in the region between $I \approx 0.5$ mm mrad and $I \approx 4$ mm mrad.

The whole analysis has to be understood as an example. Some of the calculated diffusion rates may be accurate only to within a factor of 10 or 100. This accuracy is adequate for this application since the diffusion rates for distinct processes will differ by up to 35 orders of magnitude, and, furthermore, their amplitude-dependence will be quite different too.

6.2. Chaotic Fraction of Phase Space

In Fig. 23 the absolute width of the chaotic layer $w_{sl}\Delta I_{\rm tot}$ is depicted for each resonance, again as a function of the action I. For about half of the resonances of Fig. 20 the stochastic width is zero. In Fig. 23, zero or very small values are not shown. It is interesting to note that the stochastic width w_{sl} is nonzero only at action values larger than $I_0 \approx 0.8$ mm mrad. This I_0 represents a threshold for tune-modulation induced diffusion, independent of the exact details of the diffusion mechanism, and its value is in remarkable agreement with the dynamic acceptance measured of $I_{dyn.\ acc.} \approx 0.5 - 0.8$ mm mrad.

As a measure of the harmfulness of different tune modulation frequencies for a storage ring such as HERA we introduce a 'sensitivity function' Γ as follows. The product of the total island width and the width of the stochastic layer is summed over all relevant resonances and normalized to the total action range. More specifically, the sensitivity is defined by (compare also Eqs. (69) and (89))

$$\Gamma(Q_m, q) \equiv \sum_{\text{all resonances } i} \Delta I^i_{\rm tot} \cdot w_i(Q_m, q)/I_{tot}$$

Figure 23: Absolute width of stochastic layer $\Delta I_{\rm tot} \cdot w_{sl}$ as a function of the resonant action, for the resonances of Ref. 6. A tune modulation amplitude of $q \sim 5 \cdot 10^{-5}$ at a frequency $Q_m \sim 10^{-3}$ is assumed. The curve represents the parametrization $w_{sl} \cdot \Delta I_{tot} \approx 10^{-4} I^5 (mm\ mrad)^{-4}$.

$$= \sum_{\text{all resonances } i} \left(\frac{Q_m}{Q_{I,i}}\right)^2 \frac{\sinh\left(\frac{\pi Q_m}{2Q_{I,i}}\right)}{\sinh\left(\frac{\pi Q_m}{Q_{I,i}}\right)} \frac{\sqrt{l_i^2 + k_i^2}(l_i + k_i) 4\pi q}{\left| l_i^2 \frac{\partial^2 g_i}{\partial I_z^2} + 2k_i l_i \frac{\partial^2 g_i}{\partial I_x \partial I_z} + k_i^2 \frac{\partial^2 g_i}{\partial I_x^2} \right|} \frac{1}{I_{tot}}, \qquad (129)$$

where the subscript 'i' denotes the individual resonances. The function so defined measures the fraction of phase space that becomes chaotic due to the tune modulation. It depends on the modulation frequency Q_m and on the modulation amplitude q.

Figure 24 shows the chaotic fraction of phase space for a modulation frequency $q = 10^{-4}$, where the sum in Eq. (129) was extended over all resonances through eleventh order identified between $I = 0$ and $I \approx 4$ mm mrad.[6, 7] The sensitivity to tune modulation is highest for modulation frequencies between 5 and 50 Hz. Chaotic trajectories may cover about 10% of the phase space in the presence of a 50-Hz power supply ripple. For frequencies above 100 Hz the effect of the tune modulation is negligible.

6.3. Modulational Diffusion

For small modulation frequency Q_m and large amplitude q, tune modulation causes a strongly chaotic band of overlapping sideband resonances. Particles inside such a modulational layer are driven *along* the resonance contour and may reach large amplitudes. As we shall see, the calculation of the local diffusion rate for this '*modulational diffusion*' involves an average over the modulational layer, since after some time a particle has sampled all action values inside that layer. A subsequent averaging of the local rate over larger regions of the phase space gives the macroscopic diffusion coefficient. The resulting diffusion rate exceeds that for ordinary 'thin-layer' Arnold diffusion,[33, 49] which is discussed in Ref. 7, by many orders of magnitude.

Figure 24: Chaotic fraction of phase space Γ (see Eq. (129)) as a function of the modulation frequency for a constant modulation amplitude $q = 10^{-4}$.

Two conditions have to be fulfilled in order to generate modulational diffusion. First, several strong sidebands are required. The number of large sidebands is roughly given by $(2\ |k+l|\ q/Q_m + 1)$. Tune modulation is, for instance, caused by current ripple in the main superconducting circuit (due to power supply ripple).[6] In that case $q \leq 5 \cdot 10^{-5}$, $|k+l| \approx 3$–11, and $Q_m \sim 10^{-3}$, so that at the most the two first order sideband resonances may become sizable.

Usually, synchrotron motion is included in the tracking simulation and here leads to a reduction of the dynamic acceptance for off-energy particles. The onset of strong chaos, determined from tracking data by the Lyapunov exponent method (Section 2), is reduced to $I_{dyn.\ acc.} \approx 1.7$ mm mrad for particles performing synchrotron oscillations of amplitude $\Delta p/p \approx 5 \cdot 10^{-4}$ (which corresponds to about 2 standard deviations of the momentum distribution) and chromaticity $\xi_{x,z} \equiv \Delta Q_{x,z}/\frac{\Delta p}{p} \approx 1$. For comparison, the dynamic acceptance for particles of constant energy $\Delta p/p = 0$ is found at $I_{dyn.\ acc.} \approx 2.1$ mm mrad. As typically computed in the simulation, 10,000 turns cover only four synchrotron oscillation periods, such that the total effect of modulational diffusion cannot be seen in the tracking.

Clearly, a normal-form analysis in the full six-dimensional phase space would offer additional insight. Extraction of an eleventh order Taylor map in the four-dimensional transverse

Figure 25: Ratio of resonance width and separation of zeroth and first sideband resonances (see Eq. (130)) as a function of the action, for the resonance parameters listed in Ref.6, 7. A tune modulation of $q \approx 5 \cdot 10^{-5}$ and $Q_m \approx 10^{-3}$ has been assumed which is characteristic for power supply ripple. For ratios larger than 1, resonance overlap is expected.

phase space, however, requires the maximum storage (about 48 Mbytes) available on the IBM 9000-720 at DESY. We will, therefore, approximate the effect of synchrotron motion and nonzero chromaticity by the accompanying tune modulation in the transverse phase space. A typical modulation amplitude is $q \approx 2 \cdot 10^{-4}$ (assuming a relative energy deviation $\delta \approx 2 \cdot 10^{-4}$ and chromaticity $\xi \equiv \Delta Q / \frac{\Delta p}{p} \approx 1$). The synchrotron frequency corresponds to $Q_m \approx 4 \cdot 10^{-4}$. The total number of strong sidebands is then of the order 4–12.

The second condition for modulational diffusion, besides the large size of the sidebands, is that the sidebands do have to overlap. The overlap condition for power supply ripple can be written (see Section 3)

$$\frac{\Delta \bar{I}_{x,\mathrm{tot}}}{\delta \bar{I}_x} \equiv \left[\left| J_0 \left(\frac{(k+l)q}{Q_m} \right) \right|^{\frac{1}{2}} + \left| J_{\pm 1} \left(\frac{(k+l)q}{Q_m} \right) \right|^{\frac{1}{2}} \right] \frac{Q_I}{Q_m} 2 \geq 1, \tag{130}$$

which translates into

$$Q_I \geq 3.4 \cdot 10^{-4}. \tag{131}$$

Figure 25 shows the expression on the left hand side of Eq. (130) plotted as a function of the resonant action value, for the case of power supply ripple. The overlap condition is fulfilled only for the outermost resonances, at which strong chaos is observed (in the tracking) even in the absence of tune modulation. There are several resonances at action values between $I \approx 1$ mm mrad and $I \approx 4$ mm mrad for which the sideband overlap is almost fulfilled (but even for $q = 10^{-4}$ it is not).

Figure 26: The left hand side of the inequality, Eq. (132), as a function of the action, for the resonance parameters listed in the appendix (dots). A tune modulation $q \approx 2 \cdot 10^{-4}$ and $Q_m \approx 4 \cdot 10^{-4}$ has been assumed which may be caused by synchrotron oscillation and nonzero chromaticity. For ratios larger than 1, resonance overlap is expected.

For modulation due to synchrotron oscillation and chromaticity more sideband resonances (up to about twelve) are large, and the overlap condition for these sidebands can approximately be written as (see Section 3)

$$\frac{\Delta \bar{I}_{x,tot}}{d\bar{I}_x} = \frac{4}{\pi^{\frac{1}{4}}} \frac{Q_I}{|k+l|^{\frac{1}{4}}\ q^{\frac{1}{4}} Q_m^{\frac{3}{4}}} \geq 1, \tag{132}$$

where the Bessel functions of Eq. (20) have been replaced by their rms-values for large arguments. The inequality in Eq. (132) corresponds to

$$Q_I \geq 1.5 - 2 \cdot 10^{-4}. \tag{133}$$

Hence in the case of synchrotron oscillations the overlap occurs for a smaller value of the island tune Q_I. In Fig. 26 the expression on the left hand side of Eq. (132) is depicted as a function of the resonant action value for tune modulation caused by synchrotron oscillations. The overlap condition is fulfilled for about half of the resonances.

The resulting diffusion rate can be calculated following Refs. 33 and 49. As a starting point, for $k \neq 0$ we choose the Hamiltonian

$$\begin{aligned} H(\bar{\Delta}_x, \bar{\phi}_x, \bar{I}_z, \bar{\phi}_z, \theta) &= \frac{1}{2}\frac{\partial^2 g}{\partial \bar{I}_x^2}\bar{\Delta}_x^2 + h\cos\bar{\phi}_x + q\bar{\Delta}_x(k+l)\cos Q_m\theta \\ &+\kappa I_{x,r}^{\frac{1}{2}} I_{z,0}^{\frac{1}{2}} \cos\left(\frac{1}{k}\bar{\phi}_x - \frac{l}{k}\bar{\phi}_z + \frac{p}{k}\theta - m\theta - \bar{\phi}_z + \chi_0\right) + \bar{I}_z Q_{z0}, \end{aligned} \tag{134}$$

where $\bar{\Delta}_x \equiv \bar{I}_x - \bar{I}_{x,r}$ is the deviation from the resonant value and χ_0 an initial phase.

To estimate the rate of diffusion, we have supposed in Eq. (134) that the driving term $h_{coupl}(I_x, I_z)$ of the main coupling resonance $Q_x - Q_z = m$ ($m = -1$ for HERA),

$$h_{coupl}(I_x, I_z) = \kappa I_x^{\frac{1}{2}} I_z^{\frac{1}{2}} \cos(\phi_x - \phi_z - m\theta + \chi_0), \tag{135}$$

gives rise to the pump diffusion along $\bar{I}_z$. The parameter κ corresponds to the minimum distance of the measured tunes as a function of nominal tunes[22] and is of the order $\kappa \approx 0.005$.

The stochastic modulational layer extends over all overlapping sideband resonances, which can lead to a significant diffusion rate. In order to calculate it, the Hamiltonian may be decomposed into two parts:

$$\begin{aligned} H_{across}(\bar{\Delta}_x, \bar{\phi}_x, \theta) &= \frac{1}{2}\frac{\partial^2 g}{\partial \bar{I}_x^2}\bar{\Delta}_x^2 + h\cos\left(\bar{\phi}_x + \frac{q\ (k+l)}{Q_m}\sin Q_m\theta\right) \\ H_{along}(\bar{I}_z, \bar{\phi}_z, \theta) &= \bar{I}_z Q_{z0} + \kappa I_{x,r}^{\frac{1}{2}} I_{z,0}^{\frac{1}{2}} \cos\left(\frac{1}{k}\bar{\phi}_x(\theta) - \frac{l}{k}\bar{\phi}_z + \frac{p}{k}\theta - \right. \\ &\quad \left. -m\theta - \bar{\phi}_z + \chi_0\right), \end{aligned} \tag{136}$$

where the change of $\bar{\phi}_x$ due to H_{across} drives the motion along the stochastic layer via H_{along}. Canonical perturbation theory can be used to derive $\bar{\phi}_x$.[33] In zeroth order

$$H_{across,0} = \frac{1}{2}\frac{\partial^2 g}{\partial \bar{I}_x^2}\bar{\Delta}_x^2, \tag{137}$$

which gives

$$\begin{aligned} \bar{\Delta}_{x,0} &= const., \\ \bar{\phi}_{x,0} &= (\partial^2 g/\partial \bar{I}_x^2)\ \bar{\Delta}_{x,0}\theta. \end{aligned} \tag{138}$$

To first order in h the angle $\bar{\phi}_x$ is

$$\bar{\phi}_x = \frac{\partial^2 g}{\partial \bar{I}_x^2}\bar{\Delta}_{x,0}\theta + h\sum_n \frac{J_n\left(\frac{q(k+l)}{Q_m}\right)}{\left(nQ_m + \bar{\Delta}_{x,0}\frac{\partial^2 g}{\partial \bar{I}_x^2}\right)^2}\sin\left(\frac{\partial^2 g}{\partial \bar{I}_x^2}\bar{\Delta}_{x,0}\theta + nQ_m\theta\right). \tag{139}$$

The argument of the cosine in H_{along} may now be written

$$\begin{aligned} \phi(\theta) &\equiv \frac{1}{k}\bar{\phi}_x(\theta) - \frac{l}{k}\bar{\phi}_z - \bar{\phi}_z + \frac{p}{k}\theta - m\theta + \chi_0 \\ &\approx \frac{1}{k}\frac{\partial^2 g}{\partial \bar{I}_x^2}\bar{\Delta}_{x,0}\theta - (Q_{x0} - Q_{z0} - m)\theta + \chi_0 + \\ &\quad + \frac{h}{k}RJ_\lambda(\lambda)\frac{1}{\left(\lambda Q_m + \bar{\Delta}_{x,0}\frac{\partial^2 g}{\partial \bar{I}_x^2}\right)^2}\sin\left(\frac{\partial^2 g}{\partial \bar{I}_x^2}\bar{\Delta}_{x,0}\theta + \lambda Q_m\theta\right). \end{aligned} \tag{140}$$

Here, $\lambda \equiv |k+l|\ q/Q_m$, and we have replaced $J_n\left(\frac{q\ (k+l)}{Q_m}\right)$ of Eq. (139) by the typical value $J_\lambda(\lambda) \approx 0.5$. R denotes an 'effective' number of resonances (we will assume $R \approx (2\lambda+1)$, that is, $R \approx 3$ in the case of power supply ripple, and $R \approx 4$–12 for synchrotron oscillations). The change of H_{along} during the time $T \equiv \Theta/(2\pi f_{rev})$ is about

$$\begin{aligned}
\Delta H_{along} &= \int_{-\Theta}^{\Theta} \frac{\partial}{\partial\theta} H_{along}\, d\theta \\
&= \kappa I_{x,r}^{\frac{1}{2}} I_{z,0}^{\frac{1}{2}} \left[\cos\phi(\Theta) - \cos\phi(-\Theta) - \left(1+\frac{l}{k}\right) Q_{z0} \int_{-\Theta}^{\Theta} \sin\phi\, d\theta\right] \\
&\approx -\kappa I_{x,r}^{\frac{1}{2}} I_{z,0}^{\frac{1}{2}} \left(1+\frac{l}{k}\right) Q_{z0} \int_{-\Theta}^{\Theta} \sin\phi\, d\theta, \qquad (141)
\end{aligned}$$

and the integrand in Eq. (141) is

$$\begin{aligned}
\sin\phi(\theta) &= \sum_j A_j(\bar{\Delta}_{x,0}) \sin\left[\left(\frac{1}{k}\frac{\partial^2 g}{\partial \bar{I}_x^2}\bar{\Delta}_{x,0} - (Q_{x0} - Q_{z0} - m) + \right.\right. \\
&\quad \left.\left. + j\frac{\partial^2 g}{\partial \bar{I}_x^2}\bar{\Delta}_{x,0} + j\lambda Q_m\right)\theta + \chi_0\right], \qquad (142)
\end{aligned}$$

where

$$A_j(\bar{\Delta}_{x,0}) \equiv J_j\left[\frac{h}{k}\frac{R}{\left(\lambda Q_m + \bar{\Delta}_{x,0}\frac{\partial^2 g}{\partial \bar{I}_x^2}\right)^2} J_\lambda(\lambda)\right]. \qquad (143)$$

The diffusion rate in I_z is now obtained by averaging over the width of the modulational layer $2\bar{\Delta}_{x,0,\max} = 2\lambda Q_m / |\frac{\partial g}{\partial \bar{I}_x^2}|$:[49, 33]

$$\begin{aligned}
D_z &= \lim_{\Theta\to\infty} \left\langle \frac{2\pi f_{rev} (\Delta H_{along})^2}{2Q_{z0}^2 (2\Theta)} \right\rangle_{\bar{\Delta}_{x,0},\ \chi_0} \\
&= \lim_{\Theta\to\infty} \left\langle \frac{2\pi f_{rev}}{4\Theta} \frac{\kappa^2 I_{x,r} I_{z,0}}{2\frac{\lambda Q_m}{|\frac{\partial^2 g}{\partial \bar{I}_x^2}|}} \int_{-\lambda Q_m/|\frac{\partial^2 g}{\partial \bar{I}_x^2}|}^{\lambda Q_m/|\frac{\partial^2 g}{\partial \bar{I}_x^2}|} d\bar{\Delta}_{x,0}\ \left(1+\frac{l}{k}\right)^2 \cdot \right. \\
&\quad \left. \cdot \int_{-\Theta}^{+\Theta} d\theta'' \sin\phi(\theta'') \int_{-\Theta}^{+\Theta} d\theta' \sin\phi(\theta') \right\rangle_{\chi_0}, \qquad (144)
\end{aligned}$$

where the integration over θ'' yields a delta function

$$\begin{aligned}
\int_{-\infty}^{\infty} d\theta'' \sin\phi(\theta'') &= \sum_j A_j(\bar{\Delta}_{x,0}) \sin\chi_0 \frac{2\pi}{\left(\frac{1}{k}+j\right)\frac{\partial^2 g}{\partial \bar{I}_x^2}} \cdot \\
&\quad \cdot\delta\left(\bar{\Delta}_x - \frac{(Q_{x0} - Q_{z0} - m) - j\lambda Q_m}{\left(\frac{1}{k}+j\right)\frac{\partial^2 g}{\partial \bar{I}_x^2}}\right). \qquad (145)
\end{aligned}$$

The integration over $\bar{\Delta}_{x,0}$ in Eq. (144) is readily performed:

$$D_z = \frac{\pi^2 f_{rev}\kappa^2 I_{x,r} I_{z,0}\left(1+\frac{l}{k}\right)^2}{\lambda Q_m} < \sin^2\chi_0 >_{\chi_0} \cdot \\ \cdot \sum_{j=\tilde{l}}^{\infty} \frac{1}{\left(\frac{1}{k}+j\right)} A_j^2 \left(\frac{Q_{x0}-Q_{z0}-m-j\lambda Q_m}{\left(\frac{1}{k}+j\right)\frac{\partial^2 g}{\partial I_x^2}}\right) \frac{1}{2\Theta}\int_{-\Theta}^{\Theta} d\theta', \tag{146}$$

and after averaging over χ_0 we obtain the approximate result

$$D_z \approx \frac{\pi^2 f_{rev}}{2} \frac{\kappa^2 I_{x,r} I_{z,0}\left(1+\frac{l}{k}\right)^2}{\lambda Q_m\left(\frac{1}{k}+\tilde{l}\right)} J_{\tilde{l}}^2\left[\frac{h}{k^3}\frac{RJ_\lambda(\lambda)(1+\tilde{l}k)^2}{(Q_{x0}-Q_{z0}-m+\frac{\lambda}{k}Q_m)^2}\right], \tag{147}$$

where $j=\tilde{l}$, with

$$\tilde{l} = \text{integer part}\left\{\frac{1}{2}\left[-\frac{1}{k}+\frac{Q_{x0}-Q_{z0}-m}{\lambda Q_m}\right]\right\}, \tag{148}$$

is the dominant term in the sum over j of Eq. (146). The total transverse diffusion rate is given by

$$D_{mod.\ local} = \left(\frac{l}{k}\frac{\frac{\partial^2 g}{\partial I_z^2}+\frac{\partial^2 g}{\partial I_z \partial I_x}}{\frac{\partial^2 g}{\partial I_x^2}+\frac{\partial^2 g}{\partial I_x \partial I_z}}-1\right)^2 D_z. \tag{149}$$

For $k=0$, $l\neq 0$ the diffusion rate is

$$D_{mod.\ local} = D_x \approx \frac{\pi^2 f_{rev}}{2}\frac{\kappa^2 I_{x,r} I_{z,0}}{\lambda Q_m\left(\frac{1}{l}+\tilde{l}\right)} J_{\tilde{l}}^2\left[\frac{h}{l^3}\frac{RJ_1(1)(1+\tilde{l}l)^2}{(Q_{x0}-Q_{z0}-m+\frac{\lambda}{l}Q_m)^2}\right], \tag{150}$$

where

$$\tilde{l} = \text{integer part}\left\{\frac{1}{2}\left[-\frac{1}{l}+\frac{Q_{x0}-Q_{z0}-m}{\lambda Q_m}\right]\right\}. \tag{151}$$

The macroscopic diffusion coefficient to be compared with observations differs from the local coefficient $D_{mod.\ local}$ of Eq. (149) or (150), since the storage ring parameters (and hence the parameters in the Hamiltonian) drift slowly, as is evident from drifts of the tunes, of the beam orbit etc. over periods of minutes or hours. It may be suspected that these changes of parameters are mainly due to temperature effects in the magnets and the power supplies.

The parameter drifts cause a motion of the resonance islands across the phase space. If we denote the mean change of the machine tune per unit time by $\dot{Q}$, the rate at which the position of the island changes is about

$$\left(\frac{\Delta I}{\Delta t}\right)_{island-drift} \approx \frac{\dot{Q}}{\partial^2 g/\partial I^2}. \tag{152}$$

Figure 27: Diffusion coefficient $D_{mod.}^{p.s.r.}(I)$ due to modulational diffusion caused by power supply ripple (assuming there are three overlapping sidebands), as a function of the action, for the resonances listed in the appendix (dots). A separation of tunes $(Q_{x0} - Q_{z0} - m) \approx 0.005$ is assumed. The curve represents the parametrization $D_{mod.}^{p.s.r.}(I) \approx 5 \cdot 10^{-11} I^{25}$ (mm mrad)$^{-23}$ s^{-1}. Note the large value $D_{mod.}^{p.s.r.}(I) \approx 10^6$ (mm rad)^2 s^{-1} for the single resonance at $I \approx 1.2$ mm mrad which is not covered by this parametrization.

Typically the tune changes at least by 10^{-4} during 1 hour. The corresponding action change is roughly 0.1 mm mrad (see Fig. 16). Hence the islands alter their positions at a minimum rate

$$\left(\frac{\Delta I}{\Delta t}\right)_{island-drift} \approx 3 \cdot 10^{-5} \text{ mm mrad s}^{-1}. \tag{153}$$

In a first, rough approximation, the motion of resonance islands in phase space leads to an averaging of the diffusion coefficient, describing the motion in the chaotic domain of overlapping sideband resonances over the region between two adjacent fundamental resonances. The 'macroscopic' diffusion coefficient at the ith resonance is then

$$\begin{aligned} D_{mod.}(I_i) &\approx \frac{2\sqrt{k_i^2 + l_i^2} R \; \delta \bar{I}_x}{I_{i+1} - I_{i-1}} D_{mod.\ local,i}(I) \\ &\approx \frac{2 \sqrt{k_i^2 + l_i^2} \; R_i \; Q_m D_{mod.\ local,i}}{\left| k^2 \frac{\partial^2 g(I_{x,r}, I_{z,r})}{\partial I_x^2} + 2kl \frac{\partial^2 g(I_{x,r}, I_{z,r})}{\partial I_x I_z} + l^2 \frac{\partial^2 g(I_{x,r}, I_{z,r})}{\partial I_z^2} \right| \; (I_{i+1} - I_{i-1})}, \end{aligned} \tag{154}$$

where we have divided by the sum of the half-distances and the two adjacent resonances $(I_{i+1} - I_{i-1})/2$, and R is the approximate number of relevant sidebands.

The diffusion rate of Eq. (154) evaluated for power supply ripple is shown in Fig. 27 for $(Q_{x0} - Q_{z0} - m) \approx 0.005$ and linear coupling strength $\kappa \approx 0.005$. Note that an overlap of only three sideband islands has been assumed for each resonance, and that even this modest overlap may not occur, as indicated by Fig. 25.

Figure 28: Diffusion coefficient $D_{mod.}^{sync.}(I)$ due to modulational diffusion induced by synchrotron oscillations and chromaticity, as a function of the action. Represented are values for those resonances (17 out of 28) in the appendix, for which both the first-order sidebands are large and the overlap condition is fulfilled (dots). A separation of tunes $(Q_{x0} - Q_{z0} - m) \approx 0.005$ and modulation parameters $q \sim 2 \cdot 10^{-4}$ and $Q_m \sim 4 \cdot 10^{-4}$ characteristic for synchrotron oscillations are assumed. The curve represents the parametrization $D_{mod.}^{sync.}(I) \approx 5 \cdot 10^{-11} I^{25}$ (mm mrad)$^{-23}$ s^{-1}, which is the same as for the case of power supply ripple. Note also here the large value of $D_{mod}^{sync.}(I)$ for the resonance at $I \approx 1.2$ mm mrad which is not covered by this parametrization.

On the other hand, synchrotron oscillations plus nonzero chromaticity generate a larger number of strong sidebands, a significant fraction of which are actually overlapping. The diffusion coefficient $D_{mod.}(I)$ of Eq. (154) for this case is depicted in Fig. 28. Here, only resonances for which $|k + l|\ q/Q_m \geq 1$ are represented (i.e., at least the first order sideband resonance is sizable) and for which, furthermore, the overlap criterion of Eq. (132) is fulfilled.

The coefficient $D_{mod}(I)$ for modulational diffusion is roughly parametrized by the function $D_{mod.}(I) \approx 10^{-7} I^{25}$ (mm mrad)$^{-23}$ s^{-1} both for tune modulation due to power supply ripple and due to synchrotron oscillations (compare Figs. 27 and 28).

6.4. Sweeping Diffusion

If the machine parameters, like orbit and tune, were kept constant for all times, the strong diffusion of particles *across* each chaotic layer would have no measurable effect. In real accelerators, however, these parameters are continually subject to change. As a consequence of which, the resonance islands are incessantly altering their position in the four-dimensional phase space, and individual particles will follow a succession of regular and chaotic trajectory segments. A measurable diffusion rate is the result, which we call '*sweeping diffusion*'. Its size will be estimated via a macroscopic average in phase space.

Figure 29: Local diffusion coefficient $D_{local}(I)$ inside the chaotic layer as a function of the action, for the resonances of order 7–11 listed in the appendix (dots). A modulation amplitude $q = 5 \cdot 10^{-5}$ is assumed. The curve represents the parametrization $D_{local}(I) \approx 5 \cdot 10^{-8} I^{15}$ (mm mrad)$^{-13}$ s^{-1}.

Figure 29 shows the local action growth rate from Eq. (72) for the 28 resonances listed in the appendix. A possible parametrization is

$$D_{local}(I) = \frac{< (\Delta(I_x + I_z))^2 >}{2\ \Delta t} \approx 5 \cdot 10^{-8} I^{15}\ (\text{mm mrad})^{-13} \text{s}^{-1}. \tag{155}$$

Similar to the treatment of modulational diffusion, but essential in this case, the motion of resonance islands in phase space, caused by power supply drifts and other perturbations, may be taken into account by averaging the diffusion inside the chaotic layer over the region between two adjacent resonances.[6] This averaging is further motivated by the following consideration. Since their motion is very slow, protons in the chaotic layer cannot follow the drifting resonance islands and become regular, while other, previously regular particles will become chaotic. The average over some regions of the phase space is then equivalent to an average over certain parts of the particle distribution.

The resulting coefficient $D_{sd}(I)$ of this '*sweeping diffusion*' is then

$$\begin{aligned} D_{sd}(I_i) &= \frac{1}{2} \left\langle \frac{\overline{(\Delta(I_x + I_z))^2}}{\Delta t} \right\rangle_i \approx \Delta I^i_{\text{tot}} \cdot w_i \cdot \left(\frac{\overline{(\Delta(I_x + I_z))^2}}{\Delta t} \right)_i \frac{1}{I_{i+1} - I_{i-1}} \\ &= \left(\frac{Q_m}{Q_{I,i}} \right)^2 \frac{\sinh\left(\frac{\pi Q_m}{2Q_{I,i}}\right)}{\sinh\left(\frac{\pi Q_m}{Q_{I,i}}\right)} \frac{128\pi\sqrt{k_i^2 + l_i^2}(k_i + l_i)^2 f_{rev} h_i^2(I_{x,r,i}, I_{z,r,i})}{|l_i^2 \frac{\partial^2 g_i}{\partial I_z^2} + 2k_i l_i \frac{\partial^2 g_i}{\partial I_x \partial I_z} + k_i^2 \frac{\partial^2 g_i}{\partial I_x^2}|(I_{i+1} - I_{i-1})}. \end{aligned} \tag{156}$$

Note that the diffusion coefficient $D_{sd}(I)$ in Eq. (156) is independent of the modulation amplitude q, which reflects the fact that the fraction of phase space covered with chaotic trajectories increases linearly with the modulation amplitude q, whereas the diffusion rate in this zone decreases as $1/q$ (see Eqs. (98) and (72)).

Figure 30: Diffusion coefficient $D_{sd}(I)$ due to 'sweeping diffusion' as a function of the action in units of mm mrad for the resonances of order 7–11 listed in the appendix (dots). A modulation frequency $Q_m = 10^{-3}$ is assumed. Below $I_0 \approx 0.7$ mm mrad the phase space is covered by regular trajectories, while at 4 mm mrad the diffusion coefficient $D_{sd}(I)$ adopts values on the order of 1 (mm mrad)$^2/s$. In the intermediate emittance range $D_{sd}(I)$ can be roughly parametrized by the function $D_{sd}(I) \approx 4 \cdot 10^{-10} I^{15}$ (mm mrad)$^{-13}$s^{-1}.

The action-dependent diffusion coefficient $D_{sd}(I)$, defined in Eq. (156), is shown in Fig. 30 assuming a modulation frequency of 50 Hz ($Q_m = 10^{-3}$). A possible parametrization is $D_{sd} \approx 4 \cdot 10^{-10} I^{15}$ (mm mrad)$^{-13}$ s^{-1}.
According to Eq. (128) the action growth rate is given by

$$\left\langle \frac{\overline{\Delta I}}{\Delta t} \right\rangle = \frac{d}{dI} D_{sd}(I) \approx 6 \cdot 10^{-9} I^{14} \text{ (mm mrad)}^{-13} \text{ s}^{-1}. \tag{157}$$

The action growth rate of Eq. (157) is small compared with the island drift rate, if

$$I \leq 1.8 \text{ mm mrad}, \tag{158}$$

where use has been made of Eqs. (72), (128), and (153). For this amplitude regime (which is larger than the physical aperture of HERA) the averaging over the regular and chaotic regions of phase space seems justified.

6.5. Comparison of Different Processes

The dynamic aperture observed in HERA agrees well with the smallest value of action at which a chaotic layer of nonzero width is caused by a realistic tune modulation. The diffusion coefficients for modulational diffusion, for sweeping diffusion, resonance streaming,[7] Arnold diffusion,[7] and gas scattering ($p_{H_2} = 2 \cdot 10^{-9}$ mbar[6]) are depicted for comparison in Fig. 31. It seems very

Figure 31: Comparison of diffusion coefficients computed for different types of nonlinear transport mechanisms and for gas scattering as functions of action.

unlikely that Arnold diffusion or resonance streaming is the source of the dynamic aperture, since the corresponding diffusion rates are too small by many orders of magnitude.

The largest diffusion rates are those for modulational diffusion and sweeping diffusion. The diffusion coefficients for both processes exhibit a steep increase as a function of action, and could thus give rise to something resembling a 'dynamic aperture'. They are calculated as averages of the local diffusion coefficients over regular and chaotic phase space regions between two adjacent resonances. This average is a first attempt to take into account all other types of perturbations (besides tune modulation) which will move the resonance islands around in phase space. On the other hand, the diffusion coefficients and growth rates calculated for resonance streaming and Arnold diffusion may be considered as upper limits, since they refer to the region inside the chaotic layer and would be reduced (by a factor of 100–1000) if averaged over the phase space (see also Fig. 23).

Figure 32 shows the mean action growth rate $< \overline{\Delta I}/\Delta t >$ derived from $D(I)$ according to Eq. (128) together with the growth rate due to intra-beam scattering for the design number of 10^{11} protons per bunch.[56, 57, 6]

In the amplitude regime of interest (between $I \approx 1$ mm mrad and $I \approx 2$ mm mrad) the growth rate for modulational diffusion is larger than that for sweeping diffusion by up to several orders of magnitude. Hence, modulational diffusion is the most likely cause of the dynamic aperture measured.

Figure 32: Comparison of mean action growth rates computed for different types of nonlinear transport mechanisms, for gas scattering, and for intra-beam scattering as functions of action.

7. Conclusions

The observed dynamic aperture of about $\epsilon \approx 1.2$ mm mrad in the HERA proton ring at 40 GeV is in good agreement with the results of computer simulations and analytical calculations which consider the combined effects of the measured nonlinear field errors of all superconducting magnets and a modest tune modulation. Techniques to facilitate the simulation studies have been proposed and investigated in detail. The use of Lyapunov exponents in the postprocessing analysis of tracking data is a promising method, which has routinely been applied in the simulation studies. The effect of tune modulation on a single resonance island in a nonlinear Hamiltonian system has been described in detail. It was shown how a suitable combination of normal-form and factorization processes permits the extraction of parameters for resonances including eleventh order inside the whole dynamic aperture of a complex storage ring such as HERA. A semi-analytical method for calculating transverse diffusion rates from these resonance parameters was used to derive and evaluate expressions for macroscopic diffusion coefficients, as caused by resonance streaming and modulational diffusion. Modulational diffusion due to synchrotron oscillations and nonzero chromaticity has been identified as the most probable source of the dynamic aperture measured. Further dedicated measurements are required to get a better experimental confirmation of the calculated diffusion rates.

Acknowledgements

I am very grateful to F. Willeke and P. Schmüser for guidance and continued encouragement. It is a pleasure to thank Y. Yan, A. Chao, and M. Syphers for the opportunity to visit the Superconducting Super Collider and for suggesting this lecture note. I thank É. Forest and M. Berz for providing the Lie-algebraic and differential-algebra program packages, respectively. Furthermore, I am indebted to F. Schmidt for his co-operation in creating and installing the differential-algebra version of SIXTRACK. The help of the DESY magnet measuring group, which made available the multipole data of the HERA magnets, is also appreciated. Many colleagues at DESY, SLAC, CERN, and SSC deserve my thanks for help and co-operation. Finally, I thank L. Gennari and S. MacBride for their help with this manuscript and its figures.

References

[1] H. Brück, R. Meinke, F. Müller, and P. Schmüser, "Field distortions from Persistent Currents in the Superconducting HERA Magnets," DESY 89–041 (1989).

[2] C. Daum et al., "The Superconducting Quadrupole and Sextupole Correction Coils for the HERA Proton Ring," DESY HERA 89–09 (1989).

[3] R. Brinkmann and F. Willeke, "Persistent Current Field Errors and Dynamic Aperture of the HERA Proton Ring." DESY HERA 88–08 (1988).

[4] F. Willeke and F. Zimmermann, "The Impact of Persistent Current Field Errors on the Stability of the Proton Beam in the HERA Proton Ring," *Proceedings of the IEEE Particle Accelerator Conference*, San Francisco (1991), p. 2483.

[5] S. Herb, O. Meincke, P. Schmüser, F. Willeke, and F. Zimmermann, "Experience with Persistent Current Field Errors in the HERA Proton Ring," *Proceedings of the 1992 High Energy Accelerator Conference*, Hamburg (1992).

[6] F. Zimmermann, "Emittance Growth and Proton Beam Lifetime in HERA," Ph.D. thesis, DESY 93–59 (1993).

[7] F. Zimmermann, "Transverse Proton Diffusion," submitted to *Part. Acc.* (1994).

[8] S.K. Kaufmann, D.M. Ritson, and Y. Yan, "Implementation of one-turn maps in SSCTRK using Zlib," SSCL–321 (1990);
Y. Yan and C. Yan, "Zlib—A Numerical Library for Differential Algebra," SSCL–300 (1990);
Y. Yan, T. Sen, A. Chao, G. Bourianoff, A. Dragt, and É. Forest, "Comments on round-off errors and on one-turn Taylor maps," SSCL–301 (1990).

[9] M. Berz, "Differential-algebraic description of beam dynamics to very high orders," *Part. Acc.* **24**, 109 (1989).

[10] R. Kleiss, F. Schmidt, Y. Yan, and F. Zimmermann, "On the Feasibility of Tracking with Differential-Algebra Maps in Long-Term Stability Studies for Large Hadron Colliders," DESY HERA 92–01, CERN SL/ 92–02 (AP), and SSCL–564 (1992).

[11] J. Irwin, "A Multi-kick Factorization Algorithm for Nonlinear Maps," SSC–228 (1989).

[12] R. Kleiss, F. Schmidt, F. Zimmermann, "The Use of Truncated Taylor Maps in Dynamic Aperture Studies", DESY HERA 92-21, CERN SL/92-47 (AP), published in *Part. Acc.* **41**, 117–132 (1993).

[13] M. Hénon and C. Heiles, "The Applicability of the Third Integral of Motion: Some Numerical Experiments," *Astron. J.* **69**, 73 (1964).

[14] V.I. Oseledec, "A multiplicative ergodic theorem. Ljapunov characteristic numbers for dynamical systems," *Trans. Moscow Math. Soc.* **19**, 197 (1968).

[15] D.P. Barber, G. Ripken, and F. Schmidt, "A non-linear canonical formalism for the coupled synchro-betatron motion of protons with arbitrary energy," DESY 87–036 (1987).

[16] P. Schmüser, "Basic Course on Accelerator Optics," CERN Accelerator School, Aarhus 1986, CERN 87–10 (1987).

[17] D. A. Edwards and M. J. Syphers, "An Introduction to the Physics of High Energy Accelerators," John Wiley (1993).

[18] F. Zimmermann, Diploma Thesis, University of Hamburg, in German, DESY HERA 91–03 (1991).

[19] F. Zimmermann and F. Willeke, "Long Term Stability and Dynamic Aperture of the HERA Proton Ring," DESY HERA 91–08 (1991).

[20] D. Brandt et al., "Influence of power supply ripple on the dynamic aperture of the SPS in the presence of strong nonlinear fields," CERN SL/90–67 (AP) (1990).

[21] K. Wittenburg, "Transversal Emittance Measurement," *Proceedings of the Bad Lauterberg seminar on HERA commissioning*, DESY HERA 92–07 (1992).

[22] G. Ripken and F. Willeke, "Methods of Beam Optics," DESY 88–114 (1988).

[23] T. Chen and S. Peggs, "Beam-Beam Tune Modulation, the Driven Gravity Pendulum, and Josephson Junctions," *Proceedings of the third ICFA beam dynamics workshop*, Novosibirsk (1989).

[24] S. Peggs, "Hadron Collider Behavior in the Nonlinear Numerical Model EVOL," *Part. Acc.* **17** (1985).

[25] G. N. Watson, "A Treatise on the Theory of Bessel Functions," Cambridge 1966, p. 199 (1966).

[26] B. V. Chirikov, "A Universal Instability of Many-Dimensional Oscillator Systems," *Physics Reports* **52**, No 5 (1979).

[27] L. R. Evans and J. Gareyte, "The Beam-Beam Effect in the SPS," CERN SPS/82–8 (DI-MST) (1982).

[28] L. R. Evans, "The Beam-Beam Interaction," CERN Accelerator School: Antiprotons in Colliding Beam Facilities, Geneva 1984, CERN 84–15 (1984).

[29] A. Schoch, "Theory of linear and nonlinear perturbations of betatron oscillations in alternating gradient synchrotrons," CERN 57–21 (PS Division) 55–56 (1958).

[30] J. D. Jackson, "Classical Electrodynamics," 2nd edition, John Wiley, p. 316 (1975).

[31] A. W. Chao and M. Month, "Particle Trapping during Passage through a High-Order Nonlinear Resonance," *Nucl. Instr. Meth.* **121**, 129-138 (1974).

[32] M. Cornacchia and Y. Chin, "A Study of the Dynamic Aperture Limit in Tristan," *Part. Acc.* **17**, 191–213 (1985).

[33] A. J. Lichtenberg and M. A. Lieberman, "Regular and Stochastic Motion," Springer Verlag (1983).

[34] V. I. Arnold, *Dokl. Akad. Nauk SSSR* **144**, 747 (1962); **148**, 1257 (1963).

[35] V. K. Melnikov, *Dokl. Akad. Nauk SSSR* **156**, 9 (1964).

[36] T. Satogata and S. Peggs, private communication (1992).

[37] J.-P. Jensen, private communication (1993).

[38] H.-J. Eckoldt, private communication (1992).

[39] R. Bacher, private communication (1992).

[40] R. Bacher, K. H. Meß, and M. Seidel, "Transmission Line Characteristics of the Superconducting HERA Dipole and Quadrupole String," *Proceedings of the 1992 High Energy Accelerator Conference*, Hamburg (1992).

[41] H.-J. Eckoldt, "Simulation of Transmissionline Effects within an Octant of the Superconducting HERA Proton Ring during an Energy Dump," *Proceedings of the 1992 High Energy Accelerator Conference*, Hamburg (1992).

[42] H. Kaden, "Wirbelströme und Schirmung in der Nachrichtentechnik," *Technische Physik in Einzeldarstellungen* **10**, (Springer Verlag, Berlin, 1959).

[43] P. Schmüser, private communication (1991).

[44] D. Trines, private communication (1992).

[45] J. Roßbach, "Fast Ground Motion at HERA," DESY 89–023 (1989);
K. Flöttmann, Diploma Thesis, University of Hamburg, in German, DESY HERA 90–09 (1990);
W. Decking, Diploma Thesis, University of Hamburg, in German, DESY HERA 90–13 (1990).

[46] É. Forest, M. Berz, and J. Irwin, "Normal form methods for complicated periodic systems: a complete solution using differential algebra and Lie operators," *Part. Acc.* **24** (1989), p. 91.

[47] É. Forest, "A Hamiltonian-free description of single-particle dynamics for hopelessly comlex periodic systems," LBL–28471, *J. Math. Phys.* **31**, 1133-1144 (1990).

[48] A. J. Dragt and J. M. Finn, "Lie Series and Invariant Functions for Analytic Symplectic Maps," *J. Math. Phys.* **17**, 2215-2227 (1976).

[49] B. V. Chirikov, M. A. Lieberman, D. L. Shepelyansky, and F. M. Vivaldi, "A Theory of Tune Modulation," *Physica* **14D**, 289–304 (1985).

[50] J. Tennyson, "Resonance Transport in Near-Integrable Systems with Many Degrees of Freedom," *Physica* **5D**, 123–135 (1982)

[51] A. Gerasimov, "Diffusive Transport Enhancement by Isolated Resonances and Distribution Tail Growth in Hadronic Beams," *Proceedings of the 1991 IEEE Particle Accelerator Conference*, San Francisco, and FERMILAB–Conf–90/250 (1991).

[52] T. Chen et al., "Measurements of a Hamiltonian System and Their Description by a Diffusive Model," *Phys. Rev. Lett.* **68**, 33 (1992).

[53] M. Seidel, "Determination of Diffusion Rates in the Proton Beam Halo of HERA," DESY HERA 93–04 (1993).

[54] M. Seidel, "The HERA-p Collimation System and First Experience with a Single Collimator," *Proceedings of the Bad Lauterberg seminar on HERA commissioning*, DESY HERA 92–07 (1992).

[55] F. Schmidt, F. Zimmermann, and F. Willeke, "Comparison of Methods to Determine Long-Term Stability in Proton Storage Rings," DESY HERA 91–07, CERN SL/91–14 (AP), published in *Part. Acc.* **35**, 249 (1991).

[56] A. Piwinski, "Beam losses and lifetime," CERN Accelerator School, Gif-sur-Yvette 1985, CERN 85–19 (1985).

[57] E. Karantzoulis and J. R. M. Maidment, "Estimates of Intra-beam Scattering in HERA," DESY HERA 85–12 (1985).

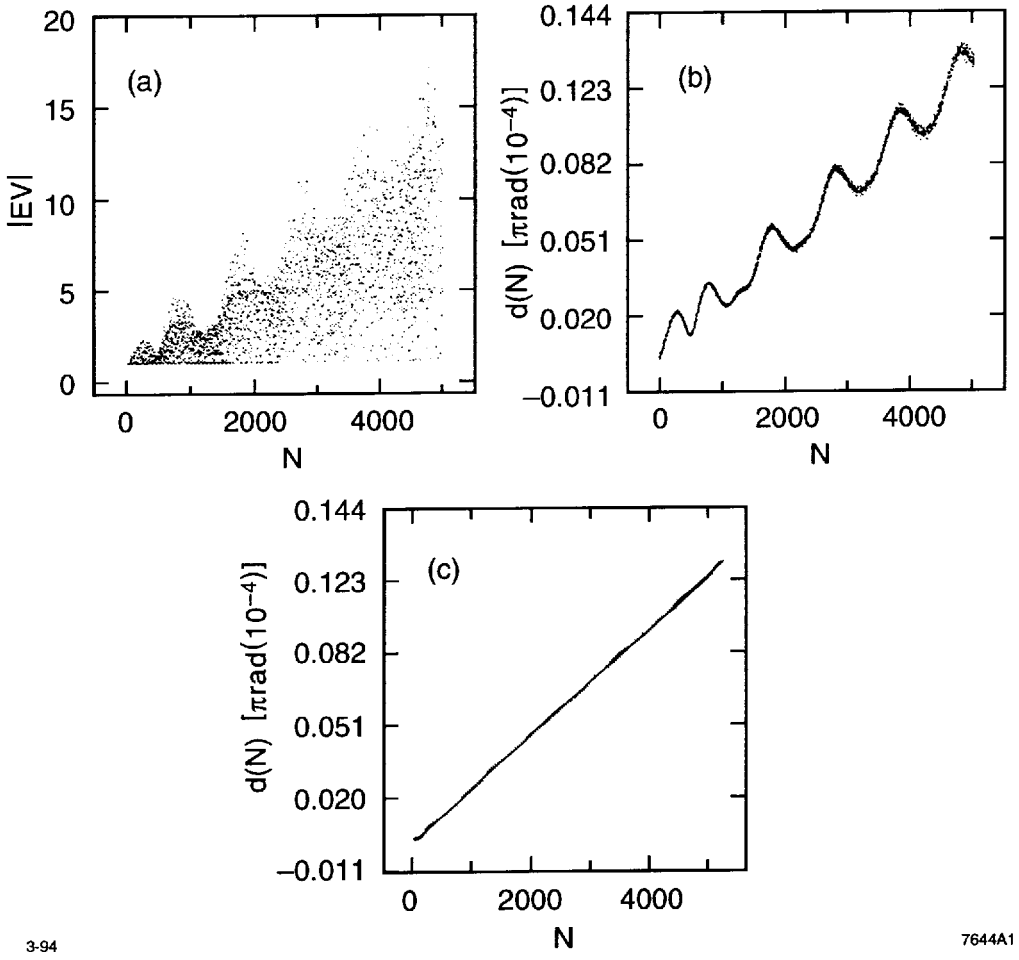

Figure 1:

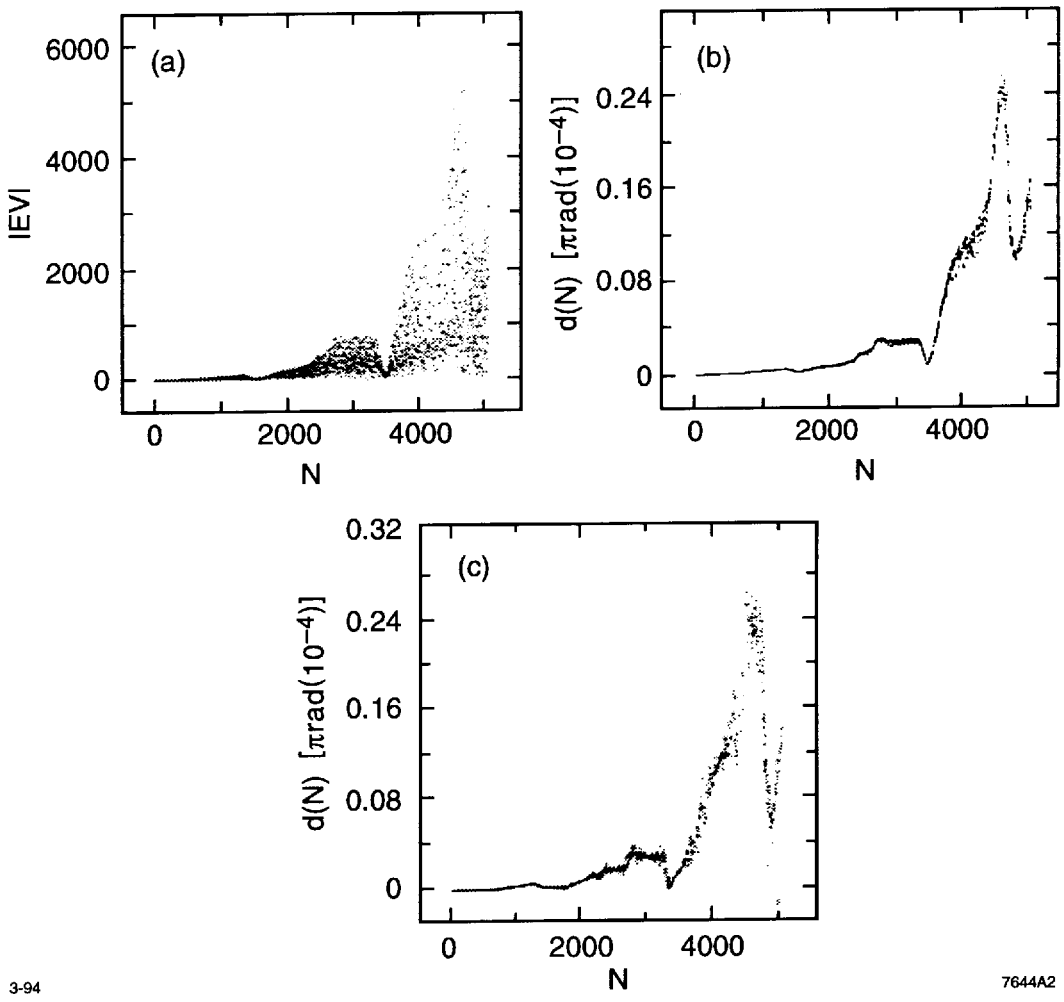
(a)
6000
4000
2000
0
|EV|
0
2000
4000
N
(b)
0.24
0.16
0.08
0
d(N) [πrad(10⁻⁴)]
0
2000
4000
N
(c)
0.32
0.24
0.16
0.08
0
d(N) [πrad(10⁻⁴)]
0
2000
4000
N
3-94
7644A2

Figure 2:

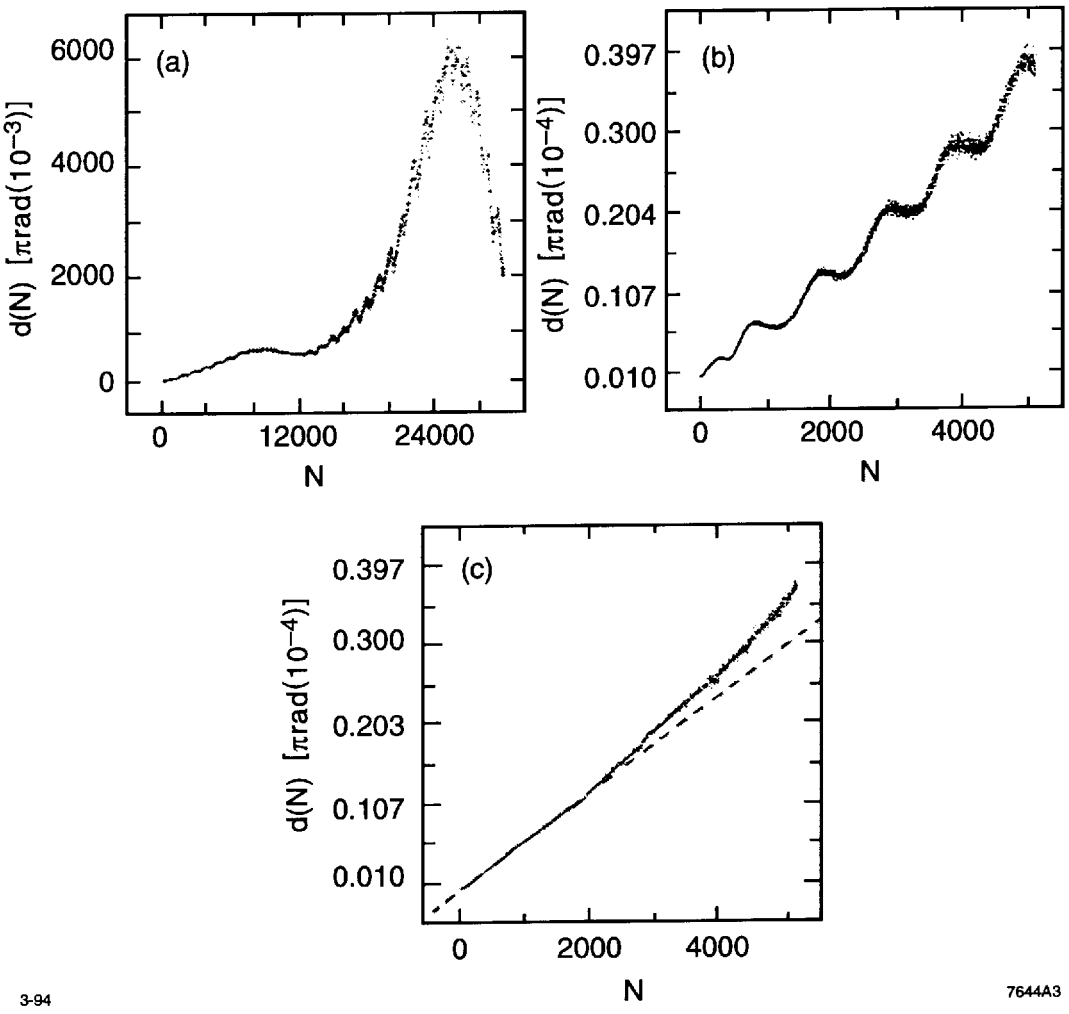
(a)
6000
4000
2000
0
d(N) [πrad(10⁻³)]
0
12000
24000
N
(b)
0.397
0.300
0.204
0.107
0.010
d(N) [πrad(10⁻⁴)]
0
2000
4000
N
(c)
0.397
0.300
0.203
0.107
0.010
d(N) [πrad(10⁻⁴)]
0
2000
4000
N
3-94
7644A3

Figure 3:

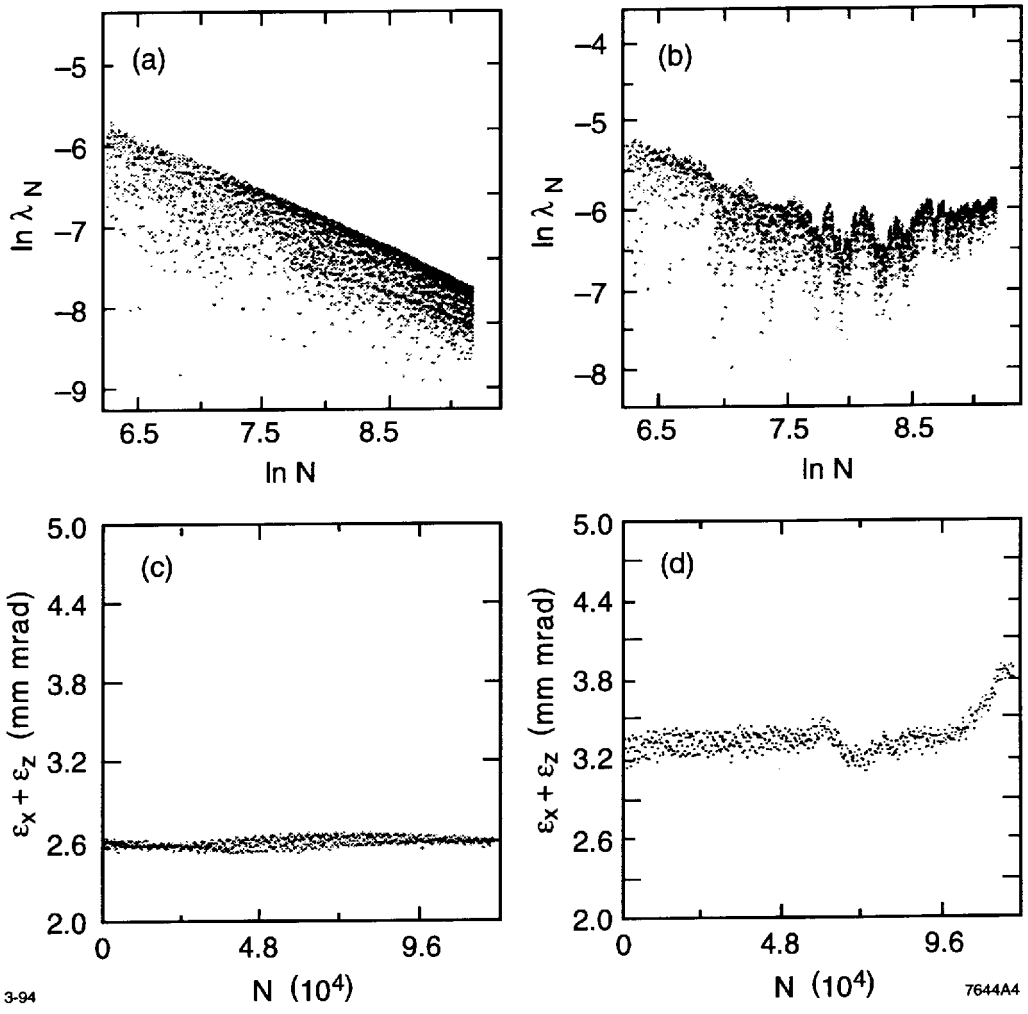

Figure 4:

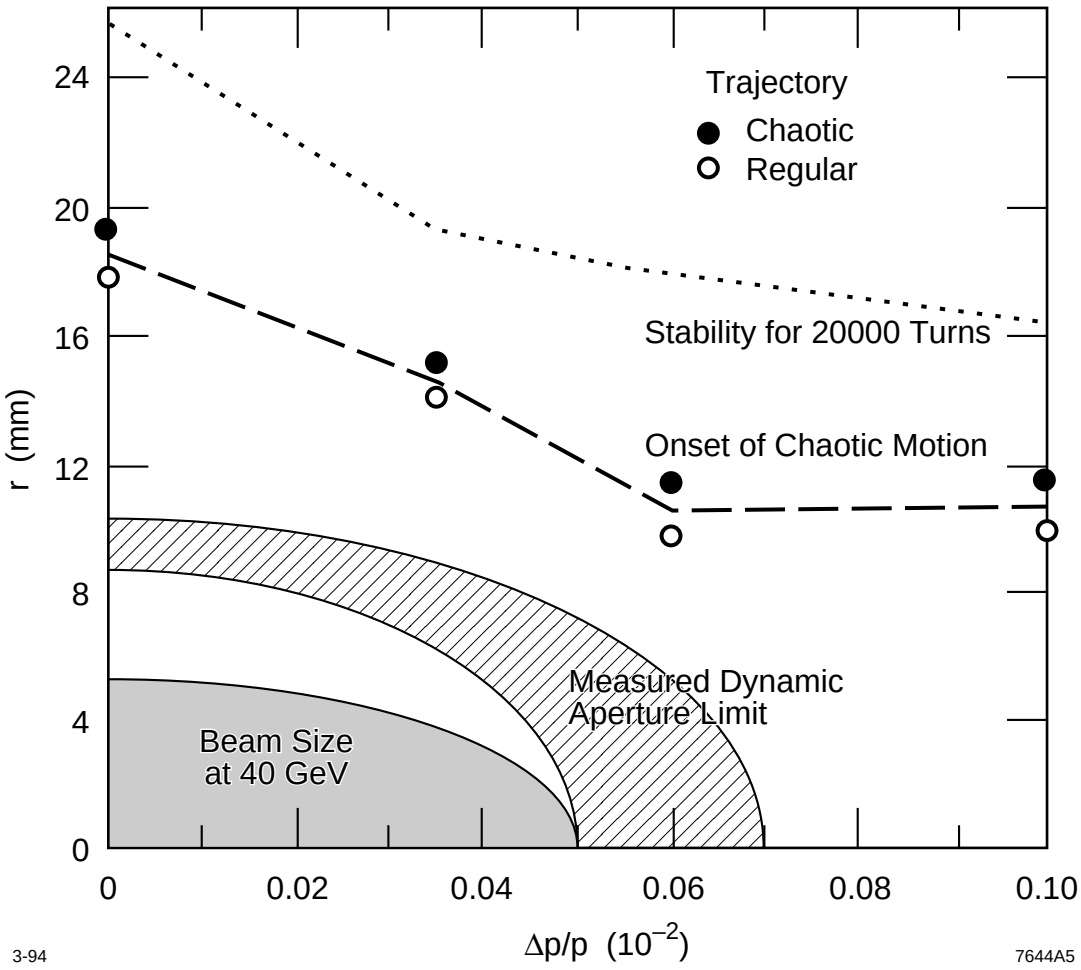
Trajectory
Chaotic
Regular
Stability for 20000 Turns
Onset of Chaotic Motion
Measured Dynamic
Aperture Limit
Beam Size
at 40 GeV
r (mm)
Δp/p (10^−2)
0
4
8
12
16
20
24
0
0.02
0.04
0.06
0.08
0.10
3-94
7644A5

Figure 5:

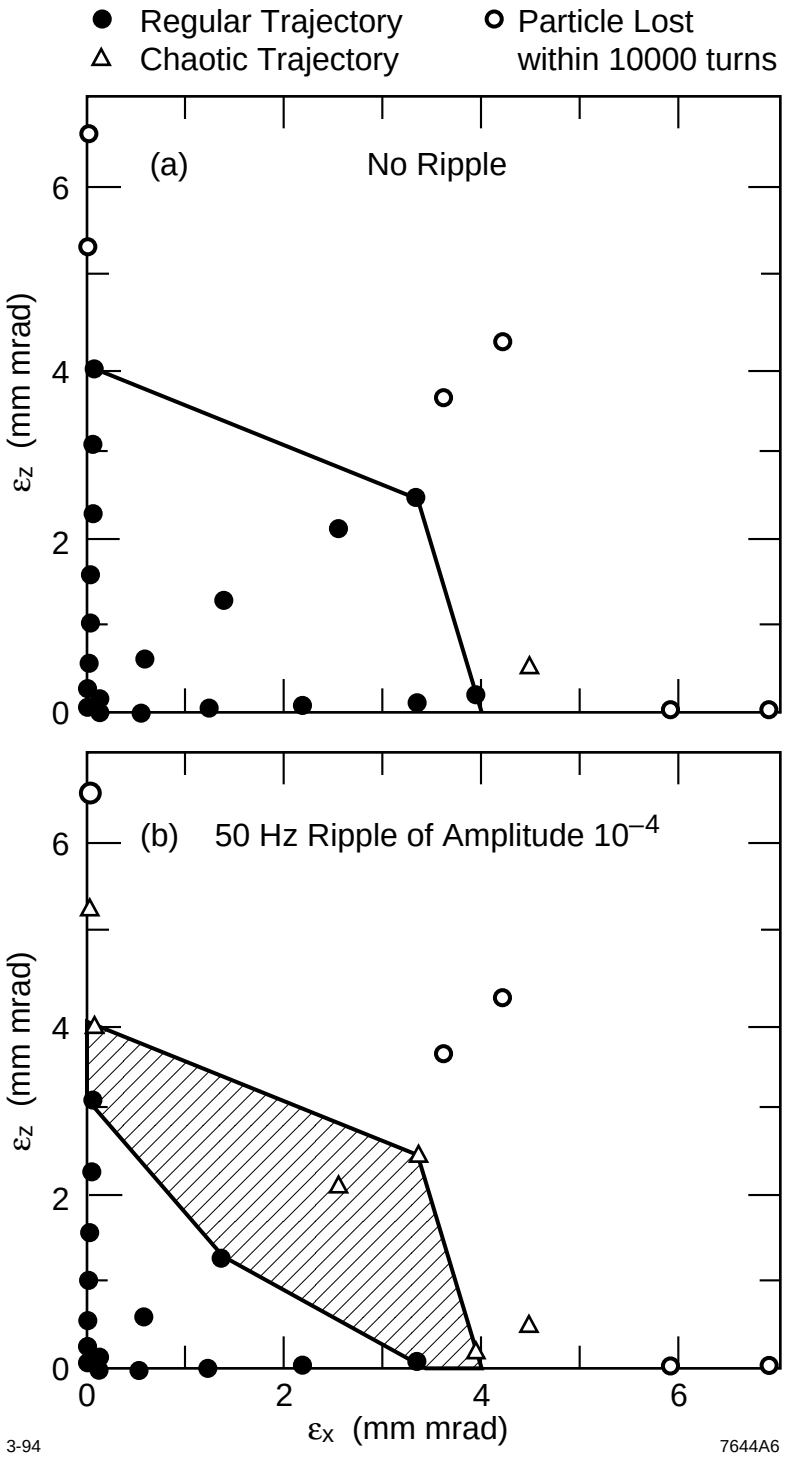
Regular Trajectory
Particle Lost within 10000 turns
Chaotic Trajectory
(a) No Ripple
(b) 50 Hz Ripple of Amplitude 10^{-4}
ε_z (mm mrad)
ε_x (mm mrad)
0
2
4
6
3-94
7644A6

Figure 6:

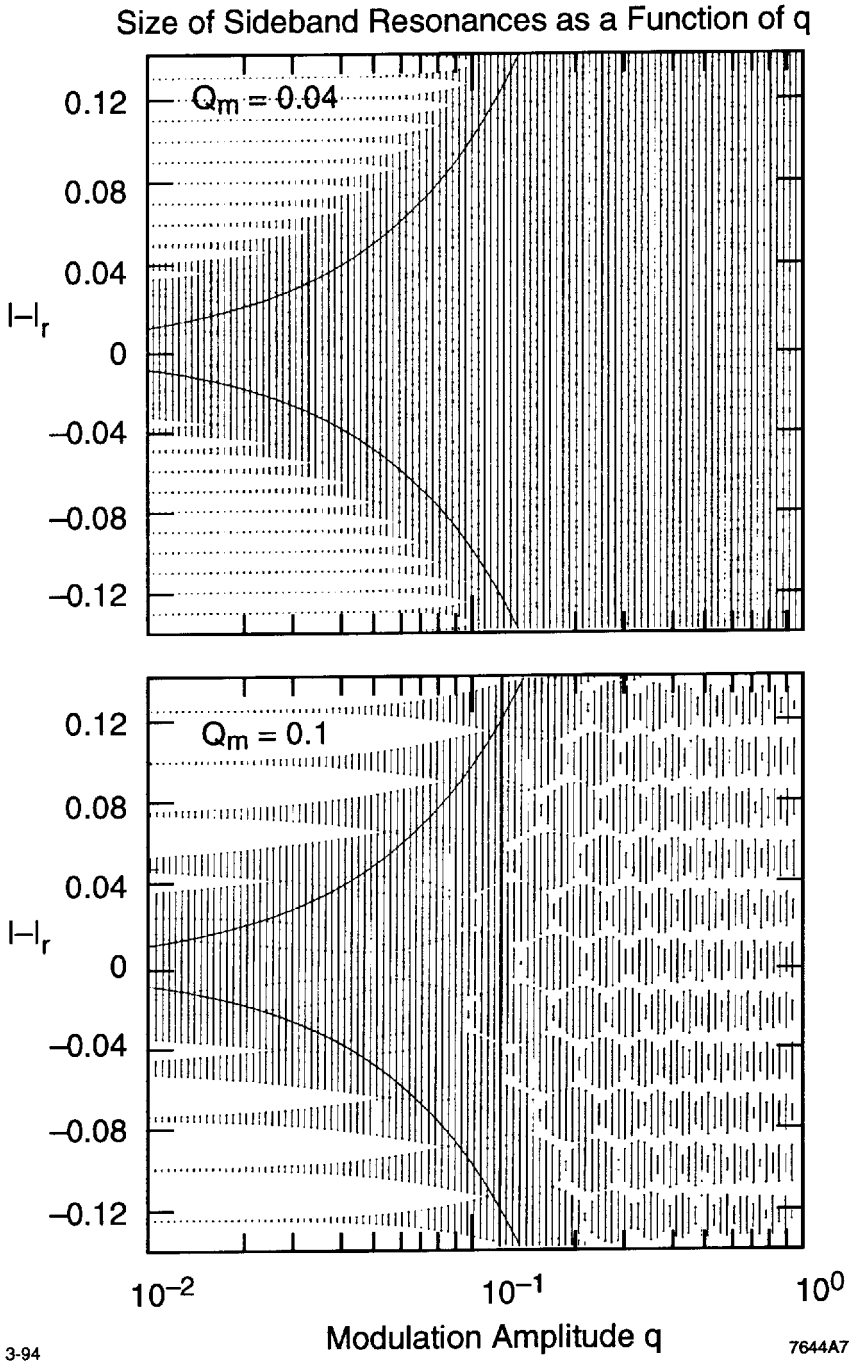
Size of Sideband Resonances as a Function of q
$Q_m = 0.04$
$Q_m = 0.1$
0.12
0.08
0.04
0
–0.04
–0.08
–0.12
$I-I_r$
10^{-2}
10^{-1}
10^{0}
Modulation Amplitude q
3-94
7644A7

Figure 7:

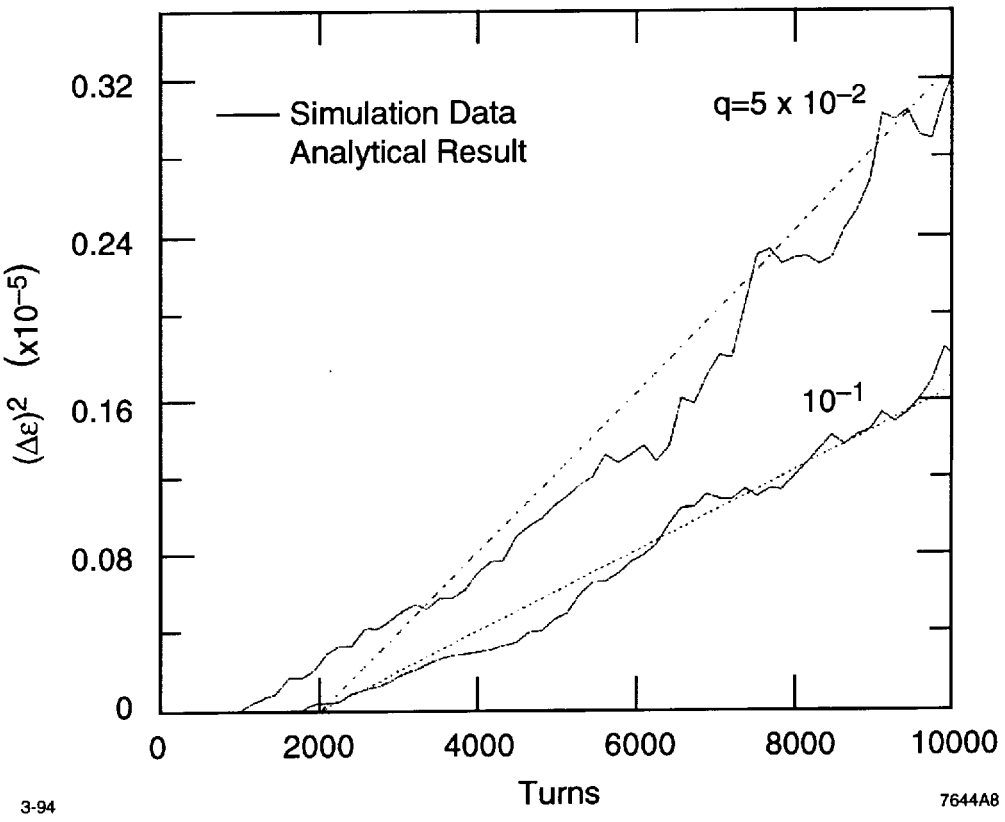
0.32
0.24
0.16
0.08
0
$(\Delta\varepsilon)^2$ $(x10^{-5})$
Simulation Data
Analytical Result
$q=5 \times 10^{-2}$
10^{-1}
0
2000
4000
6000
8000
10000
Turns
3-94
7644A8

Figure 8:

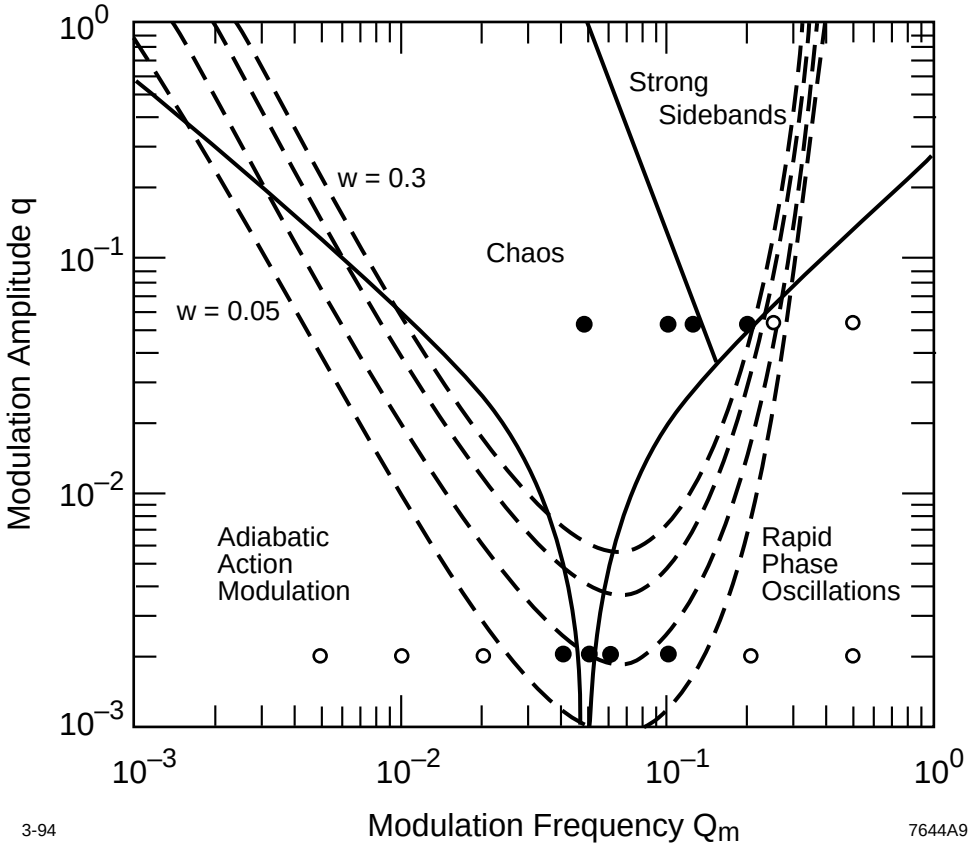
Strong
Sidebands
w = 0.3
Chaos
w = 0.05
Adiabatic
Action
Modulation
Rapid
Phase
Oscillations
Modulation Amplitude q
Modulation Frequency Qm
3-94
7644A9

Figure 9:

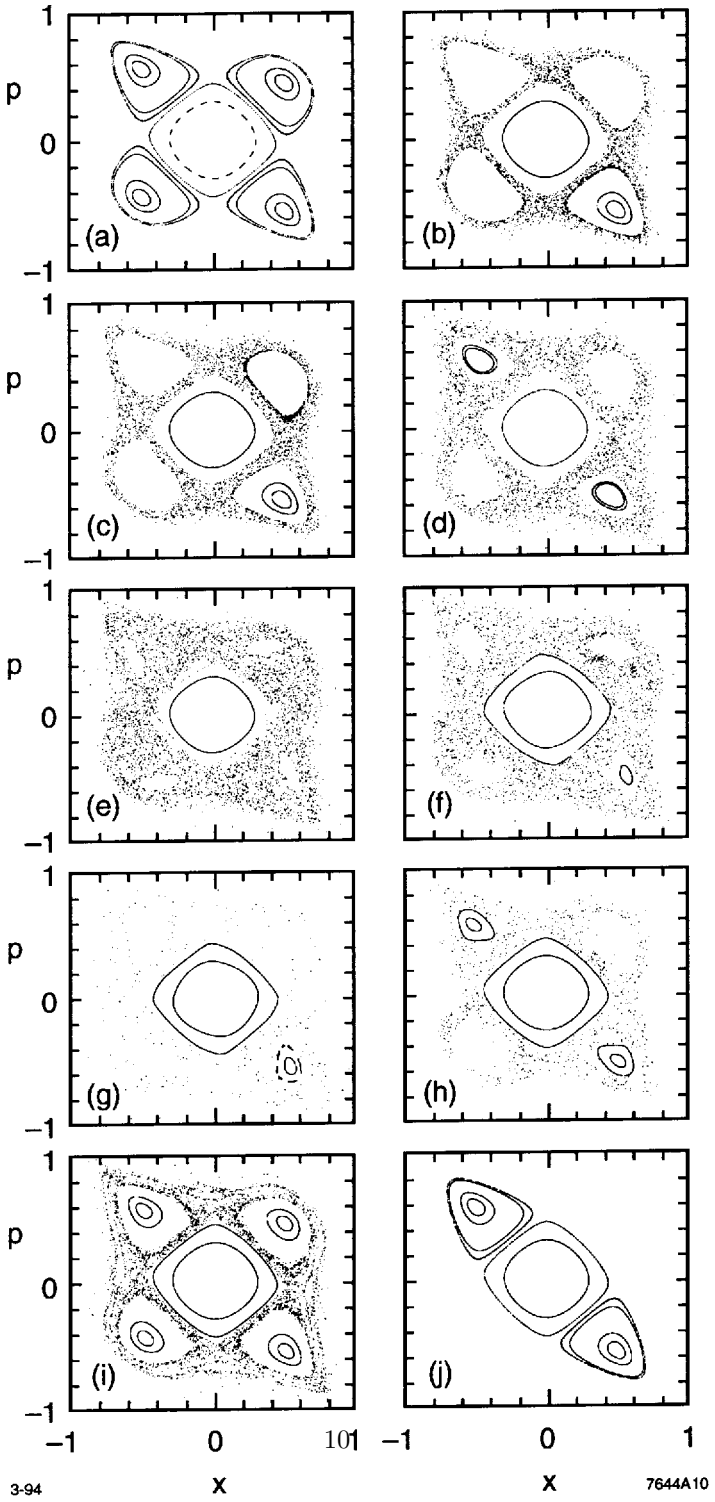

Figure 10:

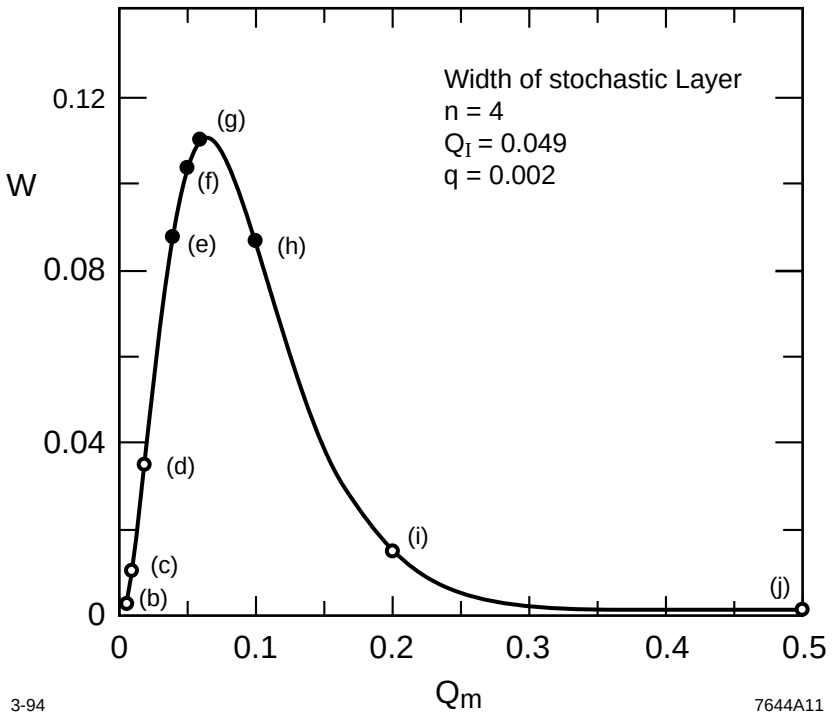
Width of stochastic Layer
n = 4
Q_I = 0.049
q = 0.002
W
0.12
0.08
0.04
0
(g)
(f)
(e)
(h)
(d)
(c)
(b)
(i)
(j)
0
0.1
0.2
0.3
0.4
0.5
Qm
3-94
7644A11

Figure 11:

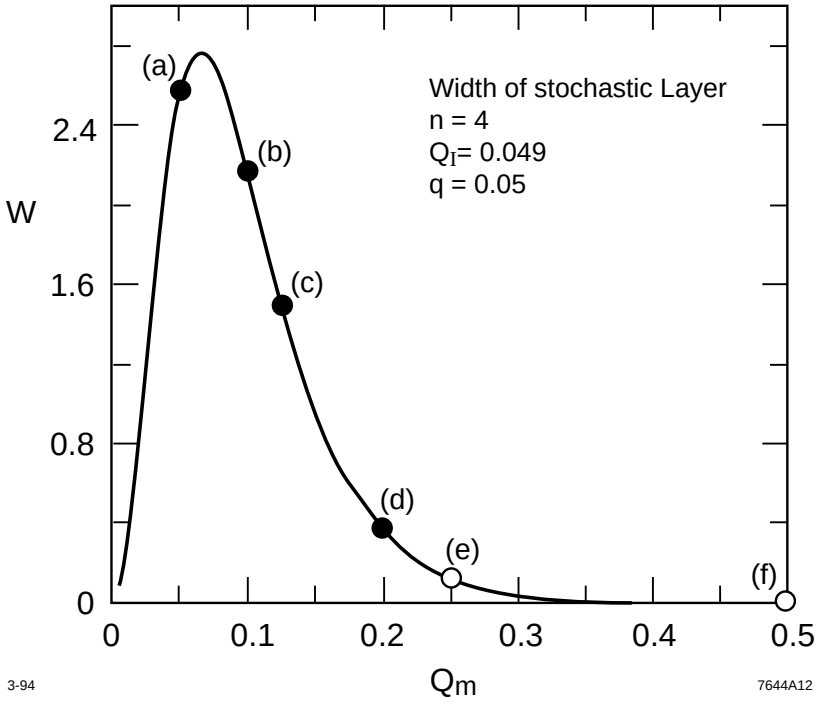
Width of stochastic Layer
n = 4
Q_I= 0.049
q = 0.05
(a)
(b)
(c)
(d)
(e)
(f)
W
2.4
1.6
0.8
0
0
0.1
0.2
0.3
0.4
0.5
Qm
3-94
7644A12

Figure 12:

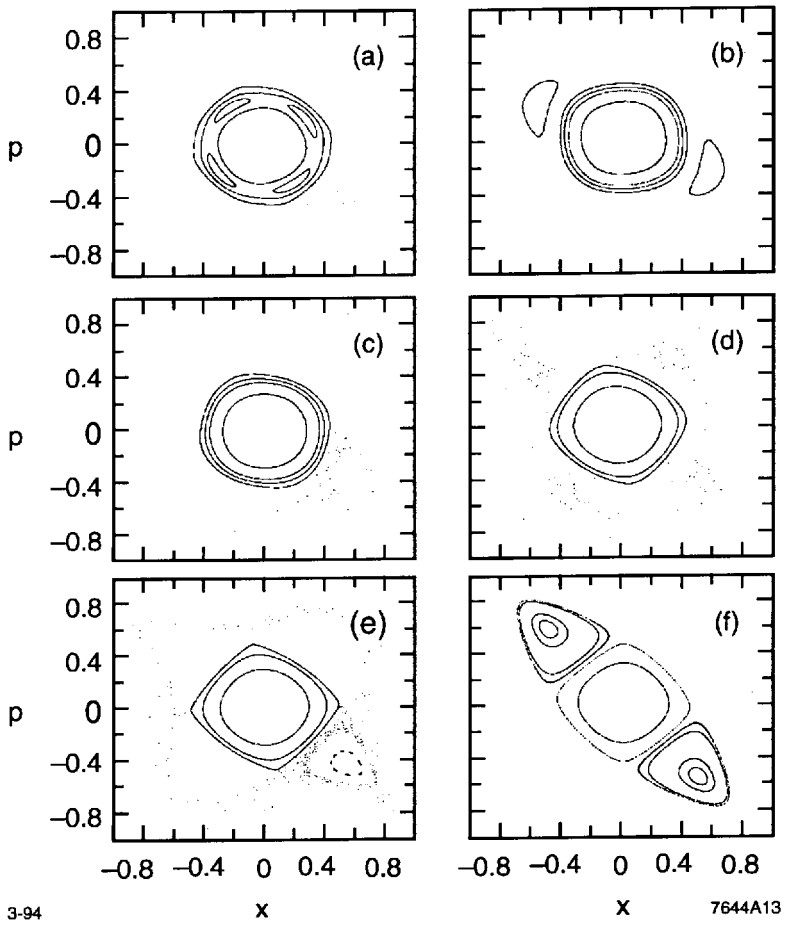

Figure 13:

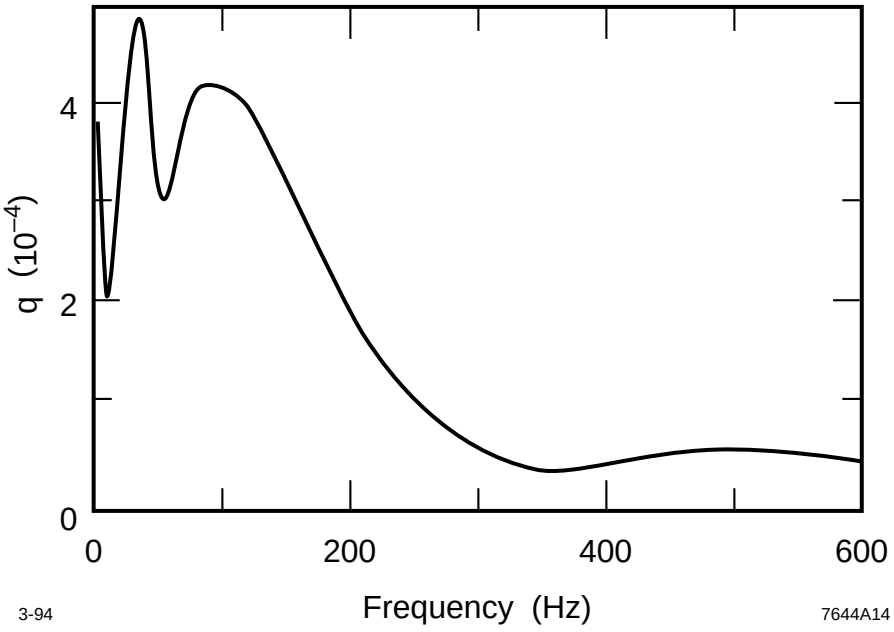

Figure 14:

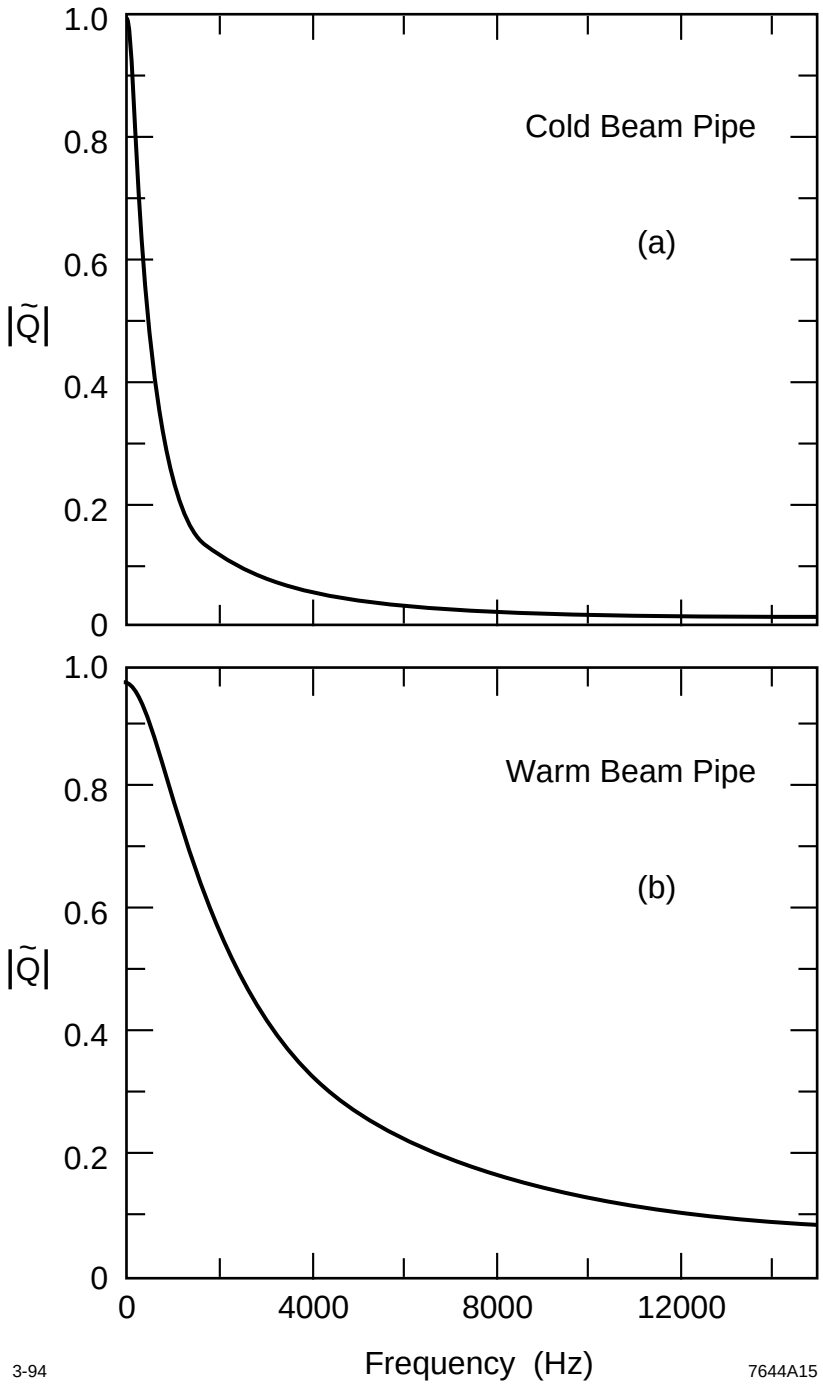
1.0
0.8
0.6
0.4
0.2
0
|Q̃|
Cold Beam Pipe
(a)
1.0
0.8
0.6
0.4
0.2
0
|Q̃|
Warm Beam Pipe
(b)
0
4000
8000
12000
Frequency (Hz)
3-94
7644A15

Figure 15:

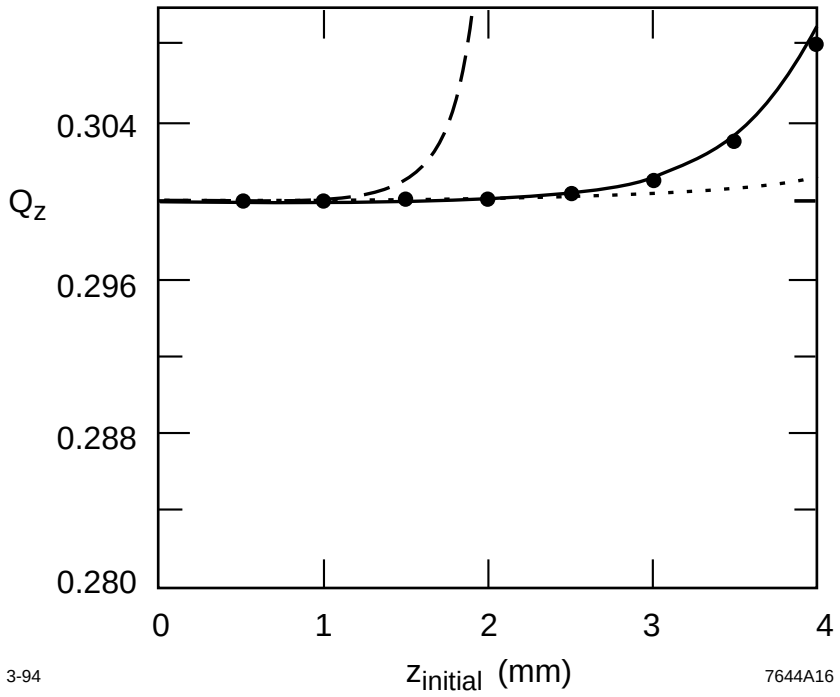

Figure 16:

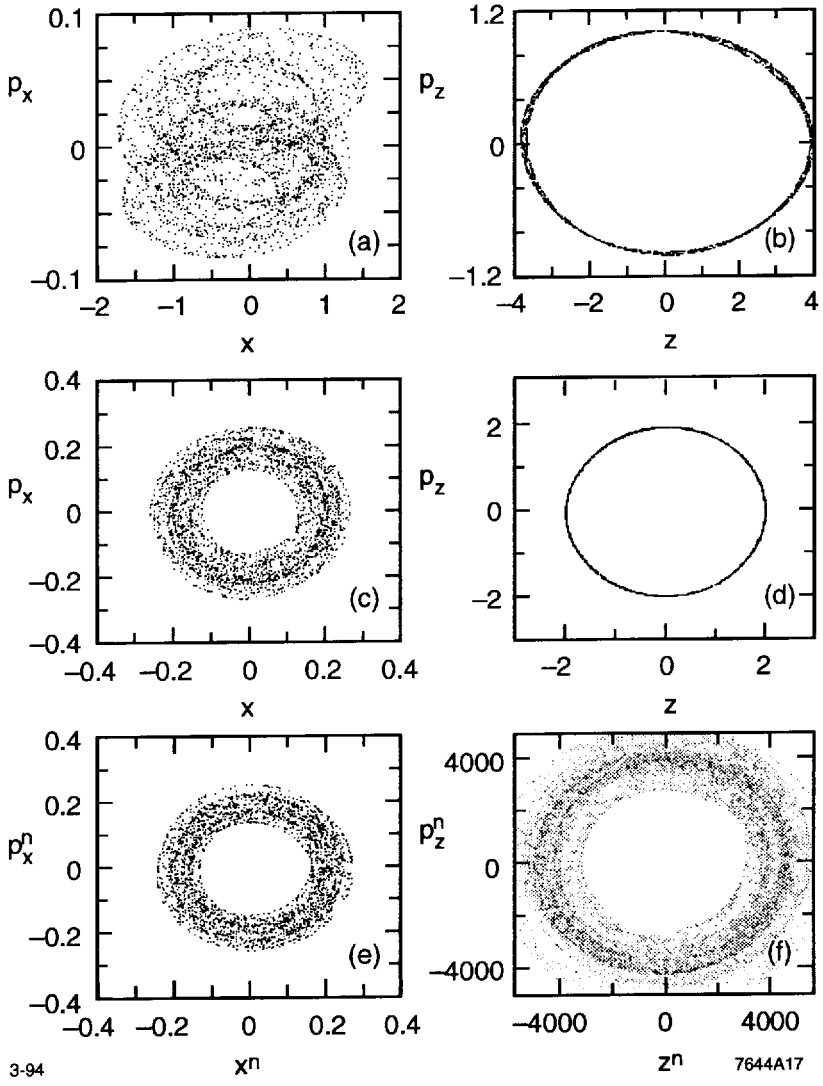
0.1
p_x
0
−0.1
−2
−1
0
1
2
x
(a)
1.2
p_z
0
−1.2
−4
−2
0
2
4
z
(b)
0.4
0.2
p_x
0
−0.2
−0.4
−0.4
−0.2
0
0.2
0.4
x
(c)
2
p_z
0
−2
−2
0
2
z
(d)
0.4
0.2
p_x^n
0
−0.2
−0.4
−0.4
−0.2
0
0.2
0.4
x^n
(e)
4000
p_z^n
0
−4000
−4000
0
4000
z^n
(f)
3-94
7644A17

Figure 17:

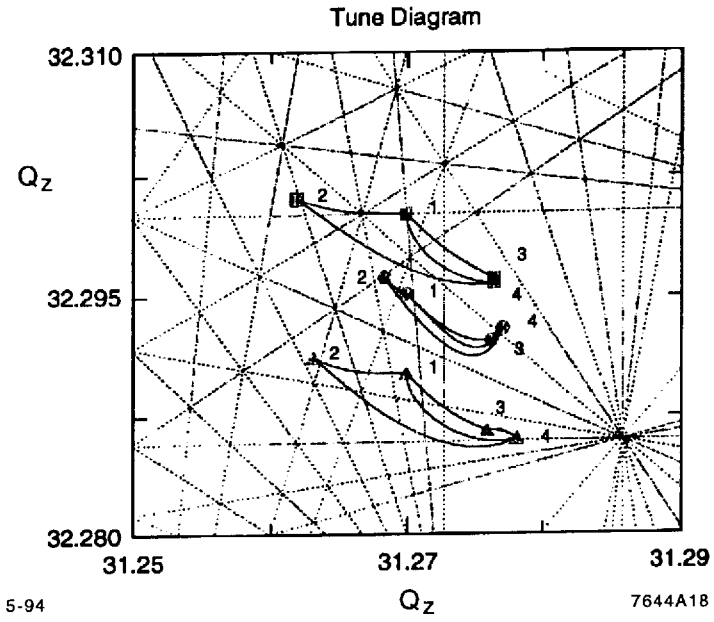
Tune Diagram
32.310
32.295
32.280
Q_z
31.25
31.27
31.29
Q_z
5-94
7644A18

Figure 18:

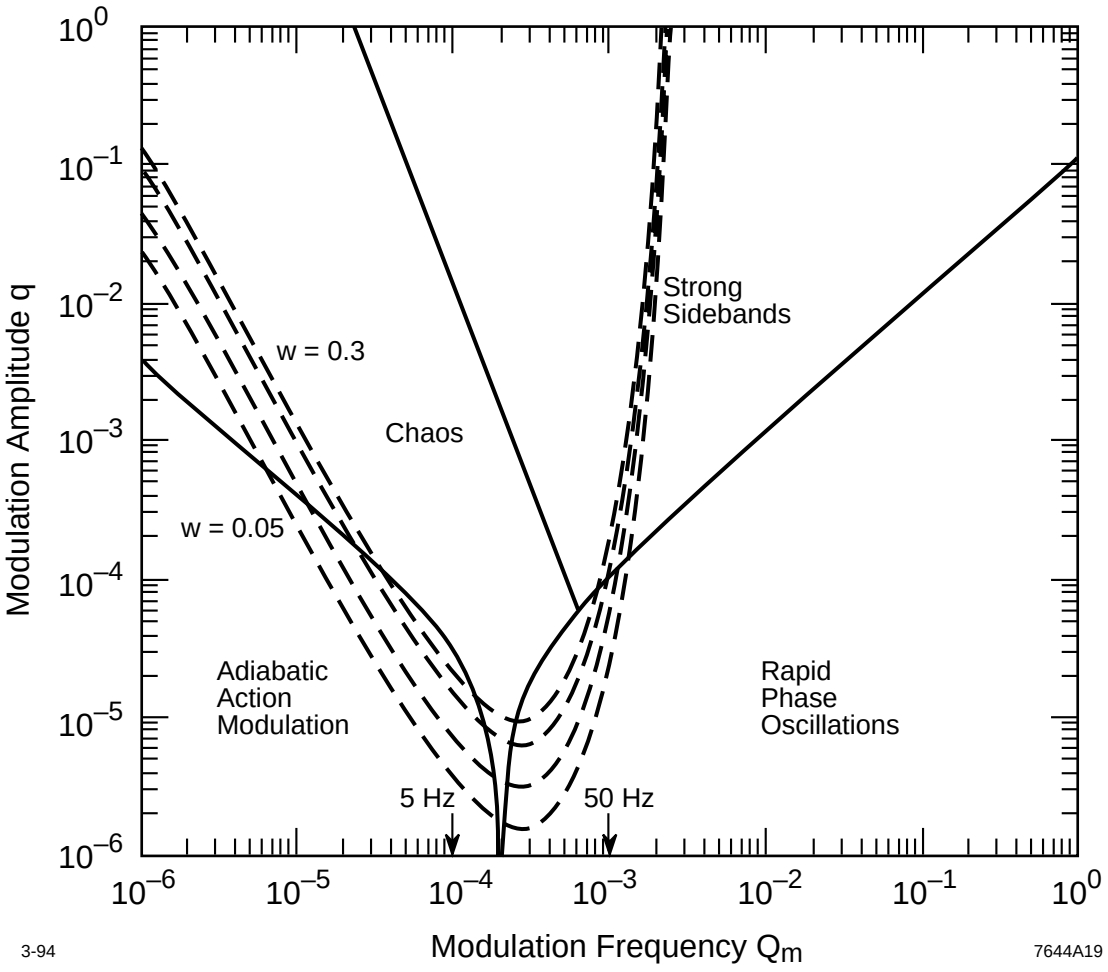
Modulation Amplitude q
Modulation Frequency Q_m
10^0
10^{-1}
10^{-2}
10^{-3}
10^{-4}
10^{-5}
10^{-6}
10^{-6} 10^{-5} 10^{-4} 10^{-3} 10^{-2} 10^{-1} 10^0
w = 0.3
w = 0.05
Chaos
Strong
Sidebands
Adiabatic
Action
Modulation
Rapid
Phase
Oscillations
5 Hz
50 Hz
3-94
7644A19

Figure 19:

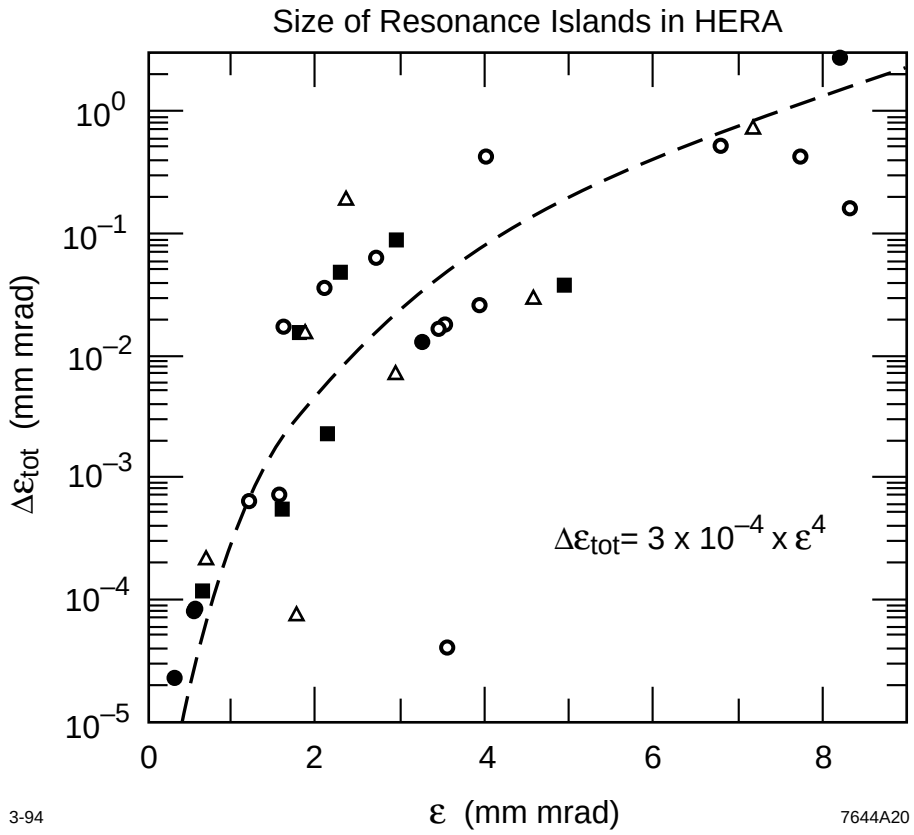
Size of Resonance Islands in HERA
$\Delta\varepsilon_{tot}$ (mm mrad)
10^{0}
10^{-1}
10^{-2}
10^{-3}
10^{-4}
10^{-5}
$\Delta\varepsilon_{tot}= 3 \times 10^{-4} \times \varepsilon^{4}$
0
2
4
6
8
ε (mm mrad)
3-94
7644A20

Figure 20:

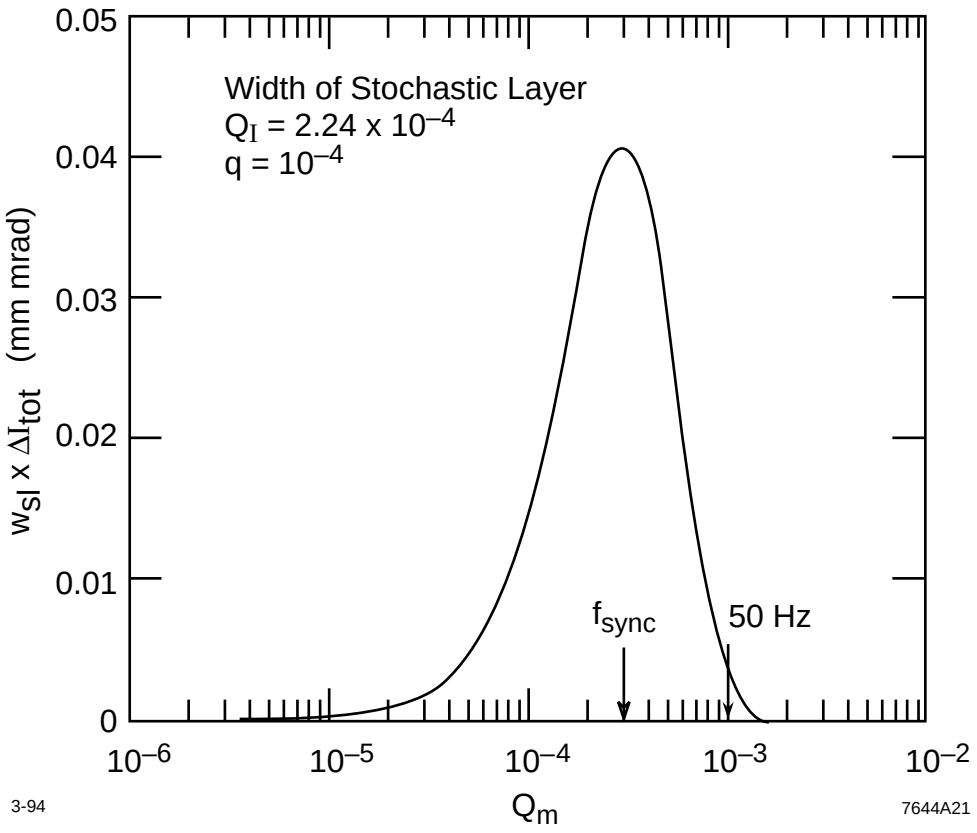
Width of Stochastic Layer
$Q_I = 2.24 \times 10^{-4}$
$q = 10^{-4}$
$w_{SI} \times \Delta I_{tot}$ (mm mrad)
0.05
0.04
0.03
0.02
0.01
0
f_{sync}
50 Hz
10^{-6}
10^{-5}
10^{-4}
10^{-3}
10^{-2}
Q_m
3-94
7644A21

Figure 21:

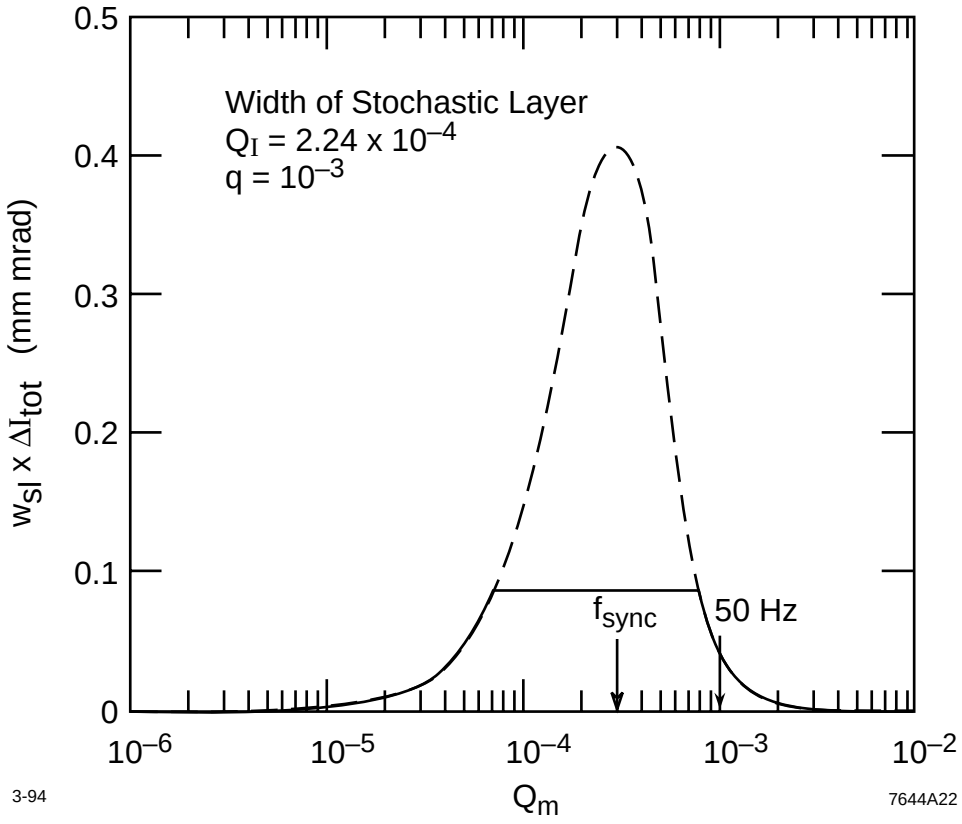
Width of Stochastic Layer
$Q_I = 2.24 \times 10^{-4}$
$q = 10^{-3}$
$w_{SI} \times \Delta I_{tot}$ (mm mrad)
0.5
0.4
0.3
0.2
0.1
0
f_{sync}
50 Hz
10^{-6}
10^{-5}
10^{-4}
10^{-3}
10^{-2}
Q_m
3-94
7644A22

Figure 22:

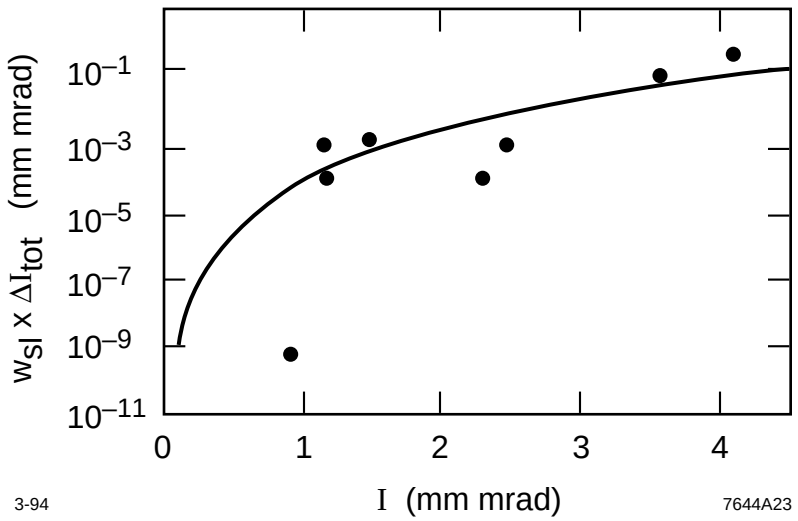
$w_{SI} \times \Delta I_{tot}$ (mm mrad)
10^{-1}
10^{-3}
10^{-5}
10^{-7}
10^{-9}
10^{-11}
0
1
2
3
4
I (mm mrad)
3-94
7644A23

Figure 23:

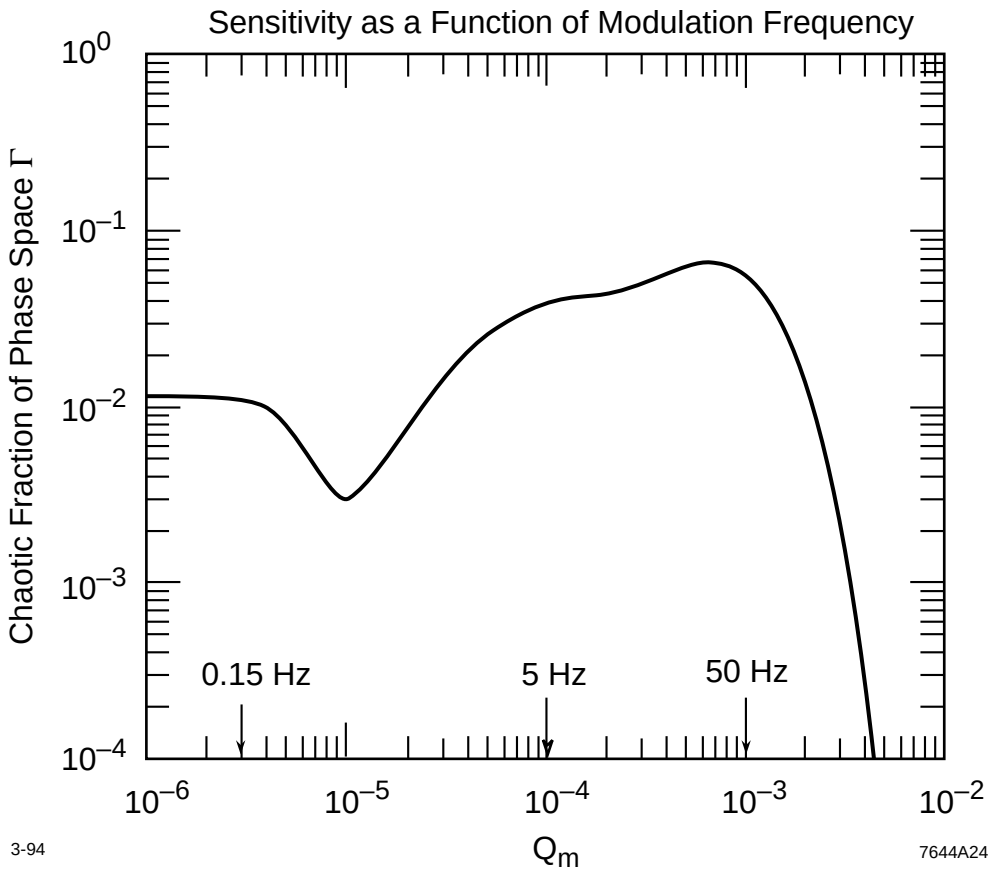
Sensitivity as a Function of Modulation Frequency
Chaotic Fraction of Phase Space Γ
10^0
10^−1
10^−2
10^−3
10^−4
0.15 Hz
5 Hz
50 Hz
10^−6
10^−5
10^−4
10^−3
10^−2
Q_m
3-94
7644A24

Figure 24:

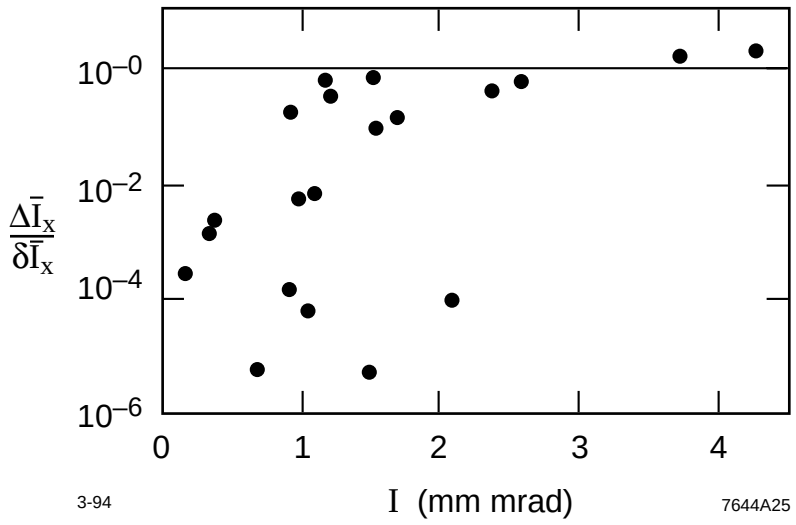
10^{-0}
10^{-2}
10^{-4}
10^{-6}
$\frac{\Delta \bar{I}_x}{\delta \bar{I}_x}$
0
1
2
3
4
I (mm mrad)
3-94
7644A25

Figure 25:

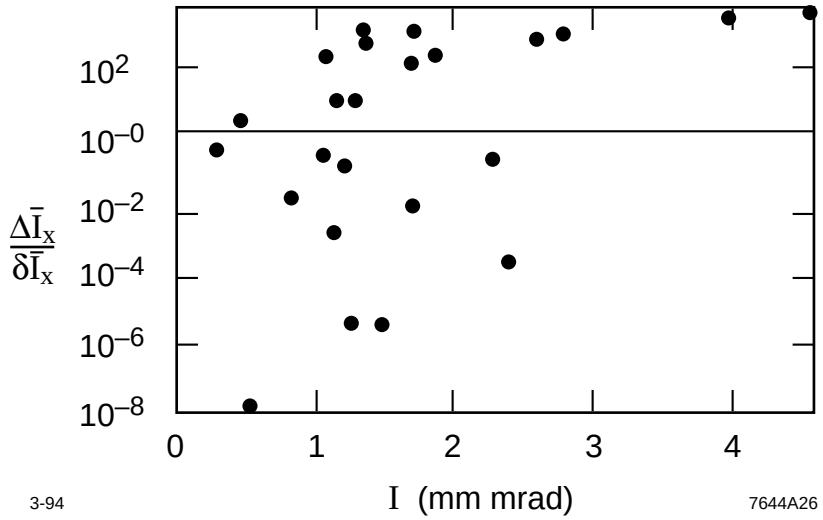

Figure 26:

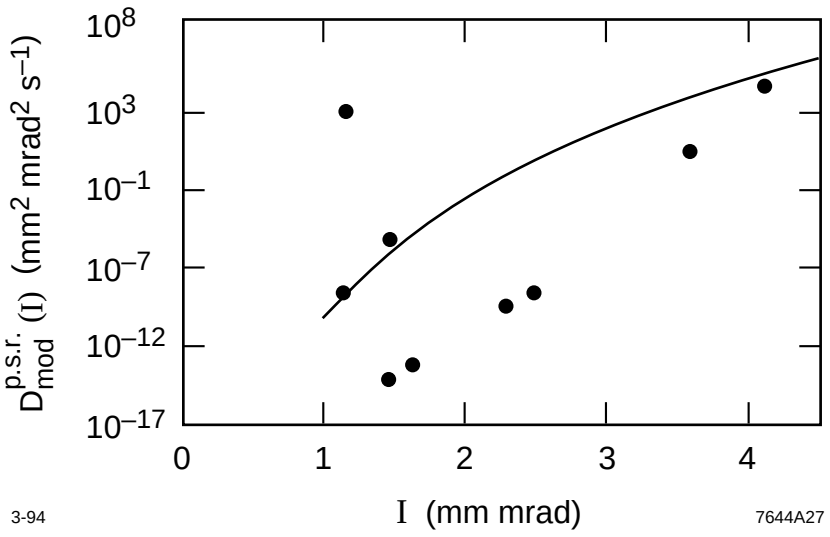

Figure 27:

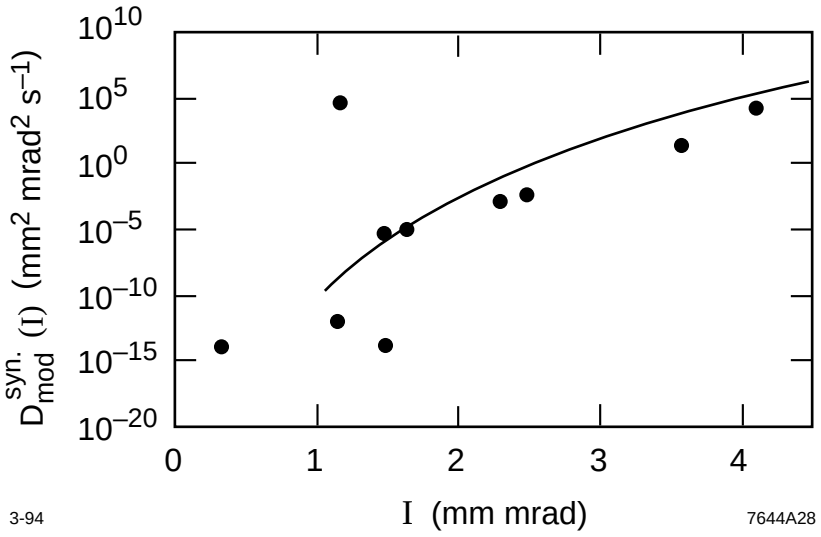

Figure 28:

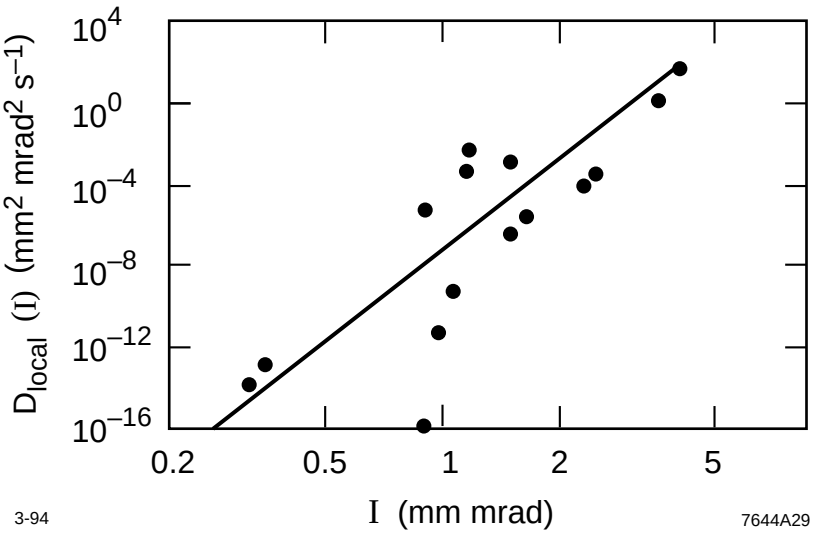

Figure 29:

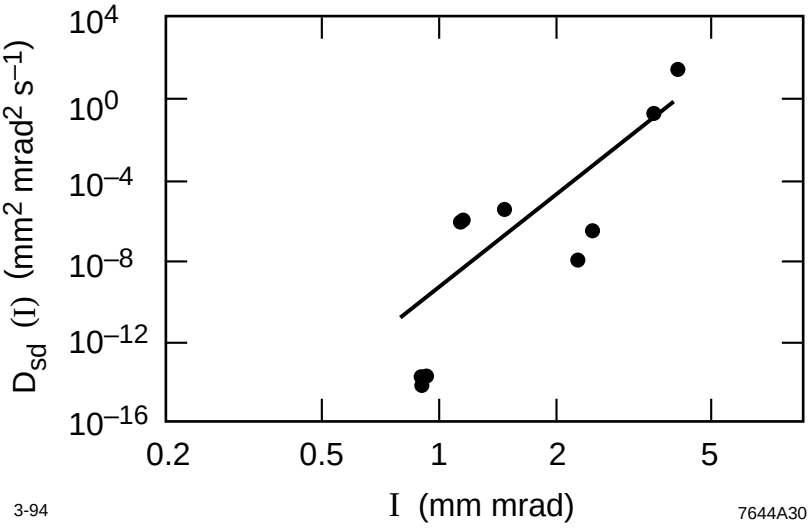
10^4
10^0
10^{-4}
10^{-8}
10^{-12}
10^{-16}
D_{sd} (I) (mm^2 $mrad^2$ s^{-1})
0.2
0.5
1
2
5
I (mm mrad)
3-94
7644A30

Figure 30:

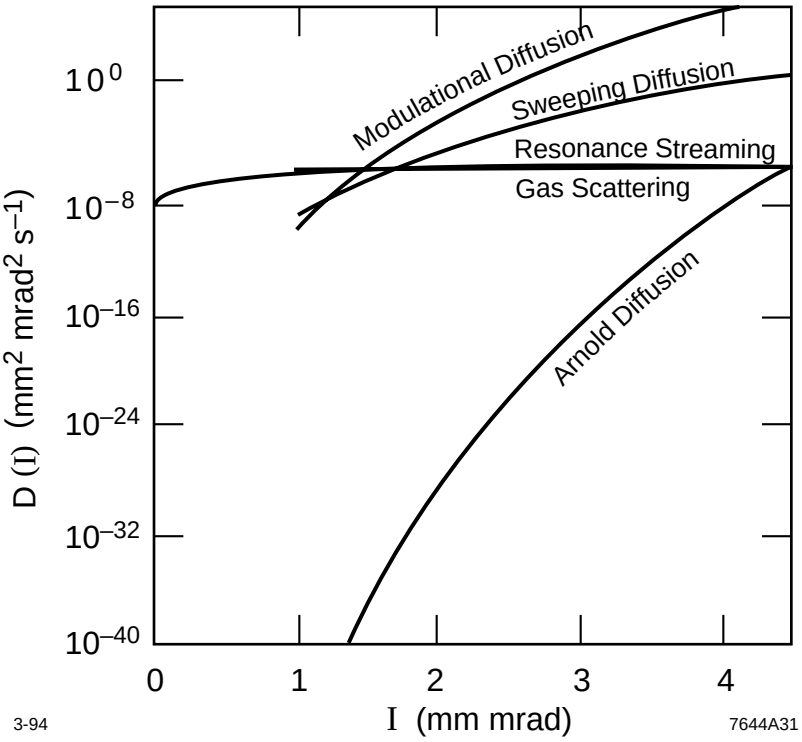
Modulational Diffusion
Sweeping Diffusion
Resonance Streaming
Gas Scattering
Arnold Diffusion
10 0
10−8
10−16
10−24
10−32
10−40
D (I) (mm2 mrad2 s−1)
0
1
2
3
4
I (mm mrad)
3-94
7644A31

Figure 31:

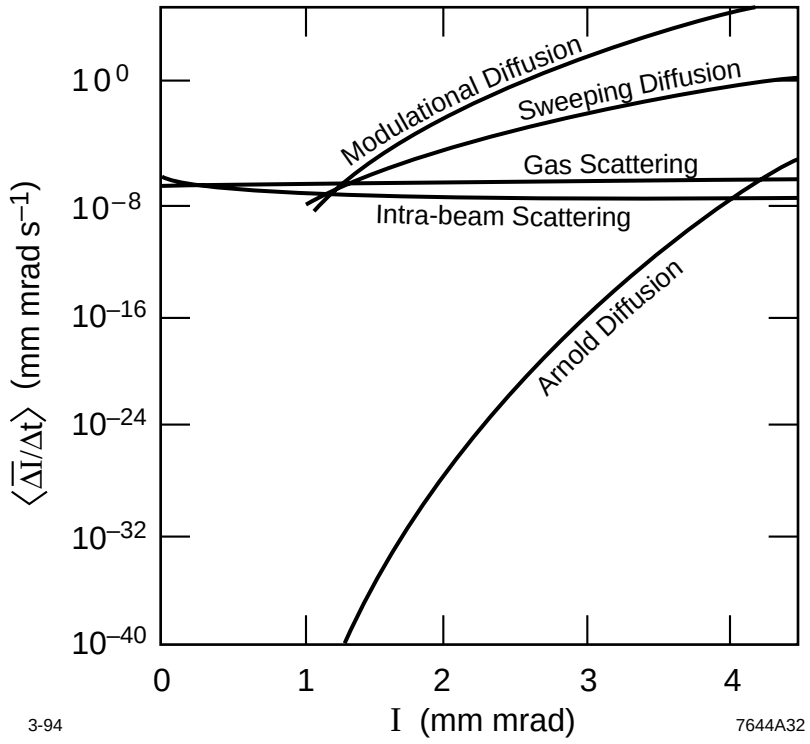
Modulational Diffusion
Sweeping Diffusion
Gas Scattering
Intra-beam Scattering
Arnold Diffusion
10^{0}
10^{-8}
10^{-16}
10^{-24}
10^{-32}
10^{-40}
$\langle \overline{\Delta I/\Delta t} \rangle$ (mm mrad s^{-1})
0
1
2
3
4
I (mm mrad)
3-94
7644A32

Figure 32: